HADROPRODUCTION OF $\Lambda_c \rightarrow pK\pi$

BY

JOHN EUGENE FILASETA

B.S., University of Arizona, 1979
M.S., University of Illinois, 1980

THESIS

Submitted in partial fulfillment of the requirements
for the degree of Doctor of Philosophy in Physics
in the Graduate College of the
University of Illinois at Urbana-Champaign, 1987

Urbana, Illinois

HADROPRODUCTION OF $\Lambda_c \rightarrow pK\pi$

John Eugene Filaseta, Ph.D.
Department of Physics
University of Illinois at Urbana-Champaign, 1987

Production of the charmed baryon Λ_c has been observed in n-nucleus collisions at the Proton East area of FNAL. A 5σ peak was seen in the decay mode $\Lambda_c^+ \rightarrow pK^-\pi^+$ (and charge congugate). The lifetime was determined to be consistent with the current world average of 0.23 ps, and the cross section for Λ_c^+ at $\sqrt{s} = 33$ GeV was measured to be

$$\sigma \cdot BR \;=\; 2.1 \;\pm\; 1.1\,(\pm.74)\mu\text{b/nucleon}$$

for $0.028 < x_f < 0.226$. The fraction of $\Lambda_c^+ \;/\; (\Lambda_c^+ + \Lambda_c^-)$ was estimated to be $78\% \pm 18\%$.

ACKNOWLEDGEMENTS

First, and foremost, I wish to thank Jim Wiss. His advice, help, and encouragement have been invaluable to me during my "career" as a graduate student. His enthusiasm for high energy physics can only be matched by his good humor. I will always value his friendship.

I also would like to thank Mike Diesburg, especially for his efforts on the preliminary analysis of inclusive Λ_c's. Paul Coteus deserves special recognition for his careful work on the vertex chamber. His toil has paid off, as seen by the successful application of lifetime anaylsis techniques.

I am grateful for the support and efforts of all who participated in E400. I especially wish to thank Dave Harding, whose patience and hard work were inspiring; and John Cumalat, for his help and guidance.

The contributions from my fellow graduate students at the University of Illinois must be recognized. Calvin Shipbaugh's development of the Čerenkov algorithms is appreciated. Tom Kroc's analysis on the magnetic fields played a key role in charged particle tracking. I was fortunate to have Tom's help during the busy days of writing this thesis.

I would like to thank the people who are employed by the University of Illinois High Energy Physics Group. Jerry Wray and Dave Lesny, have managed to keep the computer system running smoothly. Jerry was always there to answer my questions, especially the ones about TEX. I appreciate the friendly assistance of the adminstrative personnel: Bill Testory, Dorothy Schoeps, Jeannine Adomaitis, and Deborah Oberg.

Finally, I would like to dedicate this thesis to my parents for their many years of love and support.

This research was funded in part by the U.S. Department of Energy under contract DE-AC02-76ER01195.

TABLE OF CONTENTS

CHAPTER 1

Introduction and Theory

In 1970, Glashow, Iliopoulos, and Maiani (GIM) demonstrated that by introducing a fourth quark (dubbed the charmed quark or the c quark) into the Weinberg - Salam model of the weak interaction, one could explain the observed absence of weak decay processes involving strangeness changing neutral currents[1]. If this new heavier quark truly existed, high mass, charm resonances could be found. And indeed, in 1974, the lowest-lying J/ψ meson (or charmonium, $c\bar{c}$) resonance was discovered simultaneously by experimenters at SPEAR[2] and BNL[3]. Since then a series of charmonium states have been seen, and in 1976, the lowest lying non-zero charmed (or open charmed) mesons, the D mesons ($c\bar{u}$, $c\bar{d}$ and their antiparticles) were detected at SPEAR[4]. Currently, several open charmed states are well established[5]: the D and D^* mesons, the D_s^+ (or F^+) meson, and the Λ_c^+ baryon.

Most of the data on charmed particles originated from the e^+e^- process. The success of charm production in the e^+e^- process is largely due to the excellent ratio of charm to non-charm events which is almost one when the center of mass energy is considerably above charm threshold. However, in hadroproduction this ratio is of the order of 10^{-3}. Even though the level of charm to background is much higher in e^+e^- interactions, some unique opportunities can be found in using hadron beams to search for charm. Absolute production rates of charm are orders of magnitude higher in hadronic collisions. Moreover, calculations of charm cross sections in hadroproduction can be made using lowest-order QCD perturbation theory since a large $c\bar{c}$ invariant mass (over 3 GeV) must materialize. Strong interactions involving the transfer of this large invariant mass squared, $Q^2 = m_{c\bar{c}}^2$, have a small running

coupling constant, α_s, which is given by:

$$\alpha_s = \frac{12\pi}{(33-2f)\ln(Q^2/\Lambda^2)} \simeq 0.25 \qquad (1)$$

where f is the number of flavors and where Λ is the QCD scale ($\simeq 0.1$ GeV). And so only the order α_s^2 diagrams need be considered (see Fig. 1.1). In the parton model, the total charm cross section in hadroproduction is given by

$$\sigma_{c\bar{c}} = \sum_{\substack{distinct \\ subprocesses}} \iint dx_1\, dx_2\, f_1(x_1,Q^2)\, f_2(x_2,Q^2)\, \hat{\sigma}(1+2 \rightarrow 3+4) \qquad (2)$$

where $\hat{\sigma}$ is a subprocess cross section. The subprocesses being considered include flavor-creation interactions (i.e. light quark-antiquark annihilation: $q\bar{q} \rightarrow c\bar{c}$, and gluon fusion: $gg \rightarrow c\bar{c}$) as well as flavor-excitation interactions (i.e. $qc \rightarrow qc$ and $gc \rightarrow gc$). The interacting partons from the initial hadrons have fractional momentum distributions f_1 and f_2 which depend on the parton momentum fractions x_1 and x_2 and weakly depend on the momentum transferred squared, Q^2. Little is known about the charm sea quark momentum distribution, but notice that if flavor excitation subprocesses are significant in charm hadroproduction, then the form of this distribution could be directly measured. To summarize, charm hadroproduction can provide a test for QCD predictions as well as possibly reveal details about the charm sea quark momentum distribution.

The production of closed charmed states (i.e. $c\bar{c}$ states) must be distinguished from the production of open charmed states (i.e. states consisting of non-zero charm). Experimental evidence indicates rather clearly that the production rates of closed charm can be interpreted as primarily originating from flavor creation subprocesses, i.e. $q\bar{q}$ annihilation and gg fusion (see Fig. 1.2). Calculations show that central production via gg fusion is the dominating subprocess at high energies[6] , and the x-dependence of the gluon momentum distribution function obtained in hadroproduction

can be expressed as $(1-x)^5/x$ which is the form derived from counting rules[7] and is compatible with results from charm photoproduction[8].

But hadroproduction of open charmed states is not well understood. Predictions of the total charm cross section that are based only on contributions from $q\bar{q}$ annihilation and gg fusion[6] are considerably smaller then experimental estimates of the total charm cross section as indicated by data[9] taken at $\sqrt{s}$ energies ranging from about 10 GeV to 60 GeV (see Fig. 1.3). Notice that the interpretation of results from various charm hadroproduction experiments must be done cautiously. Crucial input parameters from model-based calculations may change cross section estimates by a factor of 2 or more. Typically the systematic errors on the quoted cross sections are 50% or more. This is largely due to the large uncertainties in the branching ratios of most charmed particle decays and to the strong model dependence on results from those experiments which must extrapolate beyond their kinematic range of acceptance. A more detailed discussion of charm hadroproduction experiments (including recent results from Tevatron FNAL experiments) can be found in the concluding section of this dissertation.

The charm cross section predictions may be increased by incorporating flavor excitation as well flavor creation interactions. Using perturbative, non-scaling QCD, B.L. Combridge calculated the charm cross section contribution from each flavor creation and flavor excitation subprocess[10]. His results indicated that the contributions from flavor excitation are significantly greater than those from flavor creation; however, he points out that the flavor excitation values are uncertain because of their critical dependence on the charmed sea quark momentum distribution. Furthermore, he warns the reader that there exists a danger in double-counting by considering flavor creation and flavor excitation as separate processes. His approach was to assume

that the final states produced are sufficiently different, and thus, the processes can be considered distinct. Others have shown that the flavor excitation processes must be discarded when considering higher-order processes[11].

QCD calculations, such as those made by Combridge (in 1978), suggested that open charmed states can be produced centrally , i.e., charmed states can be produced predominately at rest in the center of mass system. So, like closed charmed states, open charmed states were expected to be produced copiously at low x_f. And indeed, a clear majority of charm hadroproduction experiments conducted at the CERN SPS and pre-Tevatron FNAL energies (about $\sqrt{s} \simeq 30$ GeV) observed centrally produced open charmed states[12]. Final charmed states produced from nucleon beams have an x-dependence of the form $(1- \mid x \mid)^n$ where $3 < n < 6$ which is consistent with central production[12] (even though a somewhat higher value for n is expected from gluon counting rules[7,13]). The total charm cross sections from these experiments range from about 10 μb to 80 μb with systematic errors typically on the order of 50%.

However, in 1979, diffractive charmed particle production was observed by several experiments near $\sqrt{s} \simeq 60$ GeV at CERN ISR[9,12,14-18]. Diffractive production (or forward production) suggests that charmed states can be produced at high x_f, i.e., charmed states can be produced predominately with large forward momentum in the center of mass system. Estimates of the total charm cross section from the ISR experiments (which used colliding proton beams) incorporated a flat x-dependence model for the observed forwardly produced Λ_c^+ and a more central x-dependence for the observed D mesons. These estimates averaged around 1 mb with systematic errors at least 50%. If the charmed baryon data were forced to fit a central model x-dependence, then the total charm cross section would be over 5 mb !

The exact interpretation of the ISR results is somewhat controversial[12,19]; but,

in general terms, two major conclusions from the ISR experiments, are in need of theoretical explanation:

1. The existence of forward charm hadroproduction.
2. The tremendous rise in the charm cross section as the c.m. energy increases from about 25 GeV to 60 GeV (see Fig 1.3, again).

Forward charm production may be resolved by some particular method of hadronization (i.e., an attempt to account for how the generated c (or $\bar{c}$) quarks combine with other quarks to produce the final hadronic states). A common assumption is to allow the QCD-evolved charm quarks to "dress" themselves with lighter quarks from the general hadronic sea, so that the c quark fragments into the final hadronic state with unit probability. If one further assumes, as Combridge did, that the QCD-evolved charm sea has a momentum distribution that favors a soft (or low) x-dependence, then one finds that the flavor excitation subprocesses generate final charmed states with a soft x-dependence, and thus their cross section contributions would be central and add in with the central contributions from the flavor creation subprocesses.

Perhaps the slow charm quarks do not encounter normal fragmentation, but rather recombine with the fast moving valence quarks in the incident hadrons to manifest forward final charmed states. This hadronization method is called the Recombination Model or the Spectator Model since the non-interacting quark (i.e., the "spectator" quark) remains with the initial valence quarks (see Fig. 1.4)[20–22]. Such a model is successful in explaining the leading production of the neutral strange baryon, Λ^0, but for charm this recombination scheme should be greatly suppressed since it is difficult for a slow moving massive quark to wind up carrying a large fraction of the final state momentum [20]. However, the ISR results clearly do not indicate a suppression of forward charm.

One approach used to account for the significant amount of forward production observed at ISR imposes a hard x-dependence on the charm sea quark momentum distribution[12,22]. This hard x-dependence is given a form similar to that expected for valence quarks. As $x \rightarrow 1$, valence quark momentum distributions are typically expressed as $(1-x)^3$, but some authors[22] have forced the charm sea quark momentum distribution to be as hard as $(1-x)$. Now a fast "spectator" charm quark can recombine with fast moving valence quarks to give a leading charmed hadron. And yet, within the framework of perturbative QCD, cross sections as large as 1 mb are still difficult to obtain with this scheme [12,23].

Even though the Spectator Model can explain how incoming protons (valence uud) can generate a forward "spectator" Λ_c^+ (udc), the model fails to explain how protons can generate a "spectator" D^+ ($c\bar{d}$) since none of the incoming valence quarks are contained in the charmed meson. One ISR experiment reported the observation of both forward Λ_c^+'s and D^+'s in pp collisions[14].

An alternative approach, called the intrinsic charm theory, does not have this difficulty in explaining the observation of forward Λ_c^+'s and D^+'s. According to Brodsky et al.[24] , "extrinsic" sea quarks are generated in association with a large Q^2 via standard QCD perturbative processes; but "intrinsic" sea quarks exist independent of any scattering process, and instead are generated through bound states dynamics involving gluon exchanges and vacuum polarization.

For example, Brodsky et al. have postulated that within the proton wave function there is a probability of order 1% to 2% of finding a hidden charm, Fock state component $|uudc\bar{c}\rangle$. Because the proton's constituents move with the same velocity at high energies, the massive c and $\bar{c}$ quarks carry a large fraction of the proton's momentum. Thus intrinsic charm quarks have a broad x-distribution, while the lighter

valence quarks have an x-distribution that peaks toward zero (see Fig. 1.5).

These intrinsic heavy-quark states are expected to easily fragment into open charm hadrons at high energy, low momentum transfer reactions, i.e., diffractive processes. So, colliding protons could give rise to forward Λ_c^+ (udc) baryons from $|uudc\bar{c}\rangle$ Fock states and forward D^+ ($c\bar{d}$) mesons from $|uudc\bar{c}d\bar{d}\rangle$ Fock states. Brodsky et al. argue that ψ ($c\bar{c}$) production from intrinsic charm should be greatly suppressed since the $c\bar{c}$ system would have to be generated as a color-singlet combination and with an invariant mass below the $D\overline{D}$ threshold. These authors estimate that a 1% to 2% level of intrinsic charm can give diffractive charm cross sections of the order 1 mb at the ISR energies ($\sqrt{s} \simeq 60$ GeV) ;however, this approach tends to overestimate the charm cross section found at $\sqrt{s} \simeq 25$ GeV by about an order of magnitude[24].

The tremendous rise in the total charm cross section as the center of mass energy increases from 25 GeV to 60 GeV is difficult to resolve in any model. Consider Eq. (2) and QCD central production. By expressing the parton momentum distributions f_1 and f_2 in the scaling form[25] $x^a(1-x)^b$ where $a \leq 0$ and $b > 2$, large contributions to σ occur when $x_1 \to 0$ and $x_2 \to 0$. The peaking of x_1 and x_2 near zero implies $x_{c\bar{c}} \equiv x_1 - x_2$ also peaks near zero, whereby charmed states are created near rest in the center of mass system. In light of the threshold condition $sx_1x_2 > 4M_D^2$ the charm cross section in the central model should grow with increasing s. As s increases charmed states can be produced with lower values of x_1 and x_2 where the distribution functions peak. Setting $m_c = 1.5$ GeV, Combridge calculations (which incorporate large contributions from flavor excitation subprocesses) indicate that $\sigma \simeq 20\mu$b at $\sqrt{s}$ = 25 GeV and $\sigma \simeq 150\mu$b at $\sqrt{s} = 60$ GeV. By using $m_c = 1.2$ GeV, the cross sections can be increased by about a factor of 4 to get closer agreement with the ISR data, but this overestimates the cross sections obtained at lower energies[9,10].

Diffractive production (whether originating from intrinsic charm or from other mechanisms) is also unsuccessful at explaining the observed cross section dependence on the c.m. energy. The empirical formula for high mass diffractive dissociation[24]:

$$\frac{d\sigma}{dM^2} = \frac{\sigma_0}{M^2} \qquad \text{gives} \qquad \sigma \propto \ln\left(\frac{0.1s}{4M_D^2}\right) \tag{3}$$

and thus,

$$\frac{\sigma(\sqrt{s} \simeq 60\text{GeV})}{\sigma(\sqrt{s} \simeq 25\text{GeV})} \simeq 2, \tag{4}$$

whereas, the data suggest the ratio should be at least 10.

The general features of charm hadroproduction discussed above can be summarized as follows:

1. The ratio of charm to non-charm events in hadroproduction is a few orders of magnitude lower than the e^+e^- process. But charm hadroproduction rates can be calculated using lowest-order QCD perturbation theory. Information about the nature (and form) of the charm sea quark momentum distribution function may be revealed.

2. Within perturbative QCD theory, closed charmed states can successfully be interpreted as the result of central production dominated by flavor-creation interactions (primarily gg fusion); however, the observed production rate in open charmed states is too large to be explained by fusion processes alone. Larger production rates are obtained by incorporating flavor-creation and flavor-excitation subprocesses.

3. Two center of mass energy regions reveal dramatically different production characteristics. Near $\sqrt{s} \simeq 25$ GeV, observations indicate that charm is predominately produced in the central region (i.e., low x_f) with estimates of the total charm

cross section in the range of 10μb to 80μb. Near $\sqrt{s} \simeq 60$ GeV, observations indicate that charm is predominately produced in the forward region (diffractively, high x_f) with total charm cross sections at about 1mb.

4. Theoretical models have been devised which generate forward charmed states from charm sea quarks with momentum distributions of the final state favoring a hard x-dependence. In one model the charm sea quark is QCD-evolved and recombines with fast moving valence quarks, while in another model, the charm sea quarks are associated with bound state hadron dynamics ("intrinsic" charm).

5. The tremendous rise in the charm cross section as the center of mass energy jumps from 25 GeV to 60 GeV has not yet been satisfactorily resolved by either central or diffractive production models.

This thesis will concentrate on measuring the cross section for the hadronic production of $\Lambda_c^+(2282$ GeV) by neutrons of an average energy of 565 GeV ($\sqrt{s} \simeq 33$ GeV). In addition some information on the production properties will be presented.

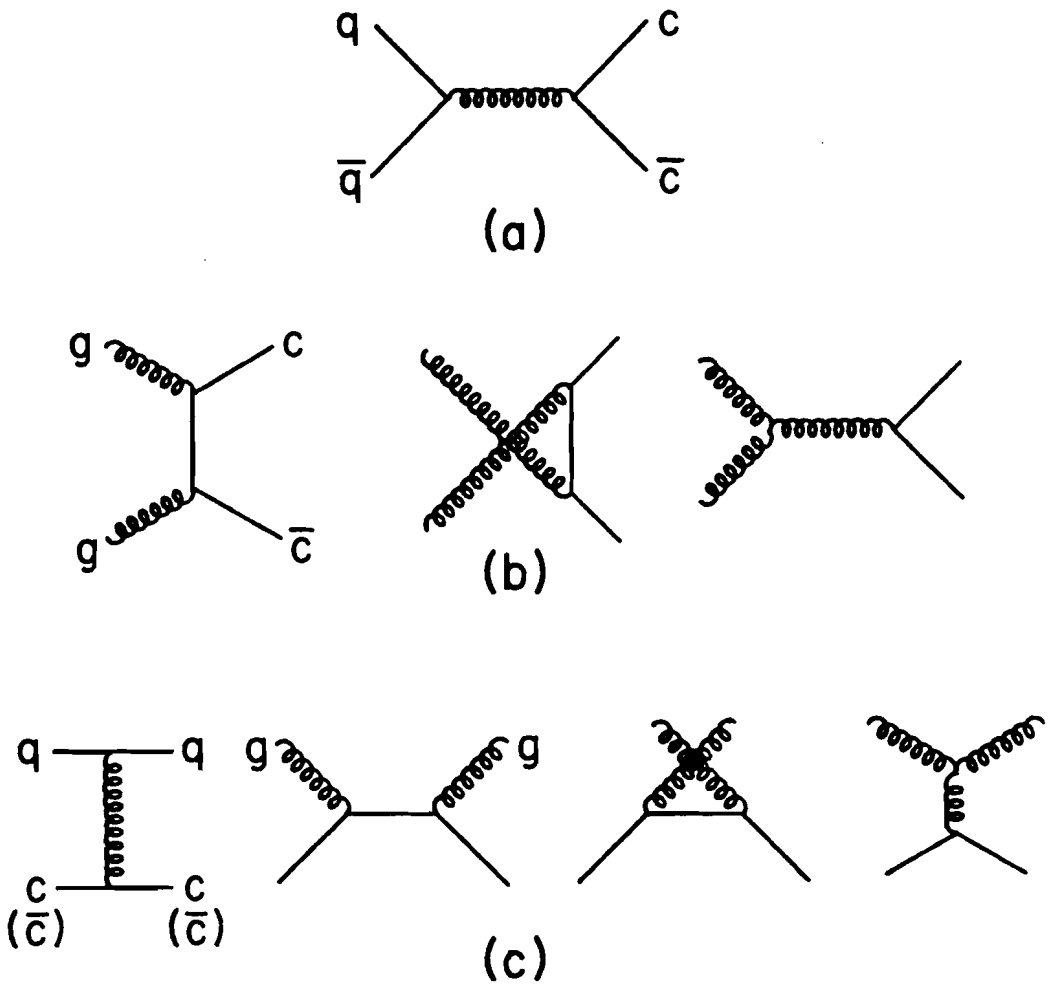

Figure 1.1 Lowest-ordered QCD diagrams:
(a) and (b) flavor-creation diagrams,
(c) flavor-excitation diagrams.

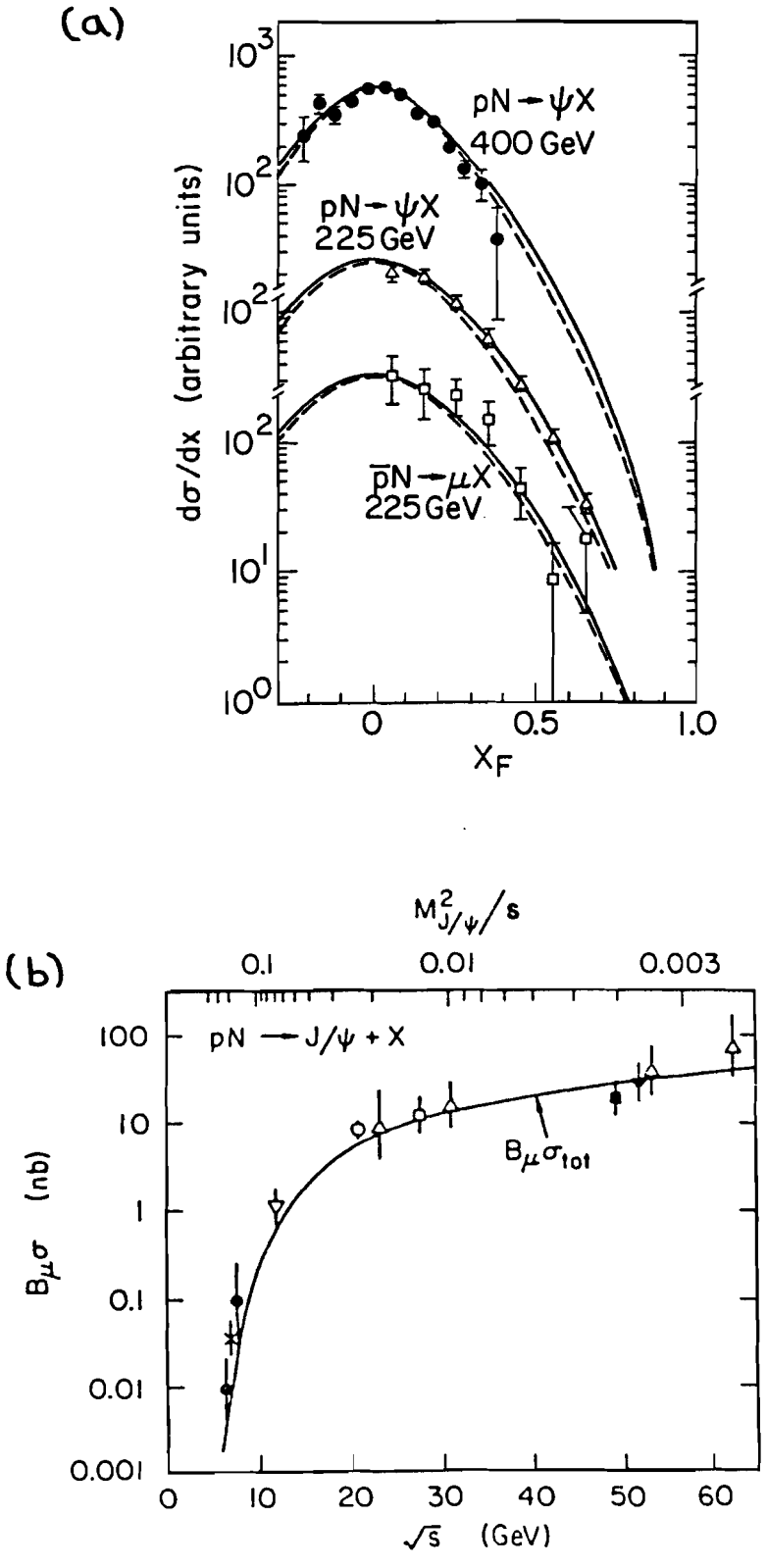

Figure 1.2 Hadroproduction of ψ's: gg fusion (dashed), $gg + q\bar{q}$ fusion (solid)[20].

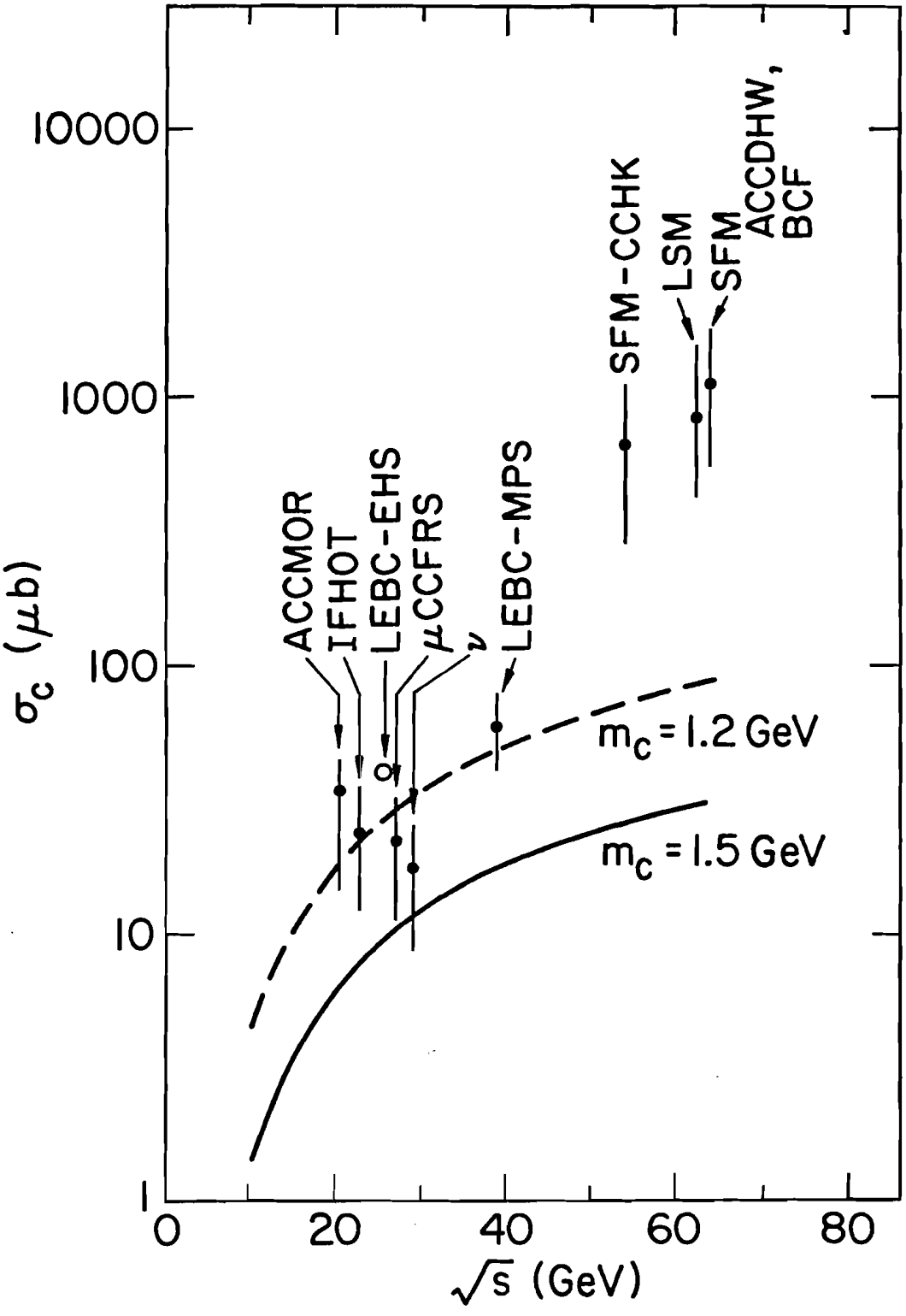

Figure 1.3 Total charm cross section vs. $\sqrt{s}$ (references: 9,12,36,38).

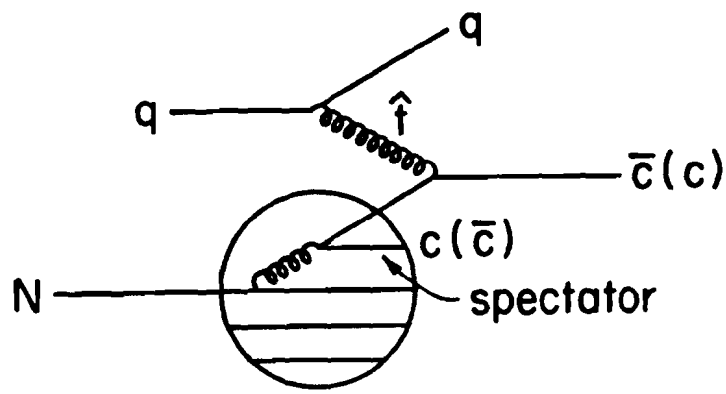

Figure 1.4 The Spectator Model .

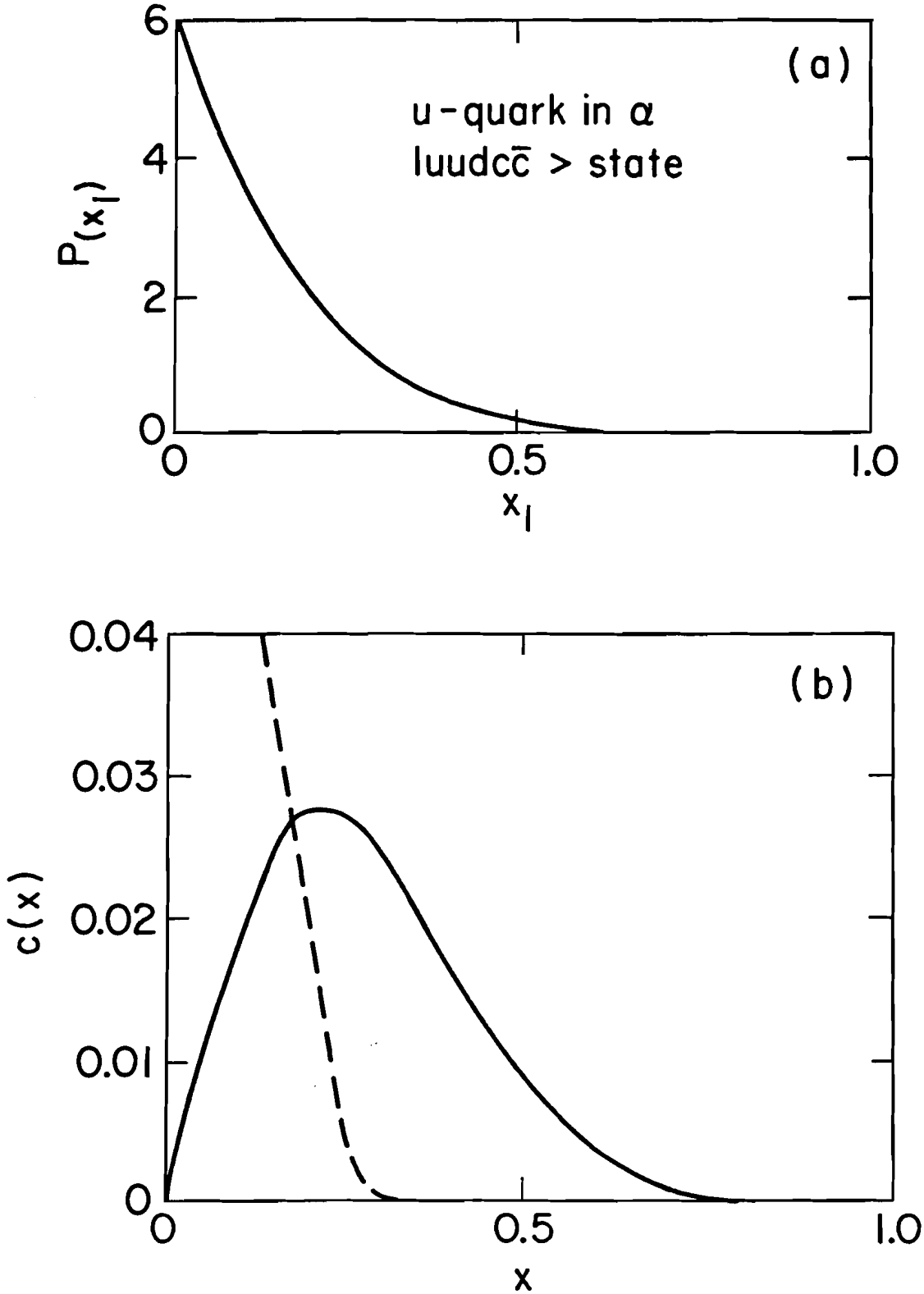

Figure 1.5 Quark x-distributions:
(a) light quarks in a $|\, uudc\bar{c} >$ state
(b) charm quark in a $|\, uudc\bar{c} >$ state (solid),
charm quark in a QCD-sea (dashed).

CHAPTER 2

The Experiment

2.1 Introduction

Experiment 400 was performed in the Proton East area at Fermi National Accelerator Laboratory from October 1983 to June 1984. One of the principal objectives of E400 was to study hadroproduction of charmed particles.

This chapter describes aspects of the experiment that are most relevant to the analysis which follows. The descriptions below include the beam, the experimental apparatus, the trigger, and the data acquisition system.

2.2 The Beam

Experiment 400 sought a beam consisting primarily of high energy neutrons incident on a fixed target. This beam was obtained in the Proton East broad band neutral beam line at Fermilab (Fig. 2.1). The neutral beam resulted from 800 GeV protons (and before February 1984, 400 GeV protons) incident on a beryllium target located 500 feet upstream of the experimental area. Magnets swept the non-interacting protons and the charged secondaries into a tungsten dump, leaving behind neutrons, K_L^0's, and photons from π^0 decays.

The energy spectra of the neutral particles in the beam have been discussed previously by those who performed experiments in the same beam line[26] (Fig. 2.2). The neutron spectrum peaks at 80% of the primary beam energy. The photon spectrum falls exponentially and is virtually non-existent at 50% of the beam energy. The K_L^0 spectrum is similar to the photon's but falls less steeply.

During normal data collection, the high energy photons were effectively removed from the beam by the insertion of six lead flippers (twelve radiation lengths) into one

of the sweeping magnets. The emerging photons would then typically have energies less than one MeV. The lead also attenuated the hadronic components by 50%. The K_L^0's were essentially eliminated by their poor angular acceptance and by the trigger requiring each event to have a certain minimal energy (roughly half of the incident proton beam energy).

Along the beam line there were three sets of steel collimators which eliminated beam halo and gave rise to a 0.6 cm x 0.6 cm beam spot size on the experiment's target. When desired, hadron steel shielding was installed into the beam line for special muon test runs which were used to test the apparatus.

2.3 The Experimental Apparatus

A schematic drawing of the experimental apparatus is shown in Figures 2.3 (top view) and 2.4 (side view). Table 2.1 gives the center locations, longitudinal extents, and the transverse active areas of various E400 devices and counters. Charged particle tracking and momentum were obtained by a system of five multiwire proportional chambers (MWPC's) and two dipole magnets (having opposite polarity and effective kicks of -.41 GeV/c and .58 GeV/c, such that positive particles would bend upward as they pass through the second magnet, M2). Particle identification was made possible by the installation of three Čerenkov counters, lead glass, and muon hodoscopes. Energy sums were formed from the lead glass, the hadron calorimeter, and a beam dump calorimeter. The sections below describe the apparatus in more detail.

The Target

The target consisted of longitudinally segmented slabs of W, Si, and Be (Fig. 2.5). The combined neutron absorption length of W (0.31%), Si (0.63%), and Be(0.98%) was 1.92%. The combined radiation length was 12.8%, but most of the radiation length (8.6%) was found in W, the most upstream target slab so that Coulomb scattering

effects were minimized. The Si segments comprised a "live" solid state detector. The hope was that some charmed particles would have long enough lifetimes to give rise to a discernable secondary vertex a few millimeters downstream of the primary vertex. An indication of such a secondary vertex could be a jump in the number of minimum ionizing particles detected in different Si target segments. This particular use of the "live" target plays no role in the analysis that is presented later. The most downstream Si segment was demanded "on" in the main event trigger to help insure a primary interaction in the target region.

The MWPC System

Experiment 400 chose a left-handed coordinate system with Z positive being downstream and Y positive being vertically up. The origin of the coordinate system was chosen to be at the center of the second magnet (M2). Each of the five multi-wire proportional chambers (P0 - P4) consisted of three planes of wires, one vertical plane (X plane), and two nearly horizontal planes of wires (V, U planes). The space coordinates V and U were related to the space coordinates X and Y by the following: $Y = (U + V)/(2\cos\theta)$ and $X = (U - V)/(2\sin\theta)$, where $\tan\theta = 0.2$. The geometric specifications for the five MWPC's are given in Table 2.2.

The MWPC's gave both single hit wire and band hit wire information. Each plane of wires had 32 bands of wires with the wires being grouped in multiples of 8, 16, 24, or 32. The larger bands of wires covered regions that expected fewer hits per unit area. The or'd output of the bands of wires was used as a multiplicity selection in the trigger. The band signals from all the chambers also provided drift arrival times through TRM's (Time Recording Modules).

The Vertex Chamber

The vertex chamber (which is also called the D5) consisted of 9 planes of wires,

each with 250 μm spacing. The active area of the chamber was 50 mm by 50 mm. The planes were arranged in triplets separated by 5.25 cm. Each plane of wires in a triplet had a different direction: one X plane (vertical wires), one V plane, and one U plane (such that 60^0 existed between any two different wire directions). The planes within each triplet were separated by 0.40 cm. The distance from the center of the vertex chamber to the center of the Be target was 11.91 cm. The chamber operated at 2 atmospheres pressures and at approximately 5.2 kilovolts. The vertex chamber is described in more detail by the designers (see reference # 27).

Čerenkov Counters

Three segmented Čerenkov counters C0, C2, C3 provided most of the particle identification (Fig. 2.6, 2.7, 2.8 and 2.9). (For historical reasons, no counter was named C1). Each Čerenkov counter had 34 cells. The transverse segmentation of C2 and C3 cells were identical (Fig. 2.7).

C0 was filled with isobutane (for a major portion of the run) and was located between P0 and P2. C0 had flat primary mirrors angled at 45^0 with respect to the Z axis. Light collection was enhanced by the installation of mirror collection cones in front of each photomultiplier tube. C0 had a radiator length that ranged from 12 - 26 inches and π/K/p thresholds of 3.0/10.6/20.3 GeV/c.

C2 was filled with 80% helium and 20% nitrogen and positioned between P3 and P4. To prevent helium from diffusing through the tubes, the windows of the tubes were flushed with nitrogen. Light collection was done with segmented focusing mirrors such that each tube had a corresponding mirror. C2 had 180 inches of radiator and π/K/p thresholds of 11.7/41.4/78.8 GeV/c. Just downstream of the mirror plane of C2 there was a bank of hodoscope scintillation counters such that each cell had a corresponding counter. A later section in this chapter will reveal how these hodoscope

counters played a role in triggering for heavy particles (i.e., kaons and protons).

C3 was filled with nitrogen and positioned between P4 and the H x V counters. Like C2, C3 had segmented focusing mirrors. C3 held 80 inches of radiator and had π/K/p thresholds of 6.4/22.4/42.6 GeV/c.

Calorimetry Devices

An energy sum which was used in the trigger was established from the appropriately gain balanced tubes of the lead glass (LG) and the hadron calorimeter (HC). The beam dump calorimeter (BDC) was used to collect energy from forward particles passing through the center hole of the HC, but this energy was not incorporated into the energy trigger.

The lead glass system which was located just downstream of C3 consisted of 2 arrays of lead blocks (Fig. 2.10). The central array (with a 2.5" x 5.0" hole) held 82 2.5" x 2.5" x 23.0" SF2 glass blocks (each with 20.8 radiation lengths and 0.63 interaction lengths). The outer array held 62 6" x 6" x 18" SF5 glass blocks (each with 18.1 radiation lengths and 0.55 interaction lengths). Every block had a corresponding photomultiplier tube.

Downstream of the lead glass was the hadron calorimeter which embodied ten banks of 0.25" thick scintillation pieces sandwiched between 1.75" thick steel plates (Fig. 2.11). Energy from charged tracks that passed through the circular hole (radius $\simeq$ 3.81 cm) of the hadron calorimeter were collected in the beam dump calorimeter which was located just downstream of the hadron calorimeter. The beam dump calorimeter consisted of 19 8" x 8" x 1" blocks of tungsten interspaced with 8" x 8" x 0.25" scintillation pieces. The HC and BDC each gave 6 interaction lengths. The scintillation light was collected through a system of light guides and photomultiplier tubes.

Muon and Electron Counters

Muon identification was made possible by the installation of 2 long blocks of steel, 2 banks of scintillation counters, and 2 stacks of proportional drift tubes (Figs. 2.12 and 2.13). Between the blocks of steel a bank of 20 horizontal scintillation counters and a horizontal stack of 72 drift tubes was located. Downstream of both blocks of steel a bank of 20 vertical scintillation counters and an additional horizontal stack of 72 drift tubes were installed.

The outer electrophotometer (OE), which was positioned just upstream of M2, operated with the hopes of providing electron identification. The OE (see Fig. 2.14) included 60 scintillation counters sandwiched between lead (giving 16 radiation lengths).

The analysis presented here does not make use of the muon or electron identification provided by the counters just described.

2.4 The Trigger and Data Acquisition

A large combinatorics from high multiplicities in hadroproduction can lead to a poor signal to background ratio. In order to improve this ratio some experiments frequently will choose a highly selective, signal enhancing trigger. However such a trigger could result in a bias away from one or more theoretical production models. To avoid such a bias, one could use a loose trigger with a data acquisition system that was designed to quickly record large quantities of data; thus reserving the many possible event selection cuts for a careful off-line analysis study. This was the course chosen by Experiment 400.

The 1500 data tapes (6250 bpi) collected from E400 includes nearly 60 million events with average multiplicities of 9 tracks. About 10% of this data were accumulated under a master gate trigger (Pin 2) which merely required the coincidence of

the T1 counter (which covered part of the opening to M1) and a 2-body count in the H x V scintillation counters (which were located just downstream of P4) (Fig. 2.15). Satisfying the requirement of $(HxV)_{2Body}$ indicates that there exists at a set of overlapping H and V signals in one quadrant plus an additional H or V signal in the same quadrant or an additional set of overlapping H and V signals in a different quadrant (see Fig. 2.16 for a logic diagram). The rest of the data were collected under a trigger (Pin 4) requiring at least two 5 chamber tracks and minimum total energy sum at about half the incident proton beam energy. The incident beam energy for the first third of the data was 400 GeV and for the remainder of the data the energy was 800 GeV.

The triggering was determined by the master gate coincidence between a signal from the T1 counter and a signal from the $(HxV)_{2Body}$ requirement. A logic box (called the "Confusion Logic") accepted the input signals from these counters (Fig 2.17). If one signal was "on" (but not both), then the logic box would flag the on-line computer to prevent any new triggers from being generated until the various detectors could recover. This resulted in a 100 nsec deadtime, i.e., the amount of time during a spill in which the experiment would not accept an event trigger. If both signals were "on" a master gate was generated, and the Confusion Logic would flag the computer to prevent any new triggers for 300 nsec until the slower logic (called DC logic) could decide if the event would be processed further.

The DC logic determined 16 buslines that were set "true" based upon information provided by scintillation counters, wire bands, or energy sums. Some combination of these buslines (or their vetos) were required in the pin logic modules (Fig. 2.18). Thus the trigger was established by selecting events which passed certain pins. Each pin logic module was prescaled so that events passing a highly selective pin trigger could

have been favored over events passing a loose pin trigger.

The relevant buslines were as follows:

B1: The median number of wire band hits taken from the individual hit totals in P0, P1, and P2 must be at least 4. Also the minimum number of band hits taken from the totals in P3 and P4 must be at least 2. When both of these conditions were true, then minimal multiplicity was satisfied.

B2: Si 33 "on". This established a primary interaction in E400's target fiducial region to maximize the coverage by the vertex chamber.

B7: ETOT PAD (Pulse Area Digitizer) ≥ 4. Each PAD count was about 40 GeV. After the primary proton beam energy was doubled to 800 GeV, the signals entering the PAD were attenuated by a factor of 2. ETOT was the energy sum from the appropriately gain balanced tubes of the lead glass and the hadron calorimeter.

B13: The maximum number of wire band hits taken from the individual band hit totals of P3 and P4 must be less than 8. This busline rejected events with high multiplicities.

B16: PS > 0. This was true for any input into the Confusion Logic box and was prescaled by a factor of 1/1024 (while still in the logic box). This unbiased busline was used in monitoring such things as deadtime.

These buslines entered the pin modules and established the following triggers (and their corresponding prescales):

PIN 2 = $\overline{\text{B16}}$ with a prescale factor of 1/128

PIN 4 (Hi Mult) = B1 $\cdot$ B2 $\cdot$ B7 $\cdot$ $\overline{\text{B16}}$ with no prescale

PIN 4 (Lo Mult) = B1 · B2 · B7 · B13 · $\overline{\text{B16}}$ with no prescale

where approximately 10% of the data were PIN 2 and 90% were PIN 4 (Hi Mult). The last 20% of the data used PIN 4 (Lo Mult) rather than PIN 4 (Hi Mult).

The maximum number of wire hits that could be stored was 255. This value was limited by the MWPC hardware encoder. Events that exceeded this wire hit limit were not written to tape but were monitored. The level of such events was a few percent per spill. During the PIN 4 (LO MULT) data taking, the maximum number of wire hits was intentionally set to 208 by modifying bits on the encoder.

Once the pin triggers were satisfied, the digitized event record was read out as blocks of data into four 2 Mbyte memories. The read-out system for the data aquisition system was named the TRACE (Tevatron Revised Automatic Control Entry) system (see Fig. 2.19). Additional information about this data acquisition system can be found elsewhere[28]. Before February, 1984, the accelerator duty cycle gave shorter more frequent spills, and a memory one eighth the size was adequate.

While the events were being read out a fast trigger processor (called the M7) was in operation. The M7 flagged events as being "good" based upon some fast tracking and particle identification. Specifically, the M7 searched for a track which satisfied the following:

M7 trigger = $\overline{\text{C2}}$ · C2H · C3 · (P > 22 GeV)

where the Čerenkov information was provided by the coincidence registers (established from signal discriminators) and the momentum estimates came from the wire bands. Note, C2H refers to the scintillation counter located just downtream of the corresponding C2 cell. PIN 4 events which failed the M7 trigger were aborted at the readout level. All PIN 2 events were kept and flagged as to whether or not the M7

trigger was satisfied. This trigger was designed to enhance the selection of events with a high momentum, unambiguous charged kaon. The efficiency of this trigger will be determined in a later section where it becomes necessary to normalize the data to obtain a cross section.

The deadtime was monitored by counting scalers which were read out at the end of each spill. The PIN 2 SD scaler counted only "live" master gates. A "computer busy" signal, which blocked counts from entering the PIN 2 SD scaler, was generated by any source of deadtime: the M7 trigger time, the TRACE busy time (read-out time), the memory full time, the off-spill time, the ADC digitization recover time, and the clear time after an aborted event. The largest readout deadtime of about 300 μsec per event was set by the largest block of data which included 256 ADC's plus a few flag words. Digitization gave an additional deadtime of 100 μsec. These deadtimes were identical for all events (PIN 2 or PIN 4). Additional deadtime from the M7 was minimized by overlapping the M7 "thinking" time with the readout. However, occasionally the M7 was slower than the readout. PIN 4 events (with higher multiplicities than PIN 2) slowed down the trigger processor more than PIN 2 events. In any case, the overall livetime was monitored by the ratio of counting scalers that were read out at the end of each spill, so that the livetime was determined by the ratio of the number of counts satisfying the master gate when "live" (PIN 2, SD) to the total number of counts satisfying the master gate (MG $>$ 1, No Dead Time).

Table 2.1 E400 geometry.

DEVICE	Z POSITION* (cm)	Z LENGTH (cm)	ACTIVE AREA
D5 Triplet No. 1	6.67	0.82	50 mm x 50 mm
D5 Triplet No. 2	11.91	0.82	50 mm x 50 mm
D5 Triplet No. 3	17.16	0.82	50 mm x 50 mm
T1 Counter	30.48	0.64	7.62 cm x 7.62 cm
M1 Magnet	132.3	101.6	38.1 cm x 84.0 cm
M1 Plate Hole	50.54	12.7	35.6 cm x 20.3 cm
P0 Center	221.5	—	44.7 cm x 70.4 cm
P1 Center	307.8	—	49.0 cm x 78.2 cm
C0 Center	381.0	66.1	71.1 cm x 91.5 cm
P2 Center	443.5	—	76.7 cm x 112.8 cm
OE Counter	504.7	55.9	112 cm x 142 cm
OE Hole	504.7	55.9	50.8 cm x 35.56 cm
M2 Magnet	632.5	182.9	50.8cm x 61.0 cm
Oμ Counter	758.8	0.64	152.4cm x 185.4 cm
Oμ Hole	758.8	0.64	50.8 cm x 61 cm
P3 Center	795.0	—	83.3 cm x 112.8 cm
C2 Center	1045.7	460.0	104 cm x 168 cm
CH2 Counter	1291.6	0.64	104 cm x 168 cm
P4 Center	1320.8	—	100.6 cm x 153.6 cm

* Z position is measured from the Be target center to the device center.

Table 2.1 (continued)

DEVICE	Z POSITION* (cm)	Z LENGTH (cm)	ACTIVE AREA
C3 Center	1437	203	104 cm x 168 cm
H x V Counters	1549	0.64	106.6 cm x 160 cm
LG Device	1592	58.4	107 cm x 167.6 cm
LG Hole	1592	58.4	6.35 cm x 12.7 cm
HC Device	1772	198.7	157 cm x 198 cm
HC Hole	1772	198.7	15.2 cm x 15.2 cm
BDC Device	1901	60	20.3 cm x 20.3 cm
P-Tubes Upstream Bank	2108	10.2	152 cm x 227 cm
μH Counters	2270	0.64	180 cm x 224 cm
P-Tubes Downstream Bank	2353	10.2	152 cm x 227 cm
μV Counters	2376	0.64	180 cm x 224 cm

Table 2.2 MWPC geometry.

Plane	Aperture	Distance from M2	Number of wires	Wire spacing
P0X	17.6" x 27.7"	-161.8"	224	.07872"
V			352	.07874"
U			352	.07874"
P1X	20.4" x 30.8"	-127.8"	256	.08021"
V			384	.08021"
U			384	.08021"
P2X	30.2" x 44.4"	-74.4"	384	.07880"
V			576	.07876"
U			576	.07876"
P3X	32.8" x 44.4"	64.0"	416	.07878"
V			576	.07873"
U			576	.07873"
P4X	39.6" x 60.5"	271.0"	336	.11818"
V			768	.07873"
U			768	.07873"

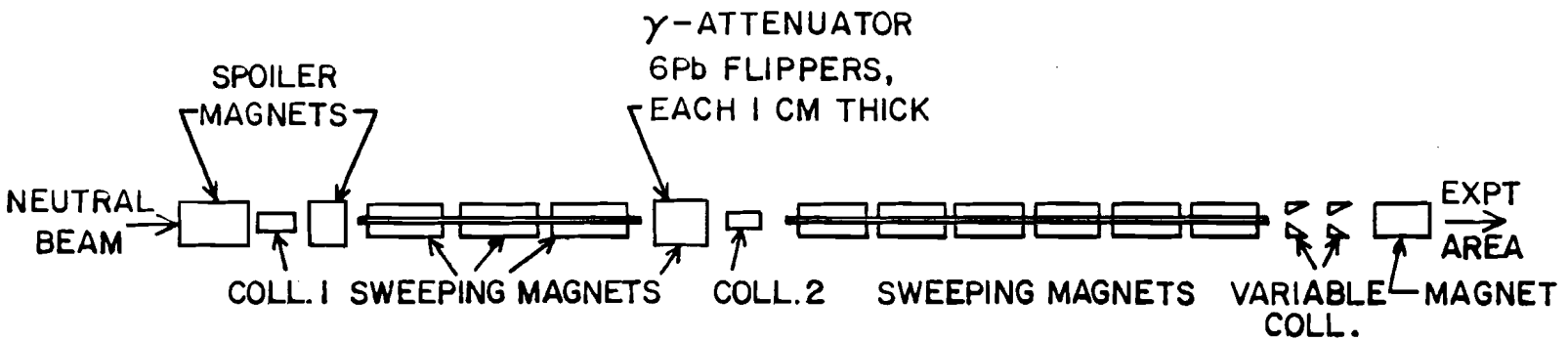

Figure 2.1 Neutral beamline.

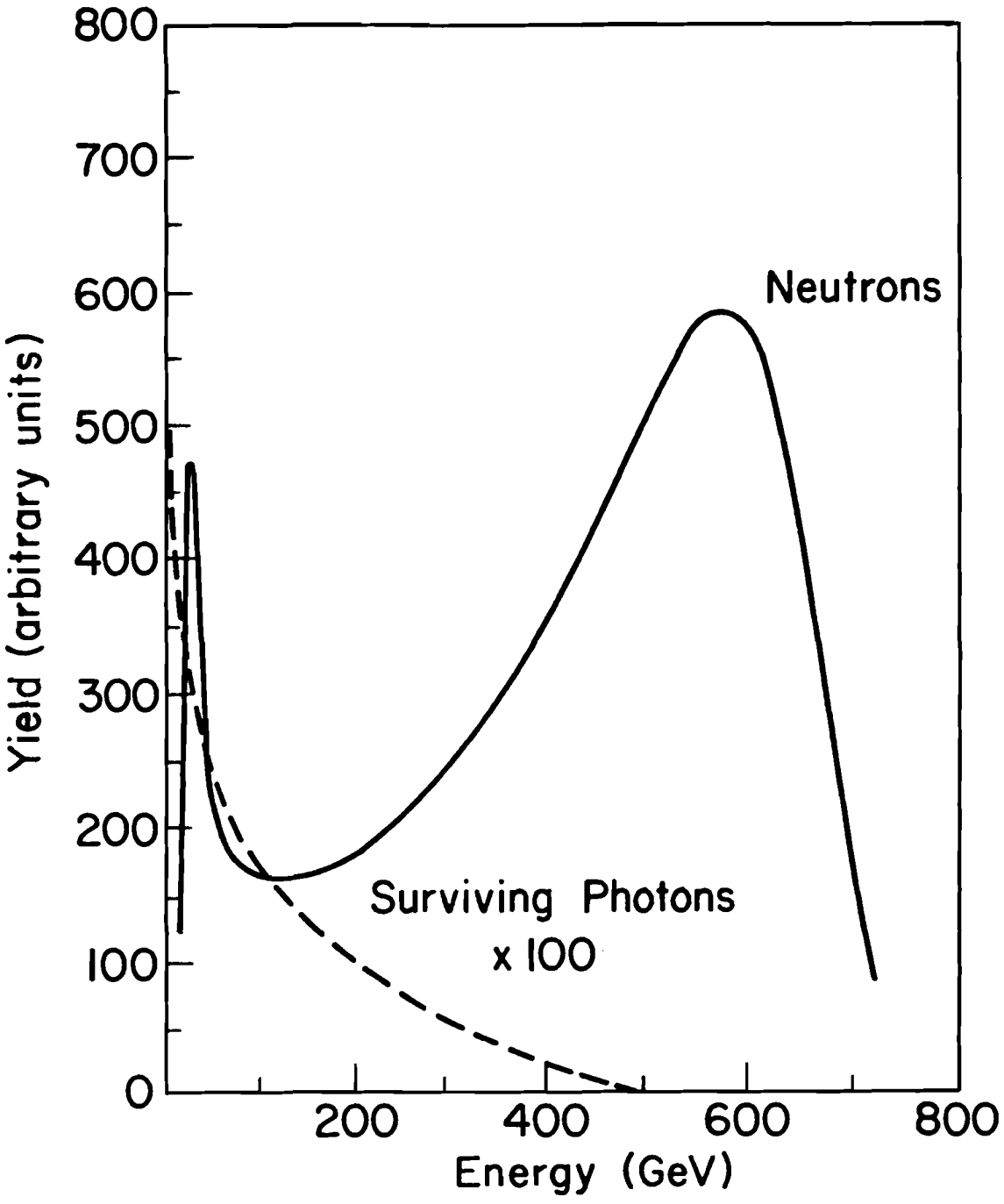

Figure 2.2 The neutron energy spectrum.

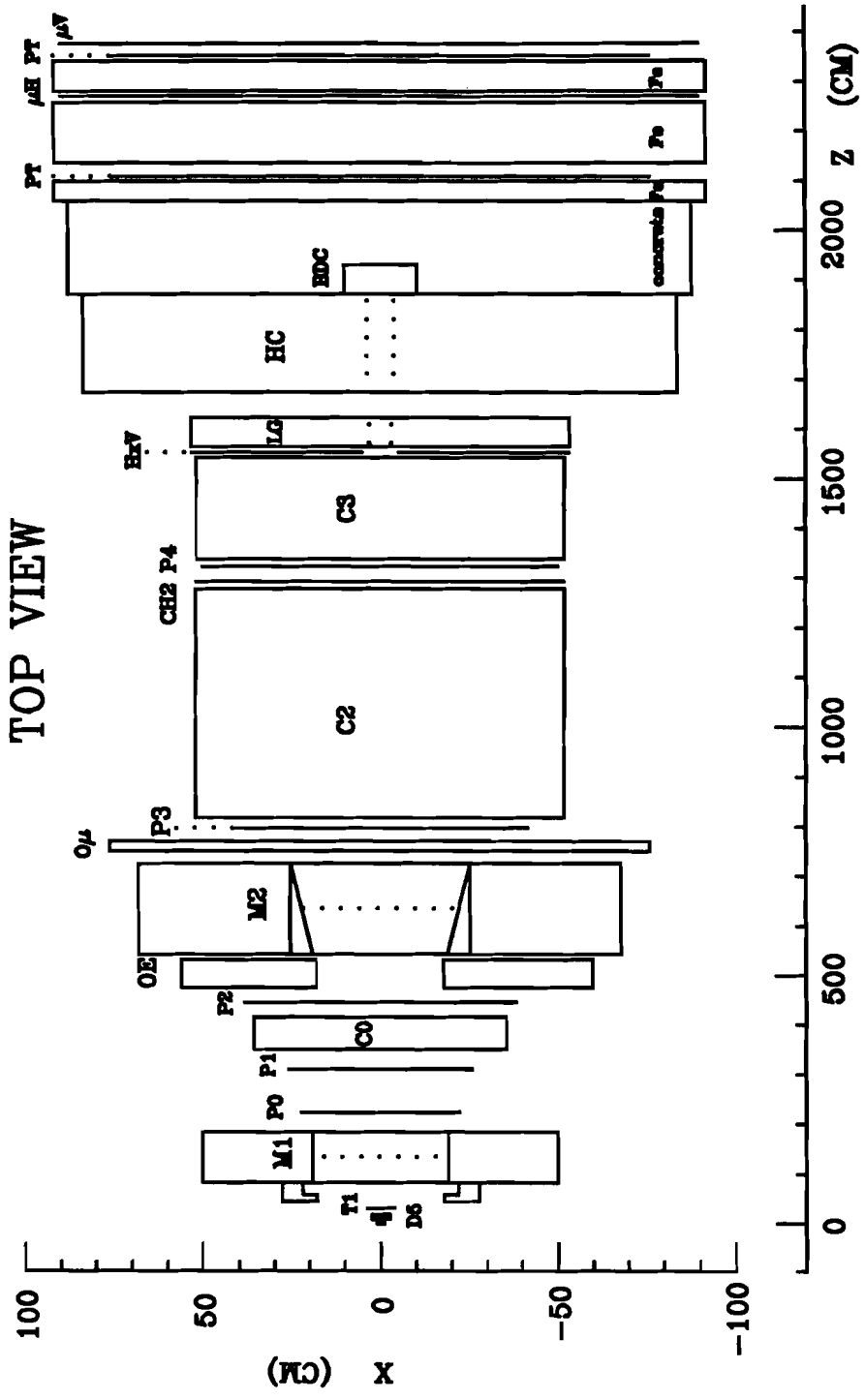
TOP VIEW
μV
μE PT
PT
Fe
Fe
concrete Fe
EDC
HC
EnV
LG
C3
CH2 P4
C2
P3
Oμ
M2
OE
P2
C0
P1
P0
M1
T1
D2
100
50
0
-50
-100
X (CM)
0
500
1000
1500
2000
Z (CM)

Figure 2.3

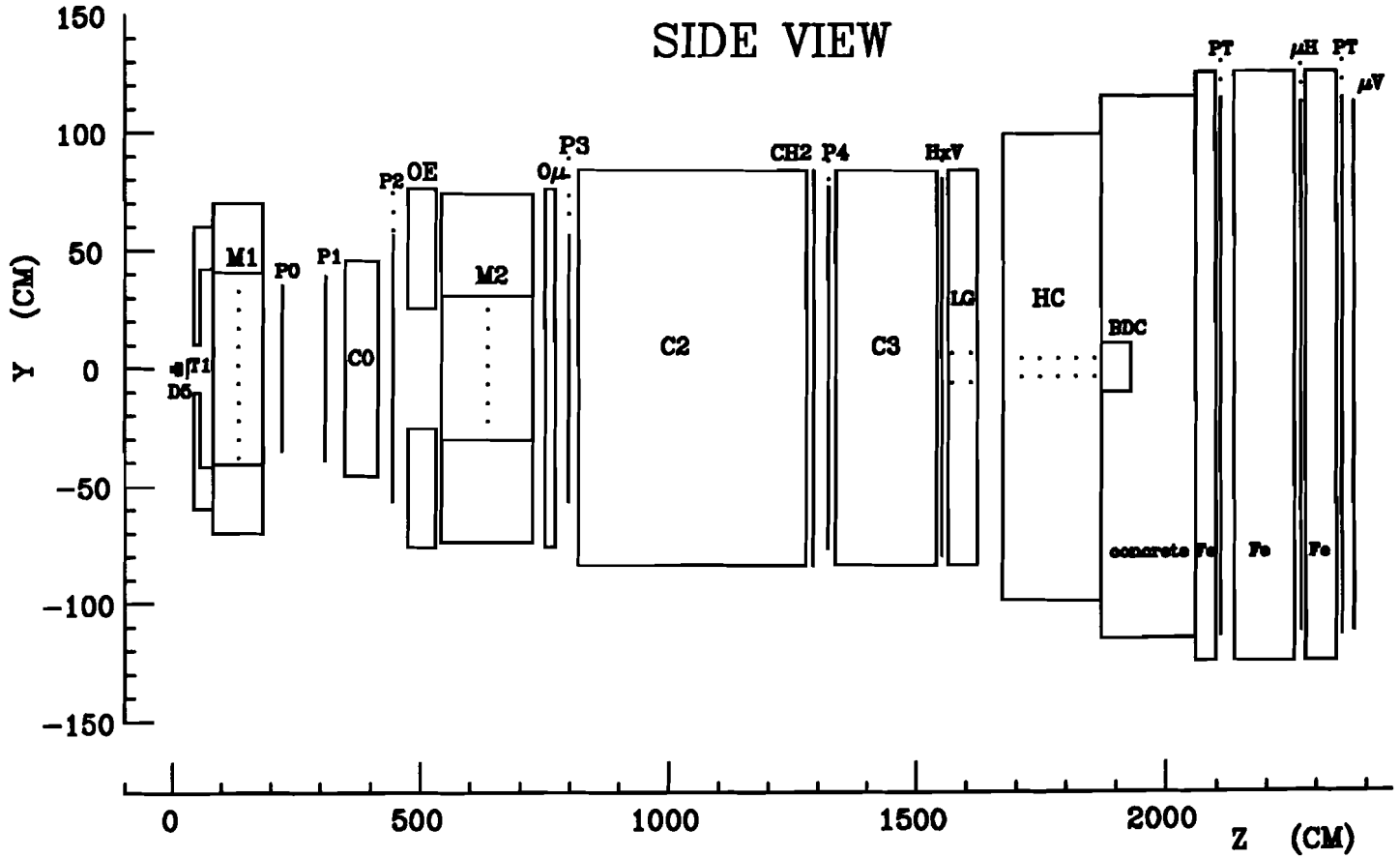
SIDE VIEW
150
100
50
0
−50
−100
−150
Y (CM)
0
500
1000
1500
2000
Z (CM)
T1
D5
M1
P0
P1
C0
P2
OE
M2
Oμ
P3
C2
CH2
P4
C3
HxV
LC
HC
EDC
concrete
Fe
PT
μH
PT
μV
Fe
Fe

Figure 2.4

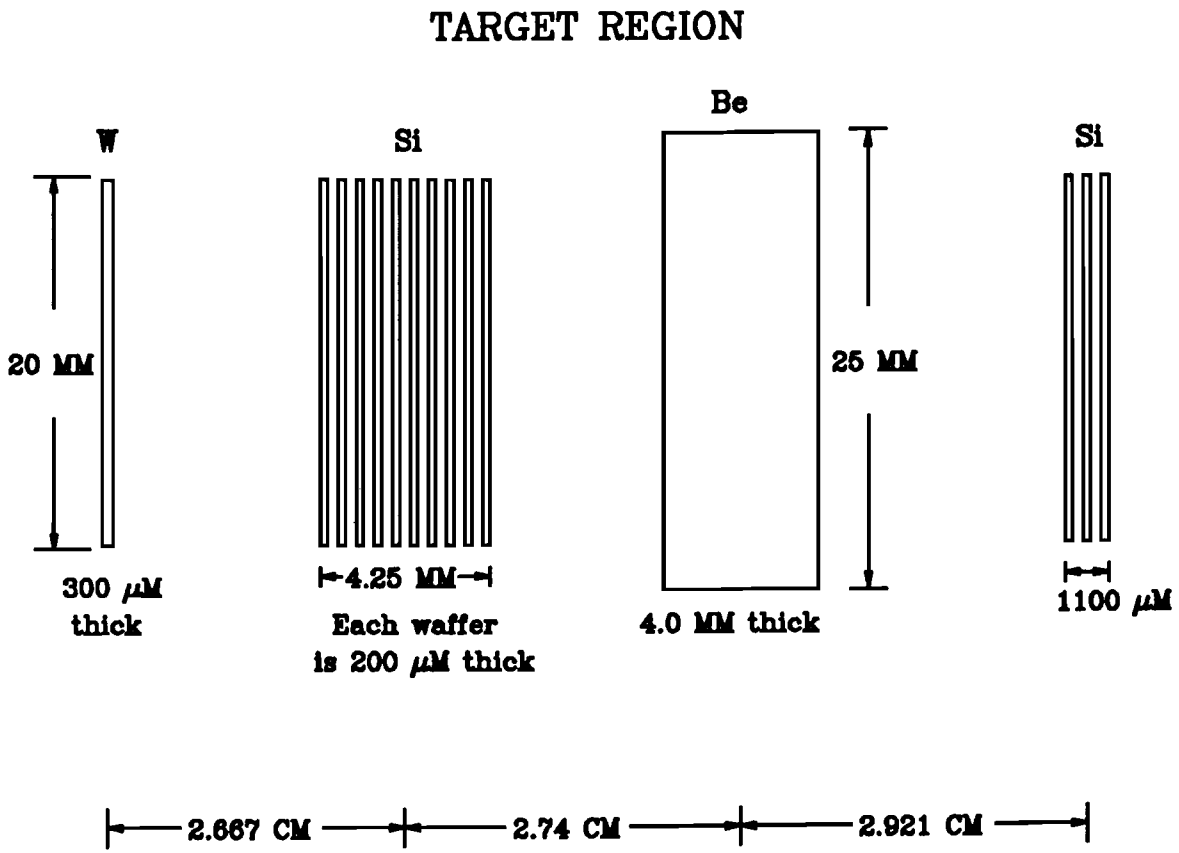
TARGET REGION
W
Si
Be
Si
20 MM
25 MM
300 μM
thick
4.25 MM
Each waffer
is 200 μM thick
4.0 MM thick
1100 μM
2.667 CM
2.74 CM
2.921 CM

Figure 2.5

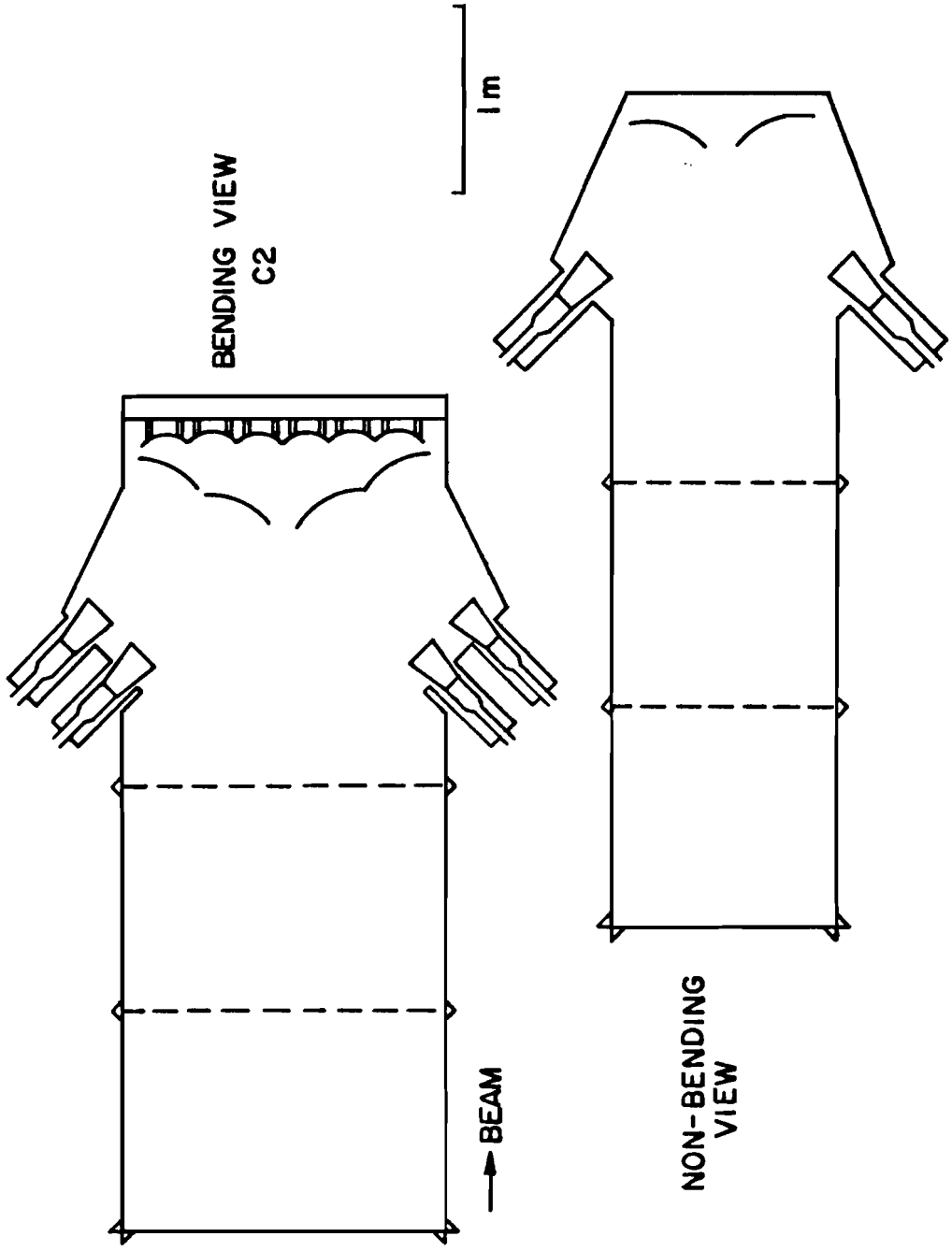

Figure 2.6 C2 design.

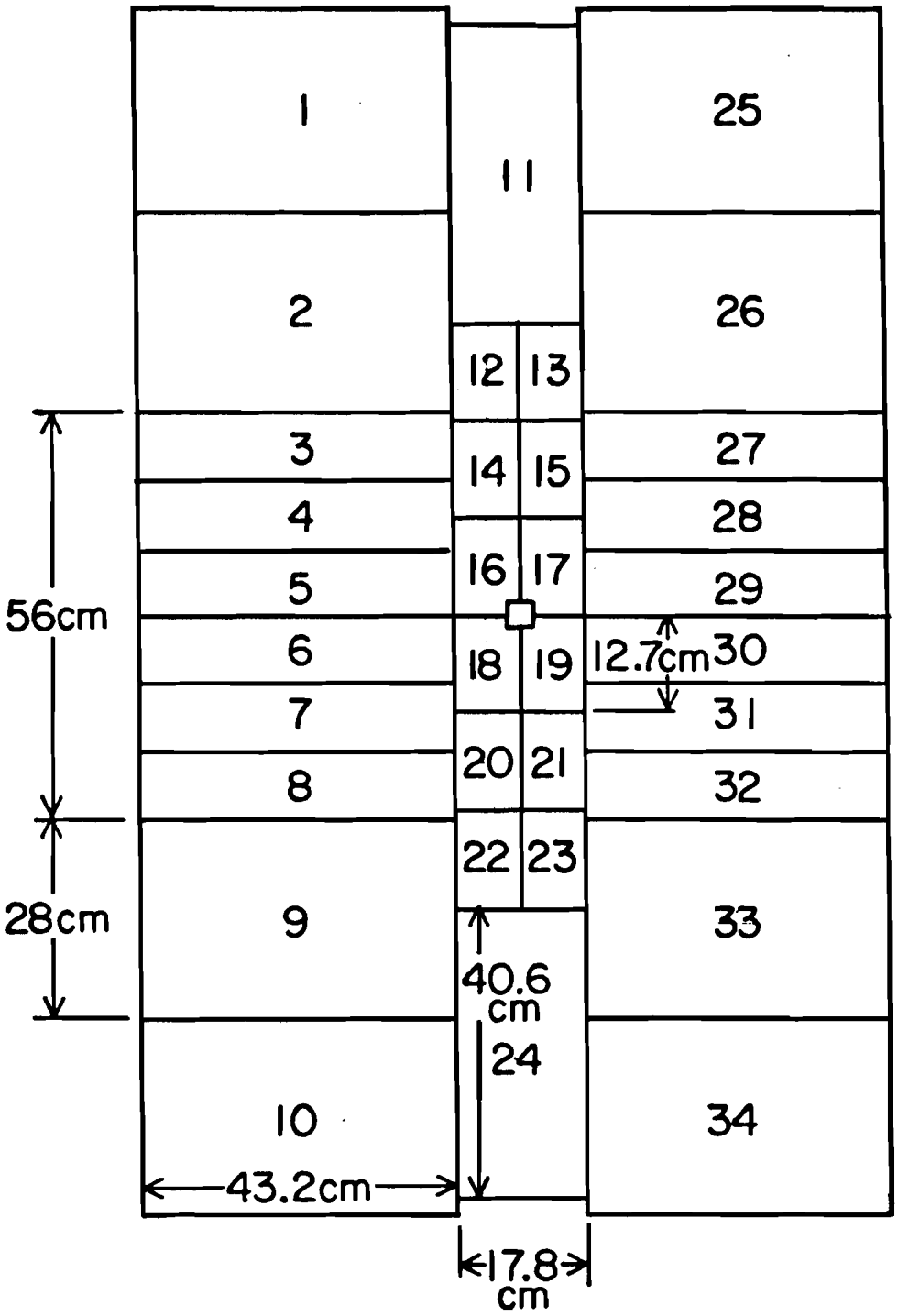

Figure 2.7 C2 and C3 mirror plane (XY projection, beam's eye view).

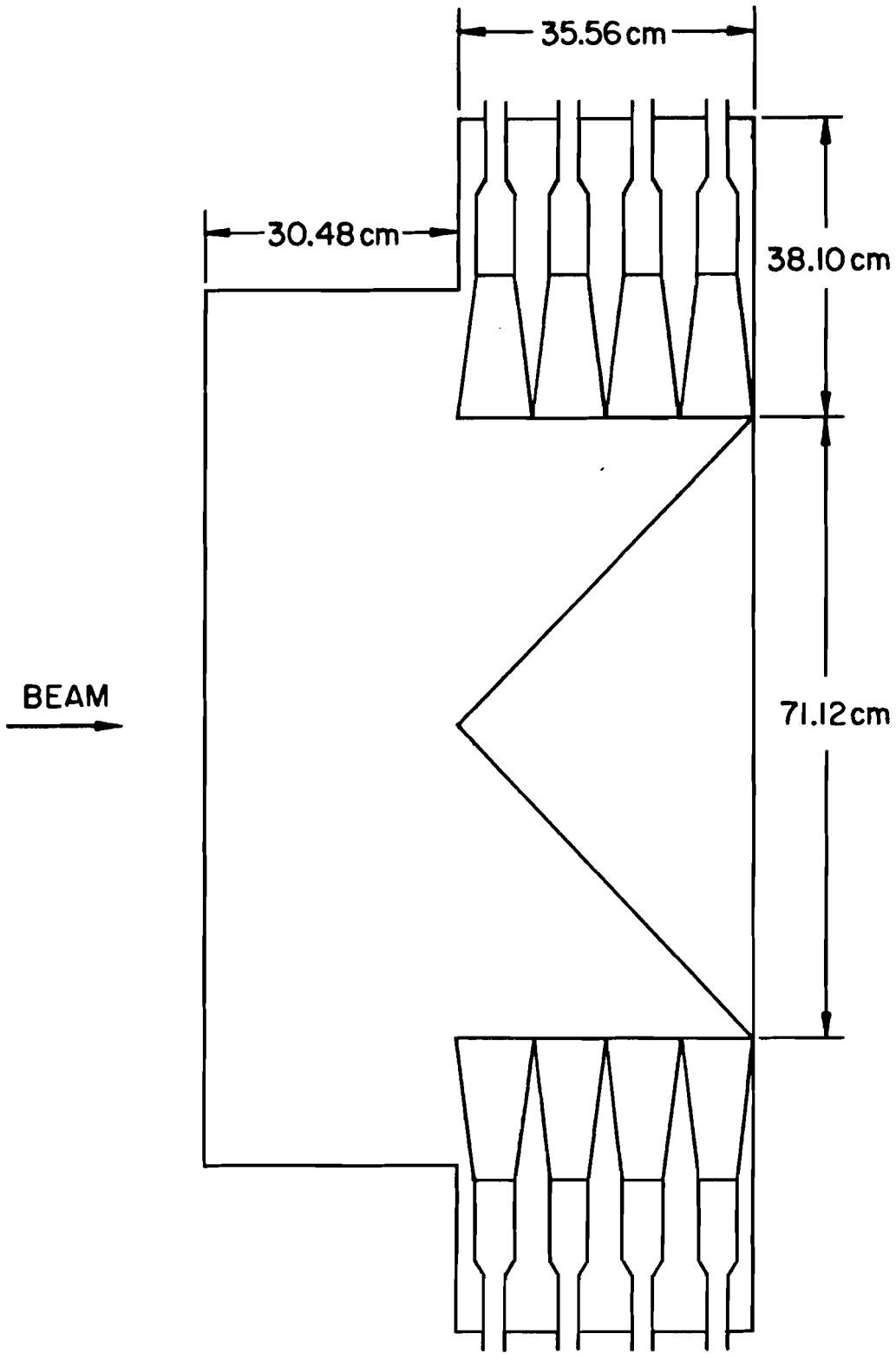

Figure 2.8 C0 design.

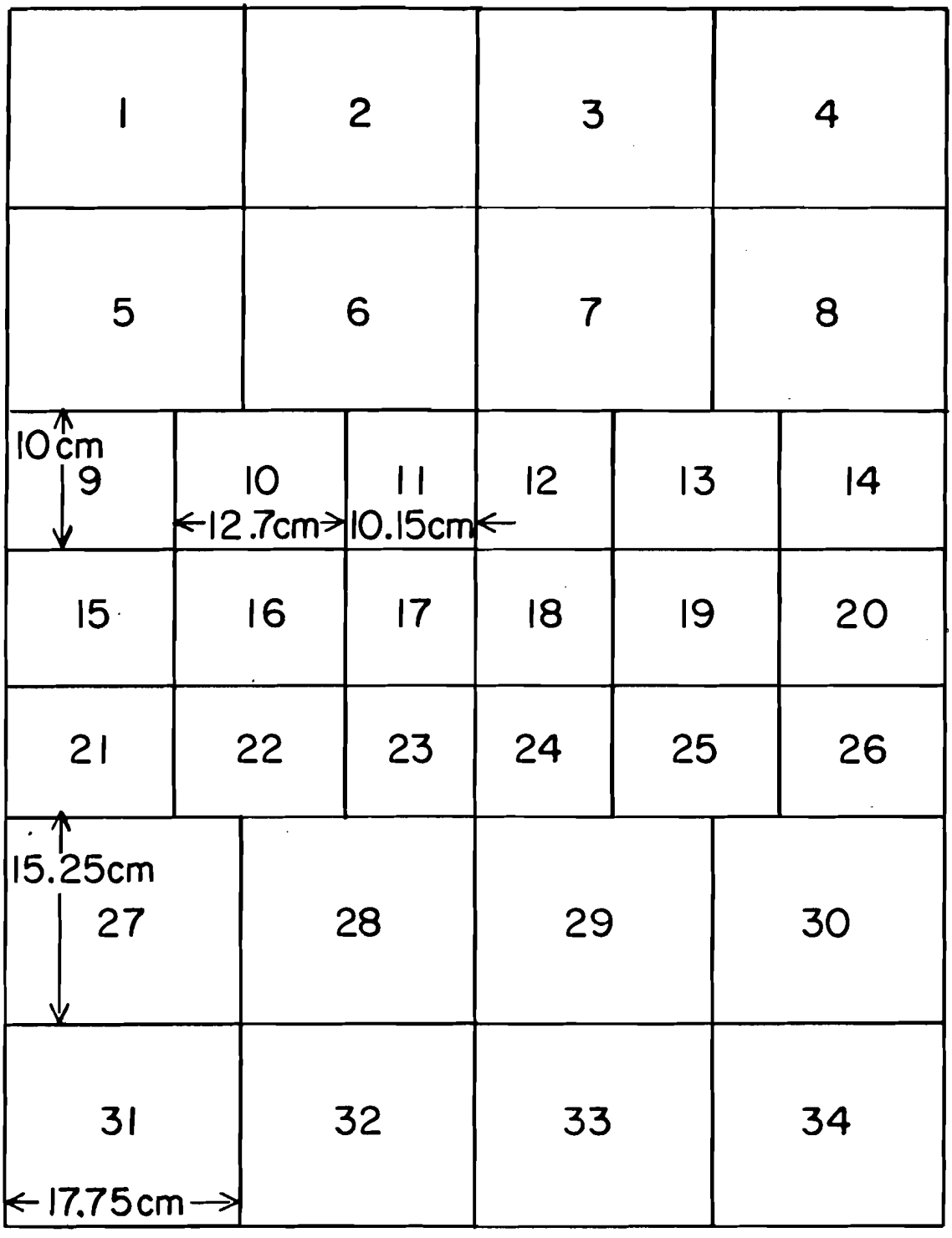

Figure 2.9 C0 mirror plane (XY projection, beam's eye view).

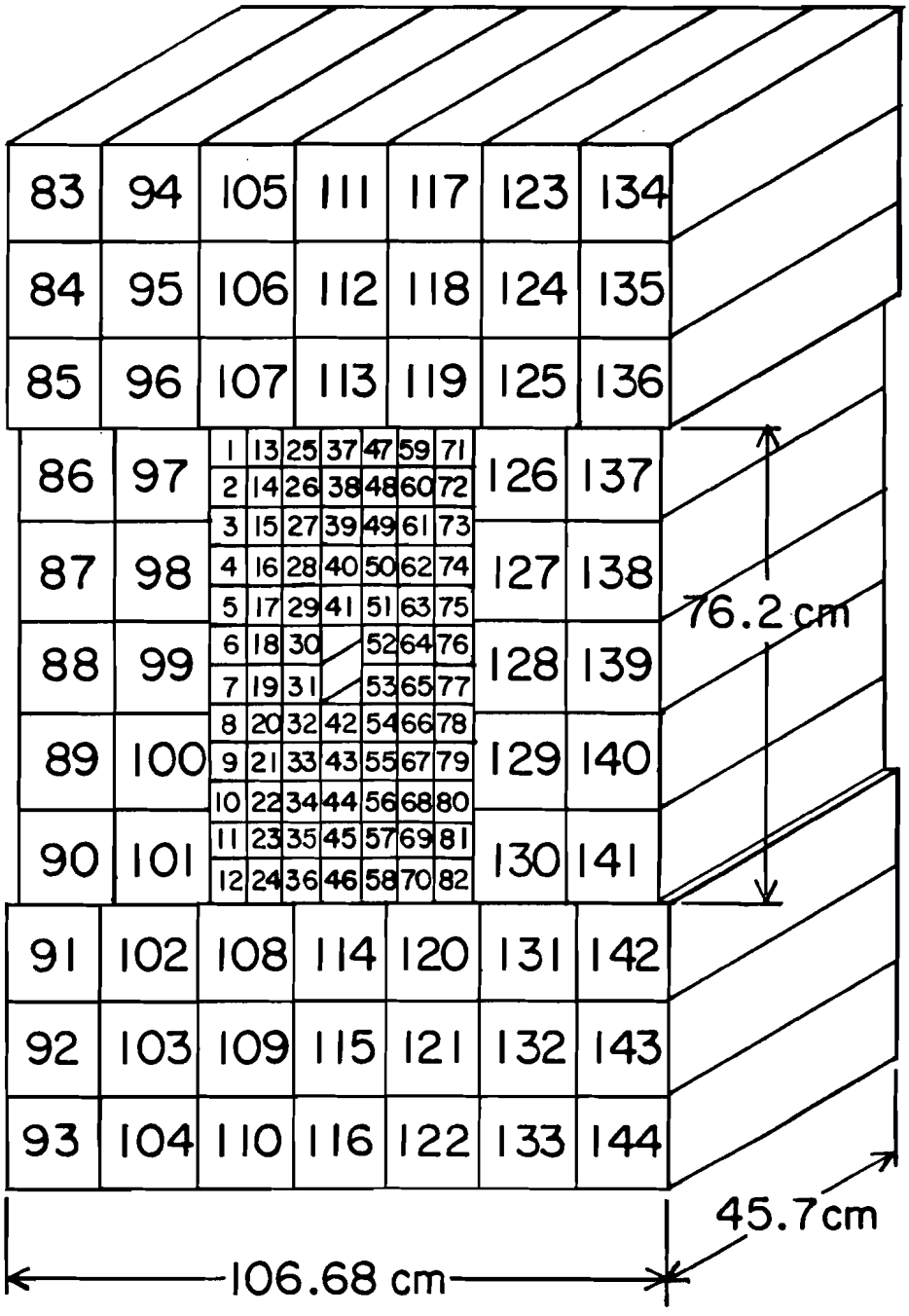

Figure 2.10 Lead glass array.

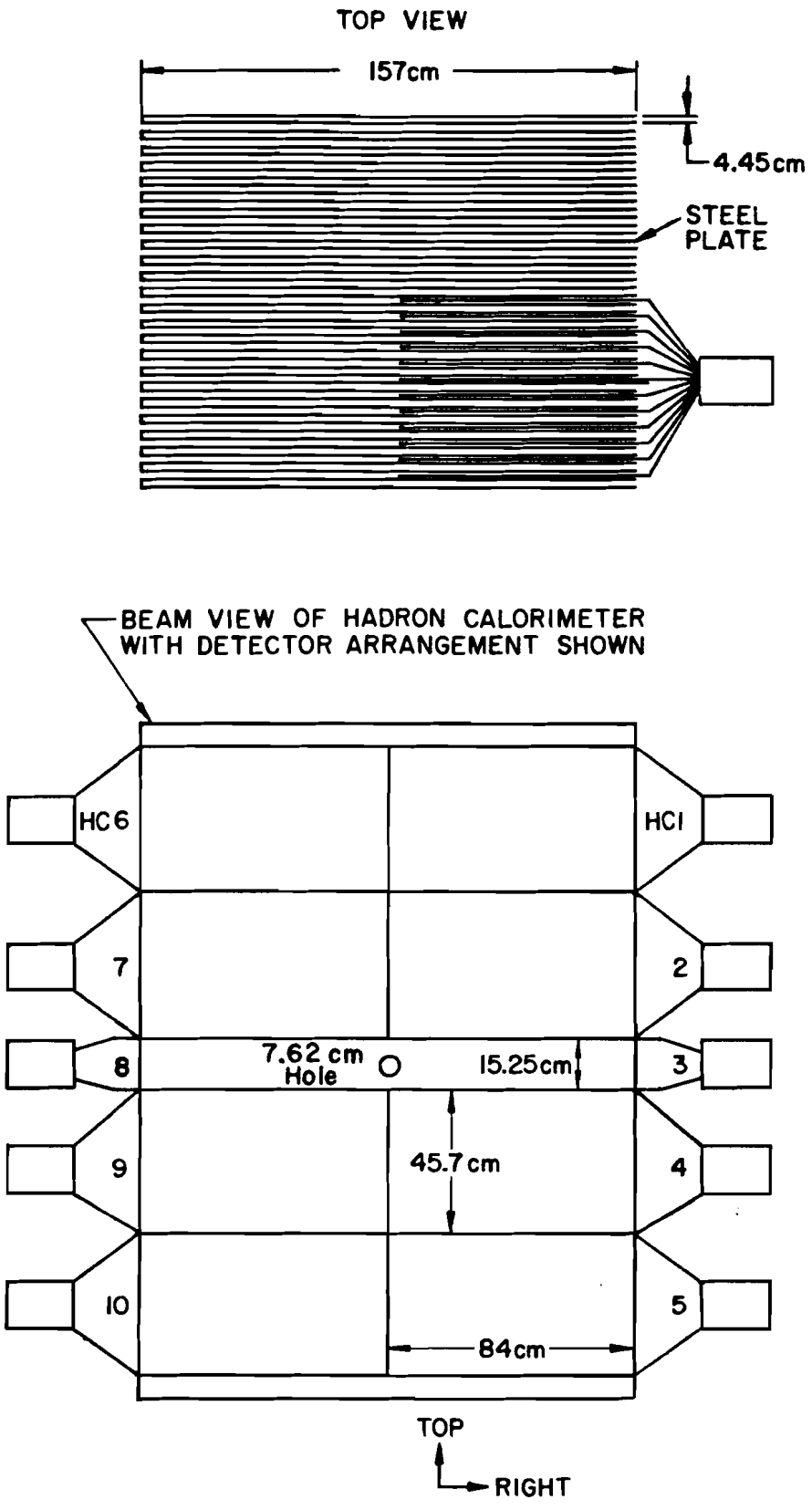

Figure 2.11 Hadron calorimeter.

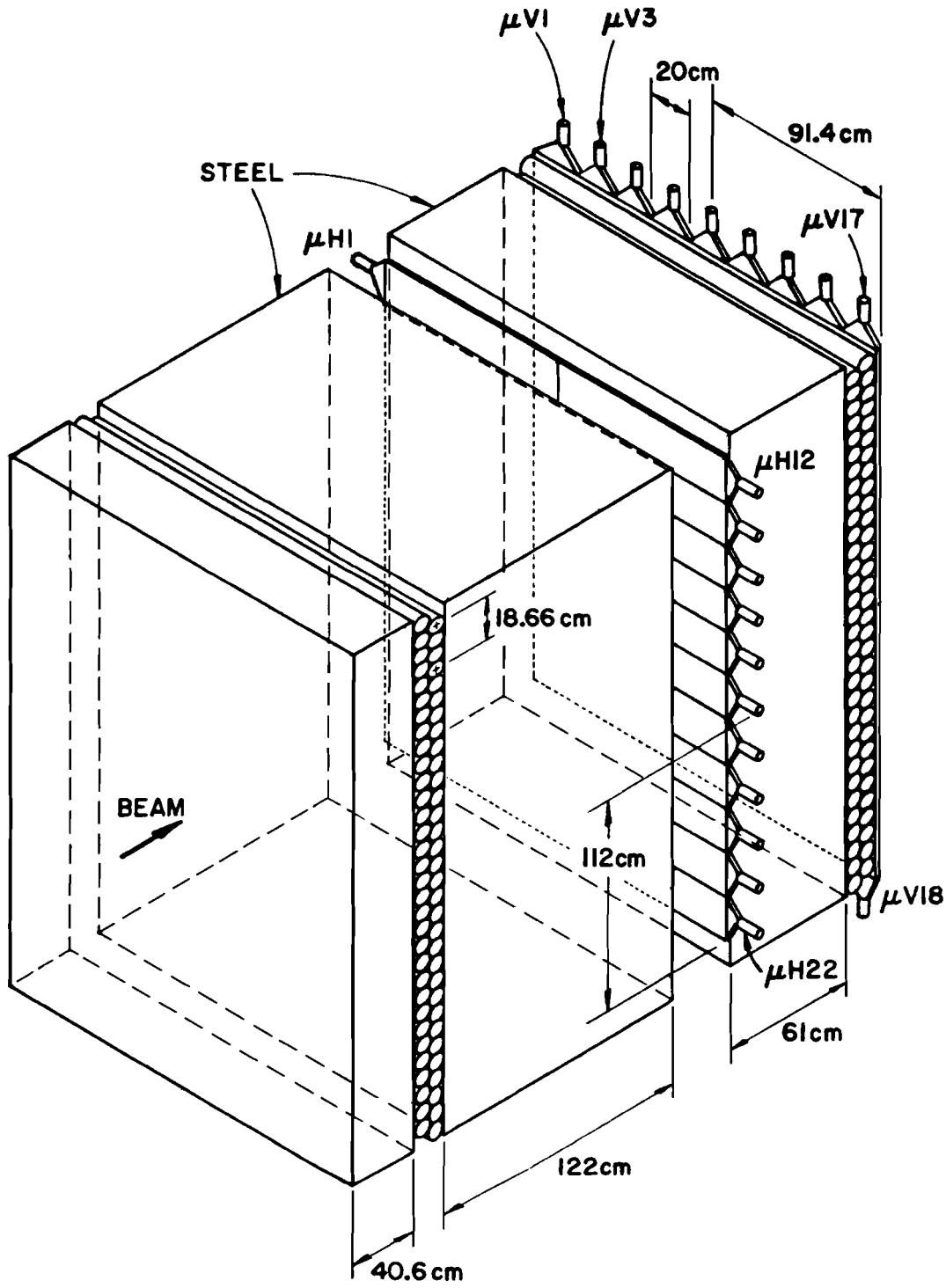

Figure 2.12 Muon identification system.
(Drift tube length is exaggerated - actual length is 152 cm)

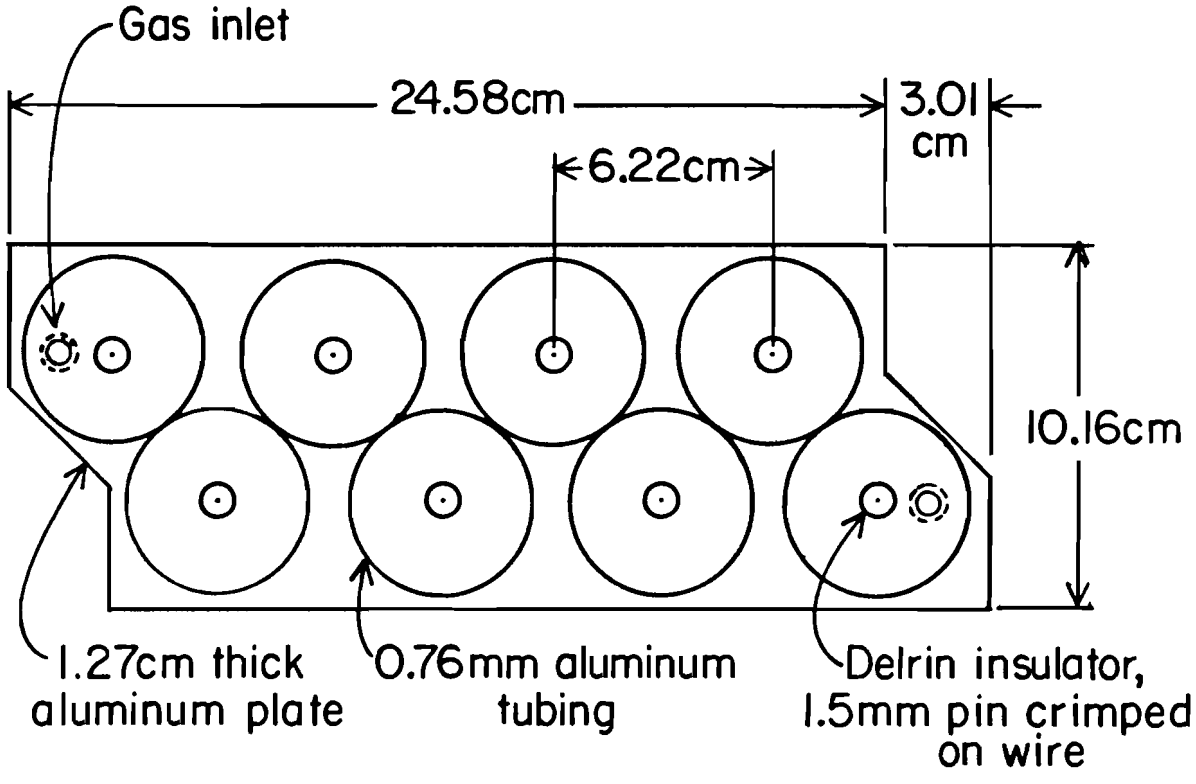

MUON TUBE ASSEMBLY

Figure 2.13

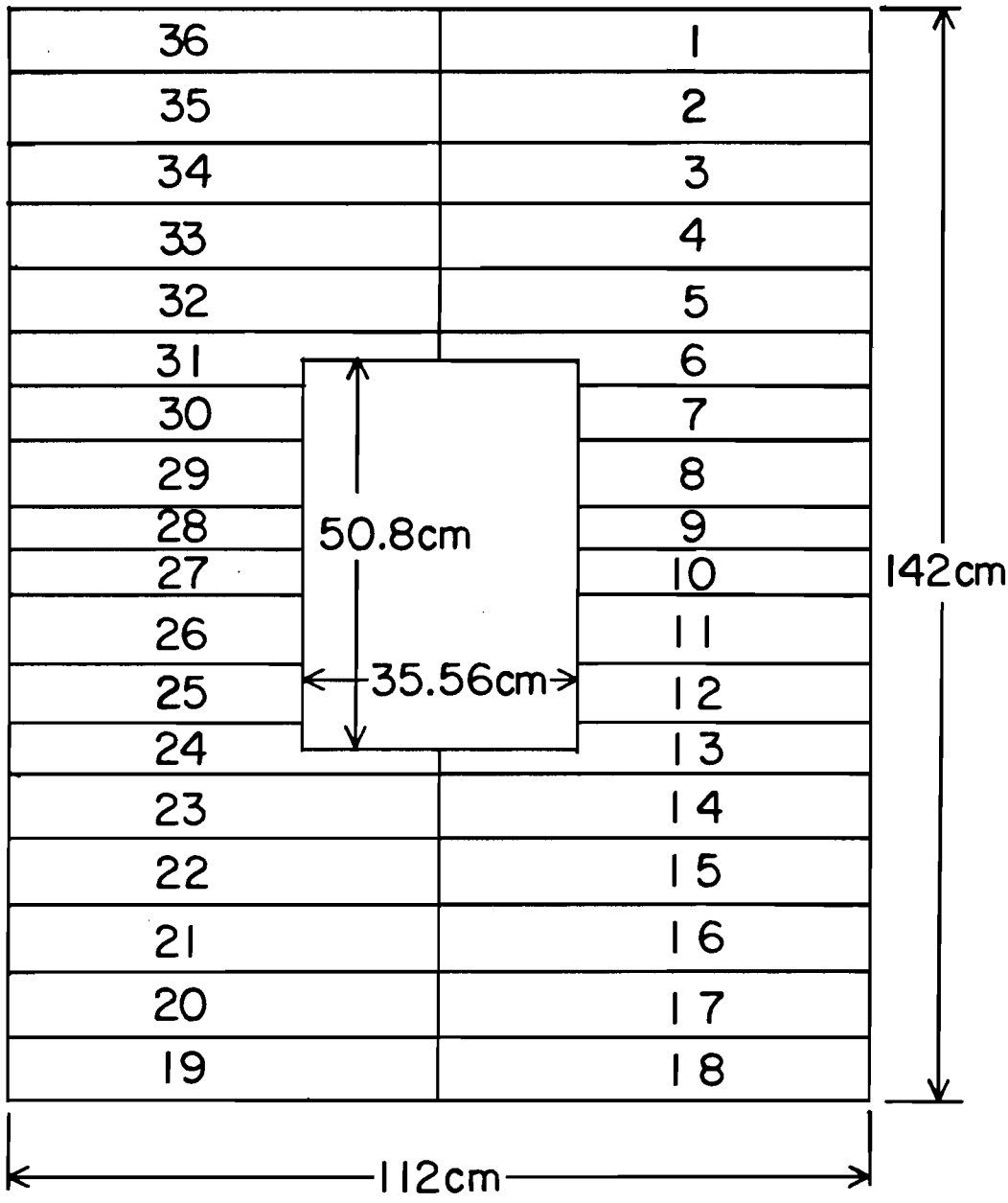

Figure 2.14 The outer electron counter.
(XY plane, beam's eye view)

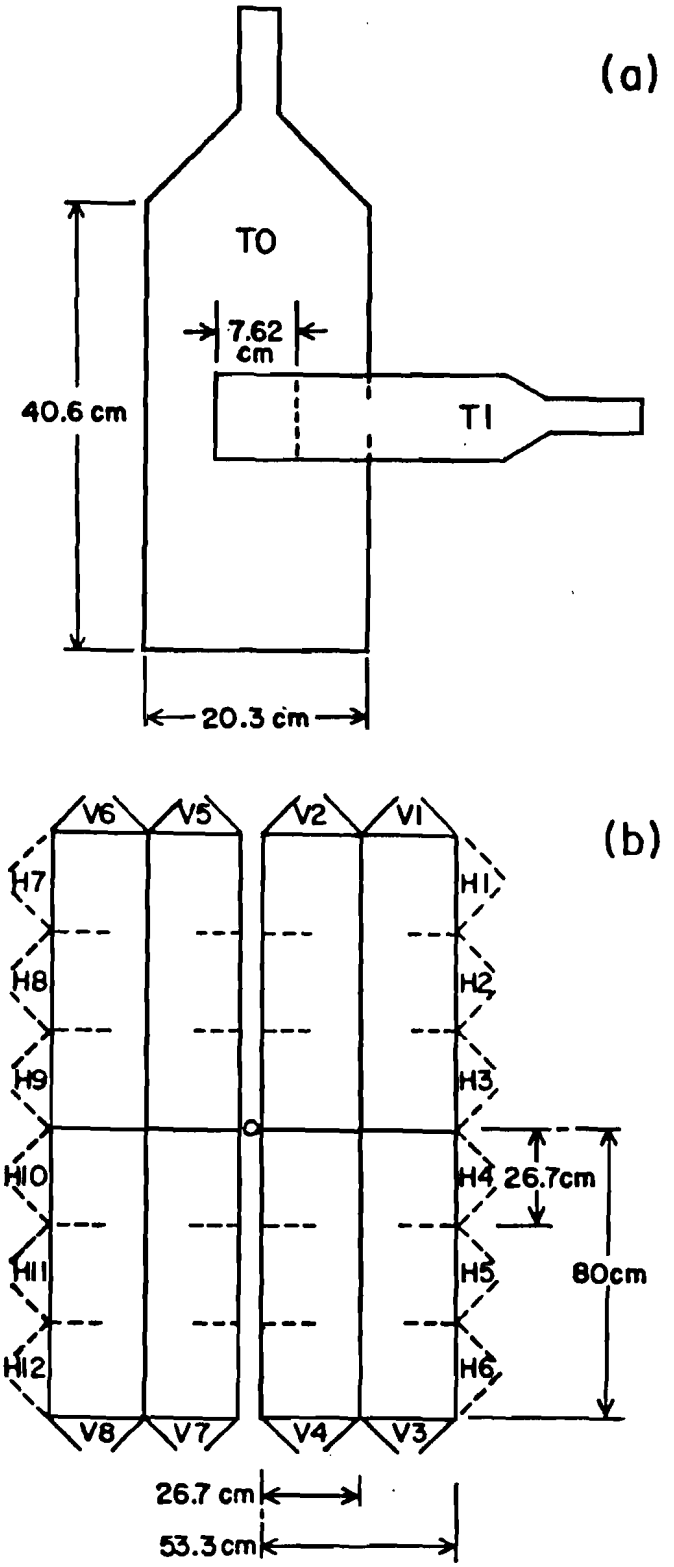

Figure 2.15 (a) T scintillation counters.
(b) H x V scintillation counters.

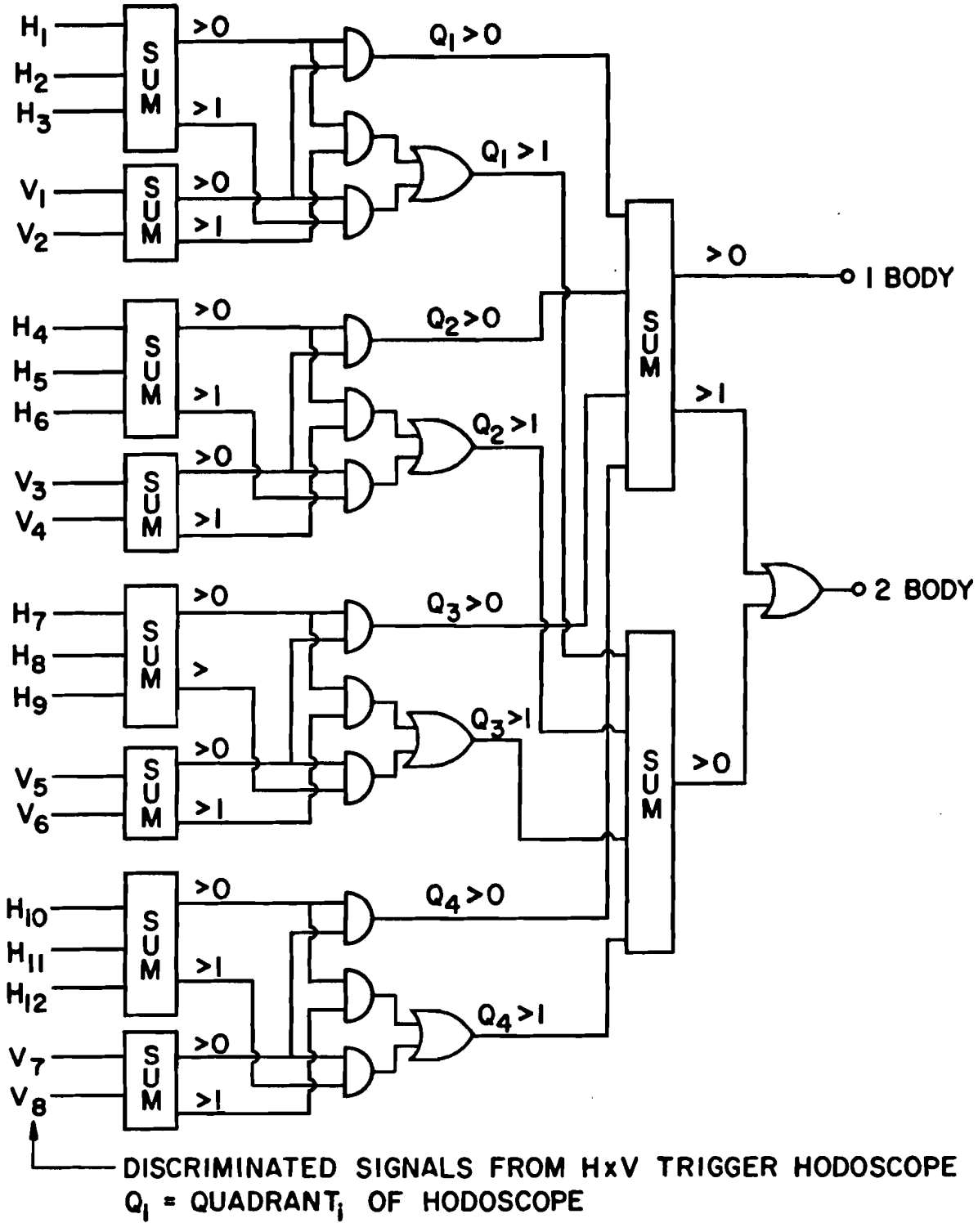

Figure 2.16 Schematic of H x V logic.

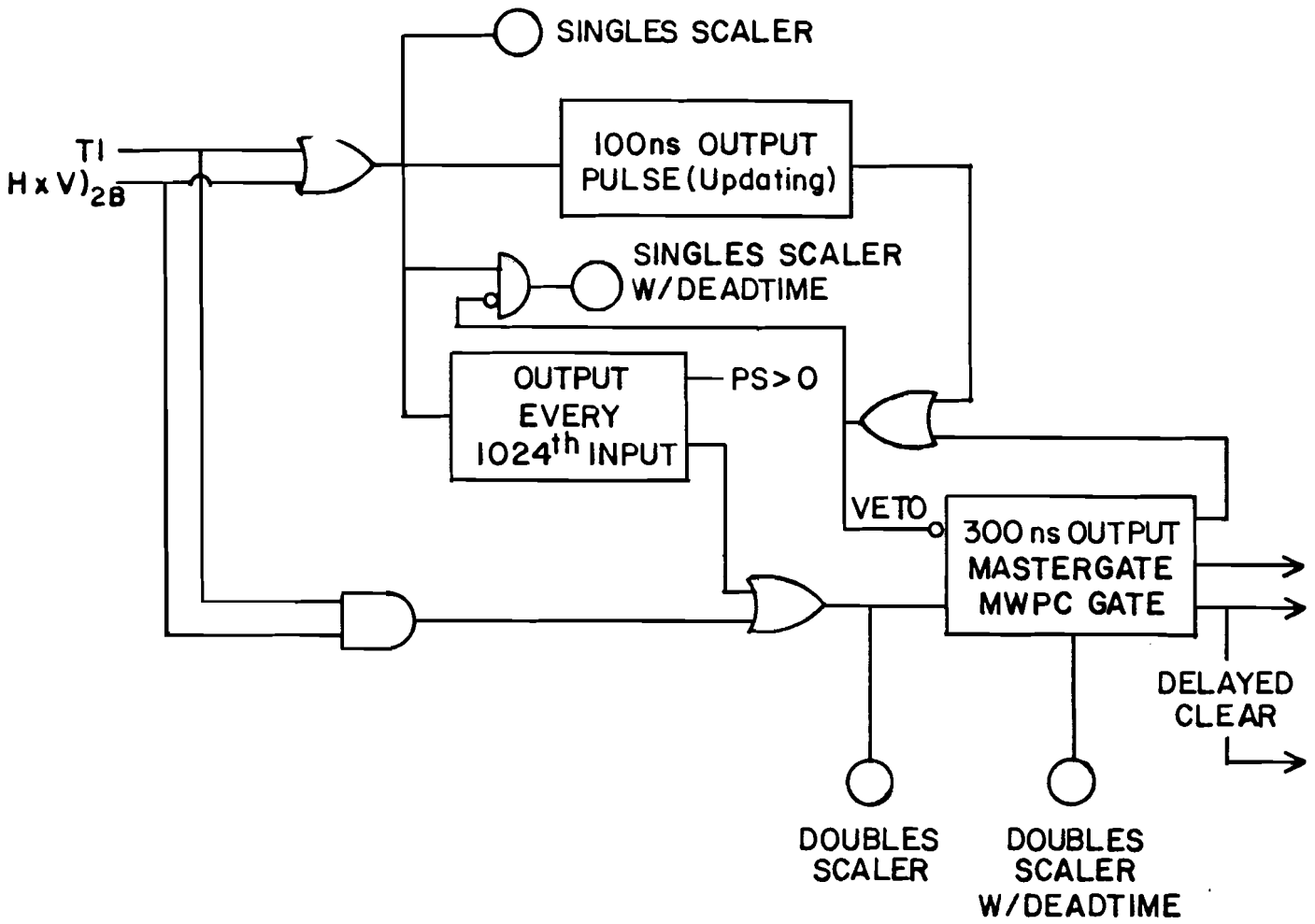

CONFUSION LOGIC SCHEMATIC

Figure 2.17

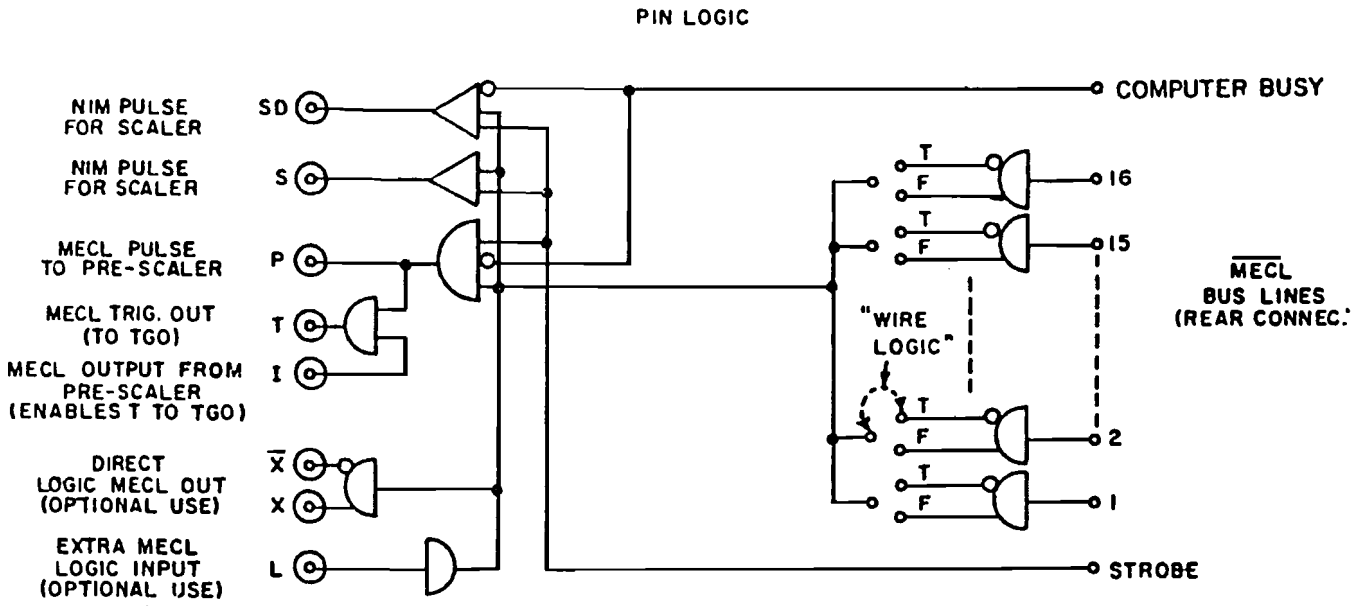

Schematic logic diagram of Pin Logic Module

Figure 2.18

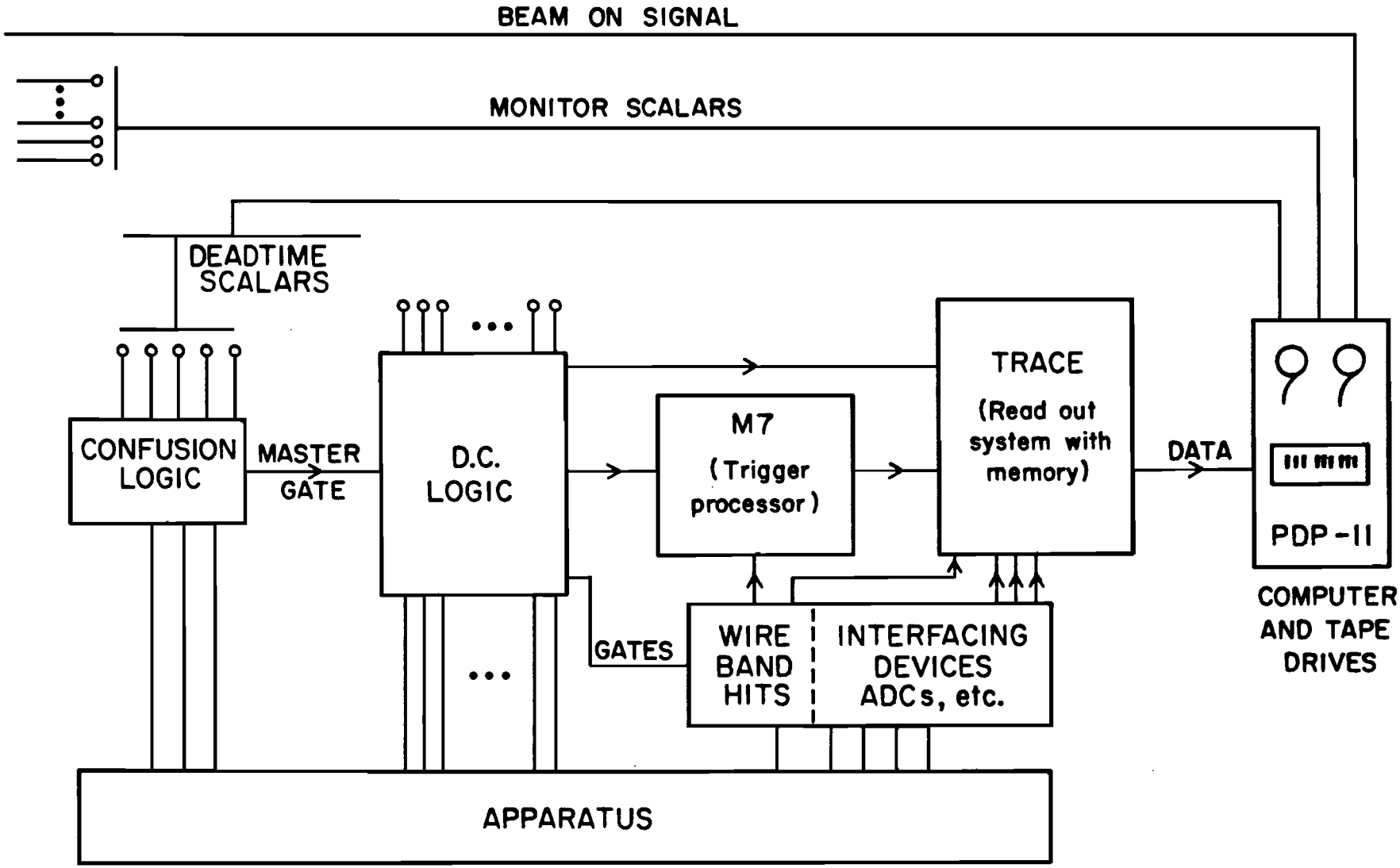

Figure 2.19 The data acquisition system.

CHAPTER 3

Data Analysis

3.1 Introduction

Data collected from FNAL Experiment 400 were recorded on 6250 BPI tapes. During the running period of 1984 (between February and June), the accelerator duty cycle time gave roughly ten seconds of beam every spill ($\sim$ 60 seconds). At this time, Experiment 400 was recording 4000 events per spill with a primary proton beam energy of 800 GeV. Each event had a length of about 900 words, and one tape was filled in 12 spills. Two tapes drives were provided so that data collection could be done without missing a spill, and with uninterrupted beam, a single 8 hour shift could require 26 or so tape mounts. The number of raw data tapes mounted for use at this beam energy was 1200, giving a total of nearly 60 million recorded events.

The raw data consist primarily of numbers that are associated with wire hits and ADC counts. The process of obtaining invariant mass plots of final charmed states from such raw information does not occur overnight. The final charmed state presented in this thesis was made possible only after the data had been carefully processed through several phases. Each phase of the data tape processing was done on the CYBER machines (three 175's and one 875) at FNAL. The data processing phases can be characterized as follows:

1. Track Reconstruction (Pass 1) - Pattern recognition and finding charged particle trajectories.
2. Pass 2 - Particle ID, momentum analysis, and calorimetry.
3. Event Skims - Selection of events to reduce the processing load and enhance the physics.
4. Pass 3 - Implementing the Vertex Chamber and TRM's to improve momentum and position resolution.

3.2 Track Reconstruction

The reconstruction program processed raw data wire hits into charged particle trajectories and also removed from the data blocks any ADC count that registered a value below threshold. During the experimental running period, raw data tapes were processed through the reconstruction phase on a daily basis so that faulty counters and "dead" wires could be detected and repaired while still collecting data. Nearly identical programs have been used successfully in the past by experimental groups operating with a similar multiwire chamber system[26]. Modification to the program for this experiment included expanding the arrays to allow for larger track multiplicities (up to 20). Also the number of unused hits (i.e., wire hits not assigned to any charged particle trajectory) was allowed to increase.

Input for the reconstruction program included the surveyed 15 wire plane Z locations, wire spacings, and central wire numbers. The program implemented an iterative fitting routine which removed, replaced and added wire hits associated with each track in an attempt to minimize the χ^2 per degree of freedom. The charged particle trajectories found by the program can be classified as follows: full tracks, stubs and V^0 tracks.

Full tracks (also called inner tracks) are trajectories that bend through magnet M2 and pass through chamber P3 and most likely chamber P4. Pattern recognition of these full tracks begins by forming a straight line through the X projection (the non-bend coordinate). These X projections are then matched with U and V projections formed from two lines that intersect in the bend plane (giving a "kink") in the center of M2. A crude estimate of the magnitude of the track's momentum can then be determined by dividing the magnet's effective "kick" by the bend (or "kink") angle. The angular acceptance of full tracks was $\pm$ 40 mrad in X and $\pm$ 50 mrad in Y.

Stubs (or outer tracks) are trajectories that do not pass through M2, but do pass through 9 planes of wires. They are assigned a zero M2 bend angle, and no momentum is assigned to them during this phase of processing. The angular acceptance of stubs was ± 100 mrad in X and ± 200 mrad in Y.

Trajectories which originate downstream of P0 define the the third classification of tracks. These tracks, called V^0 tracks, are indicative of long-lived neutral particle decays. The program accepts as input only the unused wire hits after all the tracks and stubs have been found. These V^0 tracks must exist in pairs and are constrained to come from a common vertex. At least one of the V^0 tracks must pass through M2 giving momentum information.

3.3 Pass 2

The next phase of processing (called Pass 2) accomplished the following tasks in this order:

1. Refitted the tracks from Pass 1.
2. Determined the primary vertex for each event.
3. Assigned momenta to the stubs.
4. Isolated V^0 tracks (upstream as well as downstream of P0).
5. Extracted particle identification information from the Čerenkov counters and the muon counters.
6. Summed the energy deposited into the hadron calorimeter, the lead glass and the beam dump calorimeter.

In the subsections below, details about some of these Pass 2 tasks are given, and information on detector performance is also mentioned.

Momentum and Vertex Determination

The tracks from the reconstruction program were refitted using additional input that was obtained from MWPC alignment studies and magnetic field mappings. The

MWPC alignment was performed using muon data where single track muon events were recorded (with and without the magnets on). The geometric settings of the chambers were mildly adjusted in a manner that minimized the muon track residuals (i.e., the difference between the reconstructed wire hits and the refit predicted wire hits for an assumed chamber geometry). Magnetic field maps were obtained for both M1 and M2. A great deal of effort went into understanding the details of the field. Modifications to the track fitting routines included fringe field effects at chambers P0 and P3, magnet rotation angles, weak focusing effects, bend center corrections, and helical path corrections. Checks on some of these modifications were made through a study of K_s^0 decaying in the M1 region. The efficiency in linking main spectrometer tracks with the vertex chamber depended critically on the precise form of the fields.

The primary vertex for an event was determined from extrapolating full 5 chamber tracks back to the target region using both the bend and non-bend projections. Stubs were also extrapolated back to the target region using only the non-bend projection. Stubs which had non-bend projections intersecting at the primary event vertex had their momenta determined from the bend angles found by tracing their trajectories back through M1. Primary vertex component distributions for typical Pass 2 events are shown in Fig. 3.1(a) and Fig 3.2 (a);(b). Notice that at this level of data processing, the different elements of the target are not resolvable.

V^0 Identification

The reconstruction program identified V^0's which originated downstream of P0, but a great many decays of K^0's and Λ's had occurred upstream of P0. The Pass 2 program attempts to isolate these tracks, remove them from the determination of the primary vertex, and assign them to a V^0 when appropriate to do so.

The track's distance of closest approach (DCA) to the primary vertex is cal-

culated. If a full track's DCA is less than 0.1 inches, then the track is said to be "attached" to the primary vertex. If a stub's DCA is less than 0.08 inches (using only the non-bend component), then the stub is attached to the primary vertex.

Pairs of oppositely signed tracks which meet (using the non-bend intersection) at least 3 inches downstream from the primary vertex are identified. These pairs are flagged as V^0 tracks only after passing certain conditions. The first condition requires that both tracks in the pair are not attached to the primary vertex. This is done primarily to avoid the large level of background obtained from considering doubly-attached pairs. A second condition requires that one track in the pair must be a full track to give momentum information. Finally, both tracks from a given pair must not be associated with other pairs. This leads to a complicated arbitration scheme which selects those pairs which appear to be associated with real neutral particle decays.

The pairs under consideration in this arbitration scheme are classified as a track-track pairs or track-stub pairs, and then they are further classified as singly-attached or unattached (to the primary vertex). The arbitration scheme first considers only track-track pairs, arbitrating in those pairs which have significantly smaller DCA_Z or significantly better $P_\perp$ balance. Here, DCA_Z refers to the separation distance between the 2 tracks at the Z of the decay, and $P_\perp$ balance refers to how well the V^0 momentum (as computed from the charged track pair) extrapolates back to the primary vertex. If this arbitration fails to make a decision, then unattached pairs are selected over singly-attached. Finally, if this test fails, then the track-track pair with the best DCA_Z is kept.

Then, arbitration involving only track-stub pairs is done. The selection favors pairs which "originate" significantly further downstream or pairs with significantly better $P_\perp$ balance. If these test fail to select a pair, then unattached is favored over

singly-attached. The final step selects the pair that originates furthest downstream. Arbitration between a track-track pair and a track-stub pair is done in an manner identical to track-stub only arbitration except the final step of arbitration keeps the pair giving the best $P_\perp$ balance.

Distributions of the invariant masses ($\pi\pi$ and $p\pi$) for those pairs which survived the arbitration and for those which failed are shown in Figures 3.3 and 3.4. Arbitration efficiencies are about 85%. Losses primarily occur in the singly-attached category where large background levels exist.

Searches for "unconventional" V^0's included efforts to identify reconstruction V^0's from unused wire hits allowing for a missing hit in any one wire chamber (acting on the belief that chamber inefficiencies may have accounted for a missing hit). Also, stub-stub V^0's and V^0's which open up in M2 (called P34 V^0's since only chambers P3 and P4 could have given hits for these tracks) were isolated with the help of a constrained vertex fitter which demanded $P_\perp$ balance.

Reconstruction of the Event Energy

After appropriately calibrating the calorimetry devices, the total event energy was approximated by the following expression:

$$E_{TOT} = 1.05 * E_{HAD} + E_{LG} + E_{BD} + 1.5 * E_{STUB} + 10. \text{ (in GeV)}$$

where E_{HAD}, E_{LG}, and E_{BD} represent the energy collected in the hadron calorimeter, the lead glass, and the beam dump calorimeter, respectively. The total energy from charged tracks which do not pass through the M2 and have momentum less than 25 GeV is labeled E_{STUB}.

Energy from gamma rays which do not reach M2 is taken into account by adding in $1.5 * E_{STUB}$. It is assumed that there is one-half as many neutral pions as there is charged pions. Also neutral pions and charged pions are assumed to have correlated

positions and energies. Note, however, that only about 10% of the total event energy enters the stub region.

Hadronic energy deposited in the lead glass is not properly measured by Čerenkov radiation. The additional factor of 1.05 multiplying the hadron calorimeter energy is to take into account the hadronic energy deposited into the lead glass but not collected there.

The final term of 10 GeV represents the typical energy lost due to particles not passing through M1. A distribution of the total reconstructed event energy from the data is shown in Figure 3.5. During a special test run, the beam was allowed to directly interact in the beam dump calorimeter, and a QVT distribution was obtained from the sum of the ADC outputs of the BDC. The spectrum of the reconstructed total event energy is in close agreement with the spectrum obtained from the QVT.

Čerenkov Analysis

Once the Pass 2 program determines a particular charged particle's trajectory and momentum, the next step is to identify that particle's mass. The analysis of particle identification involves three Čerenkov counter and two banks of muon drift tubes (with accompanying scintillation counters). Muon identification is not used in the results of this dissertation and will not be described here, but the success of the Čerenkov identification is essential for the results which follow.

Two separate (but not completely independent) Čerenkov algorithms are implemented. Both algorithms use the same detector performance assumptions, i.e., estimates of the predicted amount of light received by a particular Čerenkov cell from a given track with an assumed identity are the same. But the algorithms differ in the methods used to assign particle identification. One algorithm, called LOGIC, uses a quick, time-saving approach that is similar to past successful methods[26]. The

other algorithm, called CERAL, used a slower, more elaborate approach to determine particle identification.

First, LOGIC determines if the cells in a given Čerenkov counter are "on" or "off". Cells with corresponding ADC's reading out 10 or more counts above pedestal are "on", otherwise they are "off". The 10 count demand suppresses noise at a small loss to efficiencies since a single photoelectron registers about 120 counts above pedestal. Next the amount of predicted light in each cell is determined by assuming all tracks are pions. For a given track, the relevant cells being examined include the cell struck by the track and the adjacent cells. If any of these cells are "on" and 0.2 photoelectrons are expected (under the pion hypothesis) in that cell from the given track, then that track is flagged as "on". When a track can not be flagged as "on", the algorithm checks to see if the track can be positively identified as "off". If the total expected photoelectron count is greater than 2.5 after summing over all the relevant "off" cells, then the track is flagged as "off". If the track is not flagged as "on" or "off", then it is flagged as "confused". The track's on-off code for a given Čerenkov counter is then compared with the track's momentum (and the counter's threshold values) to set a 4-bit status word that gives the particle identification as follows:

No bits "on": Indeterminate.
Bit 1 is "on": Consistent with being an electron.
Bit 2 is "on": Consistent with being a pion.
Bit 3 is "on": Consistent with being a kaon.
Bit 4 is "on": Consistent with being a proton.

Values of the 4-bit status words for each Čerenkov counter and the corresponding track momentum regions are listed in Table 3.1. The final particle identifications were obtained by taking the "and" of the three status words associated with each track

(giving a final status word called ISTATL). So, for example, consider a track that has momentum between 22.4 GeV and 41.4 GeV. If C0 flags the track as "confused" (all bits "on"), C2 flags the track as kaon-proton ambiguous (having bits 3 and 4 set "on"), and C3 flags the track as electron-pion-kaon ambiguous, then the tracks final particle identification is a definite kaon (bit 3 "on" only; ISTATL = 4). When the final status word had all bits "off" (ISTATL = 0), then inconsistent information was obtained from one or more of the counters. And when the final status word had all bits "on" (ISTATL = 15) the particle identification was "confused" as a result of the track having missed the mirrors, track clustering, or the track having an unfortunate momentum value. About 80% of the tracks are identified as consistent with being a pion. The momentum regions for identifying heavy particles (which have mass exceeding the pion) are as follows:

Definite kaons are found between 10.6 Gev and 41.4 GeV.
Definite protons are found between 10.6 GeV and 78.8 GeV.
Ambiguous kaon-proton tracks are found between 3.0 GeV and 41.4 GeV.

CERAL uses status words which had the same meaning as those used by LOGIC but determines the predicted light from a given track by considering all possible track identities (electrons, pions, kaons, and protons). These photoelectron predictions are then compared to the observed number of photoelectrons from every cell (which are calculated from the raw pulse height distributions). Tracks are studied in isolated clusters (usually less than 4 tracks to a cluster), and CERAL loops over every track considering every possible identity. If the light information from a cell does not match with a possible track identity combination, then that possibility is rejected. The final status word from CERAL (called ISTATP) was set by "anding" the status words found from all three counters (just as done in LOGIC).

The overall effectiveness of these Čerenkov algorithms was studied by examining pure samples of K_s's and Λ's. This study was also used to make comparisons on the two algorithms. Pure samples were obtained by first eliminating V^0's with $0.46 \leq M_{\pi\pi} \leq 0.53$ GeV from the Λ sample and V^0's with $1.00 \leq M_{p\pi} \leq 1.23$ GeV from the K_s sample. To isolate the proton from the π in Λ decays, the proton was required to have 5 GeV more momentum than the π . A $P_\perp$ balance demand and a fixed secondary vertex was implemented in a constrained fit involving pairs of V^0 tracks. The final requirement that the χ^2 from this fit is small (less than 0.01) gives the $M_{p\pi}$ and $M_{\pi\pi}$ mass distributions for Λ's and K_s's as shown in Figure 3.6, where the solid vertical lines shown represent the V^0 mass cuts used to give pure samples of protons and pions. Protons entering the pure sample were required to have momenta in the range where unambiguous Čerenkov identification is possible (i.e., between 10 and 80 GeV). Particle identifications obtained from LOGIC and CERAL for these pure proton and pion samples are listed in Table 3.2. Čerenkov identification (CERAL or LOGIC) flags a proton as a non-proton less than 20% of the time, and flags a pion as a non-pion less than 10% of the time. Notice that there is considerable difference (nearly 50%) between the two algorithms when flagging these particles with a definite identity. LOGIC is better at flagging definite protons, and CERAL is better at flagging definite pions. Because of the large levels of background, achieving a pure sample of kaons from K^*'s or ϕ's , for example, is difficult to do without demanding Čerenkov identification. In any case, CERAL and LOGIC do differ in which tracks should be flagged as definite kaons at about the 50% level. Clearly there are significant differences in the particle identifications outputted from these two algorithms.

3.4 Event Selections

At this point events were "skimmed off" from Pass 2 tapes so that charmed particle searches (and other physics searches) could be done without implementing

information from the vertex chamber. The event skims were also motivated by an effort to save processing time at the Pass 3 level. The Pass 3 processing is considerably slower (per tape) than the other passes of the data. The 1200 Pass 2 tapes (6250 BPI) were reduced to about 350 tapes by selecting only those event which contained any of the following:

1. A clean K_s. (Demand that the invariant mass $M_{\pi\pi}$ falls within 30 MeV of 497.67 MeV for conventional V^0's; and within 40 MeV for other categories. Also for one attached V^0's demand additional clean-up criteria using a $P_\perp$ vertex constrained fit and a comparison of attachment distances at the primary and V^0 vertices.)
2. A clean Λ. (Demand the mass $M_{p\pi}$ falls within 20 MeV of 1115.6 MeV for conventional V^0's; and within 25 MeV for other categories. Also for one attached V^0's demand that the faster track be identified as a Čerenkov definite proton or an ambiguous kaon-proton.)
3. Phi Skim. (Demand two particles be Čerenkov identified as either definite kaons or kaon-proton ambiguous and that their invariant mass fall within 20 MeV of 1020 MeV. Require opposite signs on the particles.)
4. First D* candidate skim. (Demand the mass $M_{K\pi}$ is within 150 MeV of 1864.7 MeV and $M_{K\pi\pi} - M_{K\pi} < 165$ MeV. The kaon and the first pion must be oppositely charged. Also the kaon must be Čerenkov identified as a definite kaon or kaon-proton ambiguous.)
5. Second D* candidate skim. (Demand a clean K_s and require the $M_{K_s\pi\pi}$ mass to be within 150 MeV of 1864.7 Mev with the pions having opposite charges. Also demand $M_{K_s\pi\pi\pi} - M_{K_s\pi\pi} < 165$ MeV.)
6. D^+ candidate skim. (Demand a Čerenkov identified definite kaon and that $M_{K\pi\pi}$ is within 150 MeV of 1869.4 MeV. Also require that the pions have the same sign and that the event multiplicity is less than 12.)
7. First Λ_c candidate. (Demand that a definite proton, a definite kaon or kaon-proton ambiguous track, and a pion give an invariant mass $M_{pK\pi}$ within 150 MeV of 2282 MeV. Also require that the charges on the proton and pion are opposite the kaon charge, and that the event multiplicity is less than 12.)
8. Second Λ_c candidate. (Demand that a clean K_s and a track flagged as a definite proton or kaon-proton ambiguous give an invariant mass $M_{K_s\pi}$ that falls within 150 MeV of 2282 MeV.)
9. A "good" muon. (Demand that a single track fires 3 of the 4 muon planes and that the track has $p_\perp > 1.0$ GeV.)
10. A "kink". (A $\Sigma^\pm$ candidate).
11. Oppositely charged pair of definite kaons.
12. Kaon - proton pair. (Both tracks are identified as definites and must have the same charge.)

Note that for the charmed particle candidate skims, both particle and antiparticle combinations were selected. Also notice the broad kinematic mass selection cuts used for these charmed particle searches. Secondary skims were done off these event selection tapes to isolate a specific item of interest. For example, the results presented later in this dissertation are based on a secondary skim that selected only those events which passed item number 7 above. This secondary skim outputted 14 tapes from the available 350 event selection tapes.

3.5 Pass 3

The final phase of data processing (called Pass 3) improved the momentum and position resolution by implementing information from the vertex chamber and the TRM's. Wire hits assigned to the main spectrometer tracks were adjusted according to the drift distances obtained from the TRM's located in chambers P1 through P4. And then these tracks were linked through the vertex chamber and refitted with the resulting additional wire hits. Approximately 85% of the main spectrometer tracks which originated from the target region successfully linked through the vertex chamber.

In Pass 3, the track momentum resolution was improved by 25%. The momentum resolution achieved was about 2% for 100 GeV full tracks and 14% for 100 GeV stubs.

Position resolution was improved by about an order of magnitude, giving the transverse position resolution at nearly 70μm and the longitudinal position resolution at about 1300μm (as determined by the error on the primary vertex - see Appendix B). The effects of this improved position resolution can be seen from a comparison of the primary vertex Z component distributions found in Pass 2 (Fig. 3.1(a)) with those found in Pass 3 (Fig. 3.1(b)). At the Pass 3 level the four distinct target

regions are clearly resolved. A description of an analysis technique which utilizes this improved position resolution to identify charmed particle decays (by their short but finite lifetime) is described in Appendix A - The Correlated Impact Parameter Fit.

Table 3.1 Čerenkov identification status words.

C0

Track Momentum Region (GeV)	Cells Off	Cells On	Confused
0.0 - 3.0	1110	0001	1111
3.0 - 10.6	1100	0011	1111
10.6 - 20.3	1000	0111	1111
above 20.3	0000	1111	1111

C2

Track Momentum Region (GeV)	Cells Off	Cells On	Confused
0.0 - 11.7	1110	0001	1111
11.7 -41.4	1100	0011	1111
41.4 - 78.8	1000	0111	1111
above 78.8	0000	1111	1111

C3

Track Momentum Region (GeV)	Cells Off	Cells On	Confused
0.0 - 6.4	1110	0001	1111
6.4 - 22.4	1100	0011	1111
22.4 - 42.6	1000	0111	1111
above 42.6	0000	1111	1111

Table 3.2 Checks on Čerenkov algorithms.

COMPARISONS ON PROTONS FROM LAMBDAS		
Track's Status Word	LOGIC	CERAL
Inconsistent	10.4%	11.3%
Definite Kaon	6.3%	5.0%
Non - Proton	18.1%	13.6%
Definite Proton	33.7%	20.0%
P/K Ambiguous	21.4%	32.5%
Confusion	15.6%	19.8%

COMPARISONS ON PIONS FROM KSHORTS		
Track's Status Word	LOGIC	CERAL
Inconsistent	2.5%	8.2%
Definite Kaon	0.2%	0.6%
Definite Proton	0.8%	0.5%
P/K Ambiguous	3.3%	2.3%
Non - Pion	7.5%	5.6%
Definite Pion	12.5%	21.1%
Confusion	19.6%	19.9%

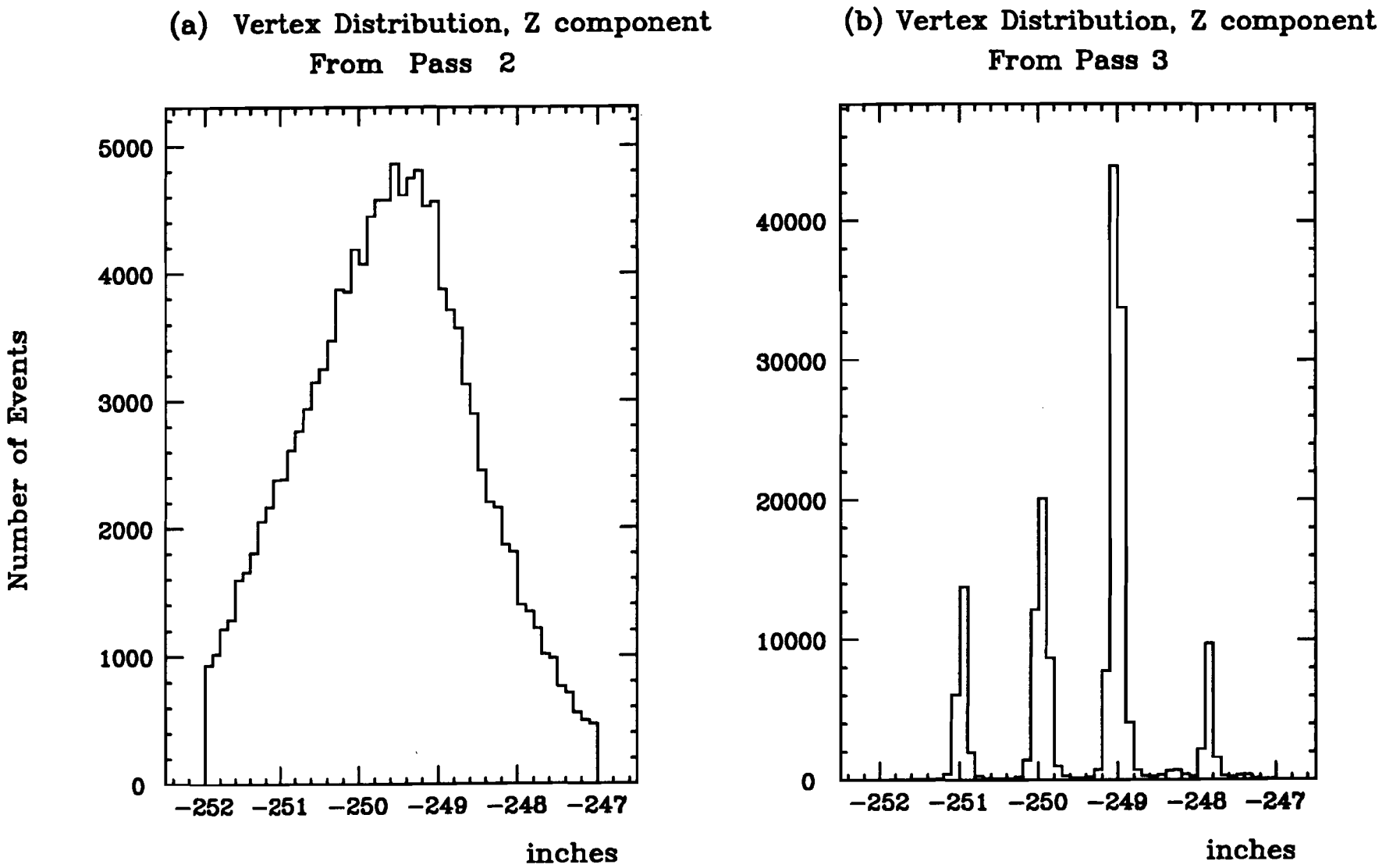
(a) Vertex Distribution, Z component
From Pass 2
(b) Vertex Distribution, Z component
From Pass 3
Number of Events
5000
4000
3000
2000
1000
0
40000
30000
20000
10000
0
−252 −251 −250 −249 −248 −247
inches
−252 −251 −250 −249 −248 −247
inches

Figure 3.1

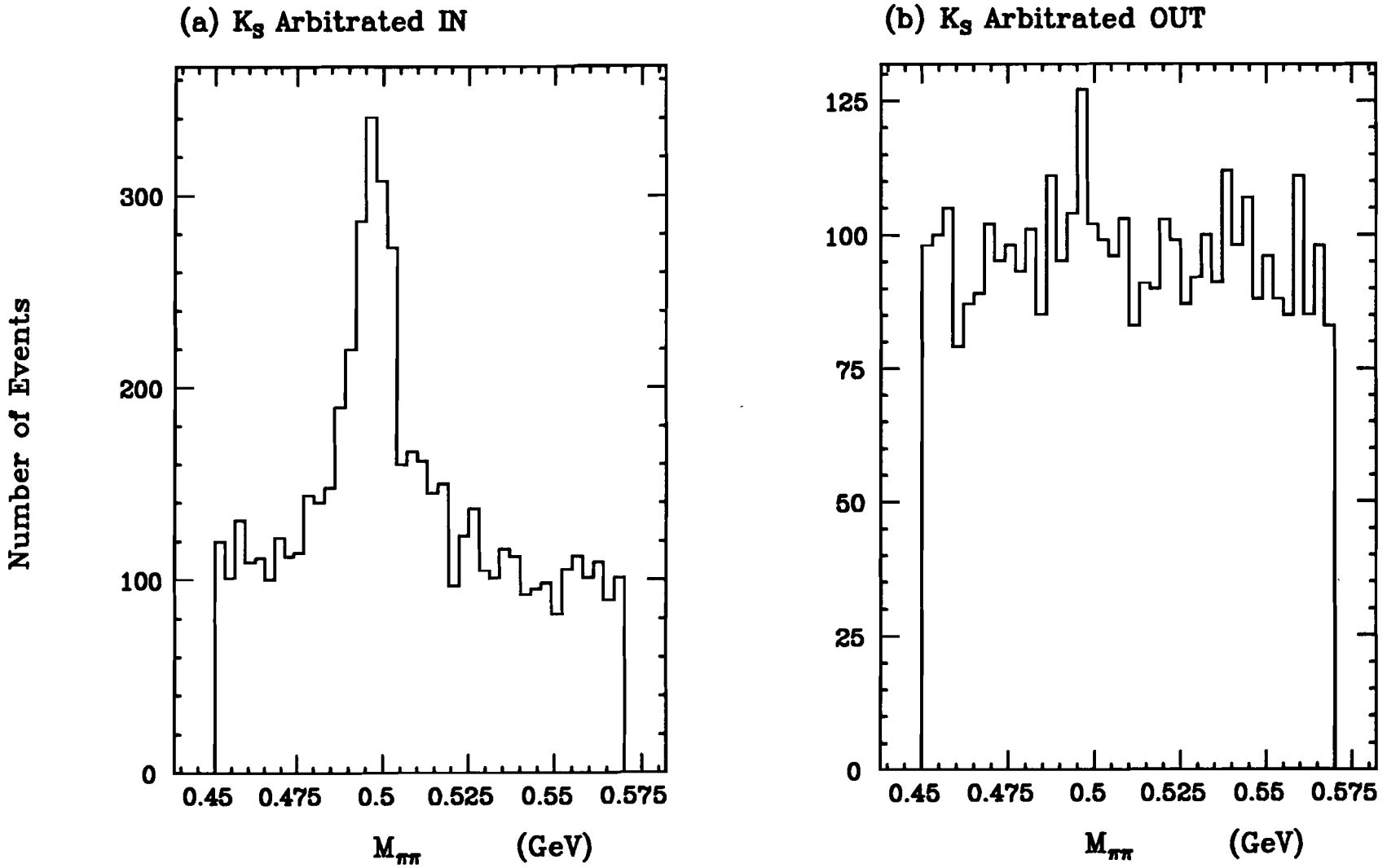
(a) K_S Arbitrated IN
(b) K_S Arbitrated OUT
Number of Events
0
100
200
300
0
25
50
75
100
125
0.45
0.475
0.5
0.525
0.55
0.575
$M_{\pi\pi}$ (GeV)

Figure 3.3

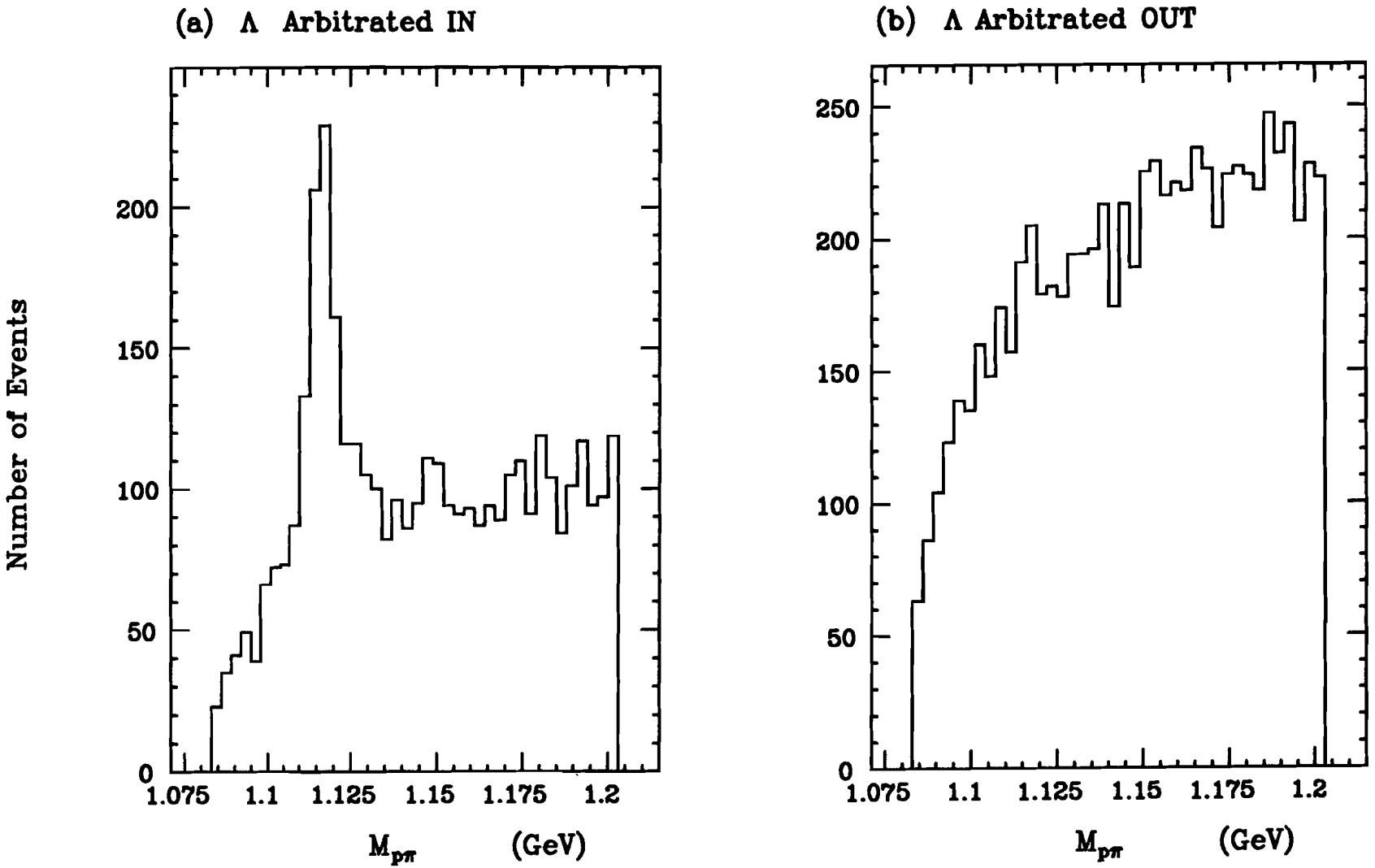
(a) Λ Arbitrated IN
(b) Λ Arbitrated OUT
Number of Events
0
50
100
150
200
250
1.075
1.1
1.125
1.15
1.175
1.2
$M_{p\pi}$ (GeV)

Figure 3.4

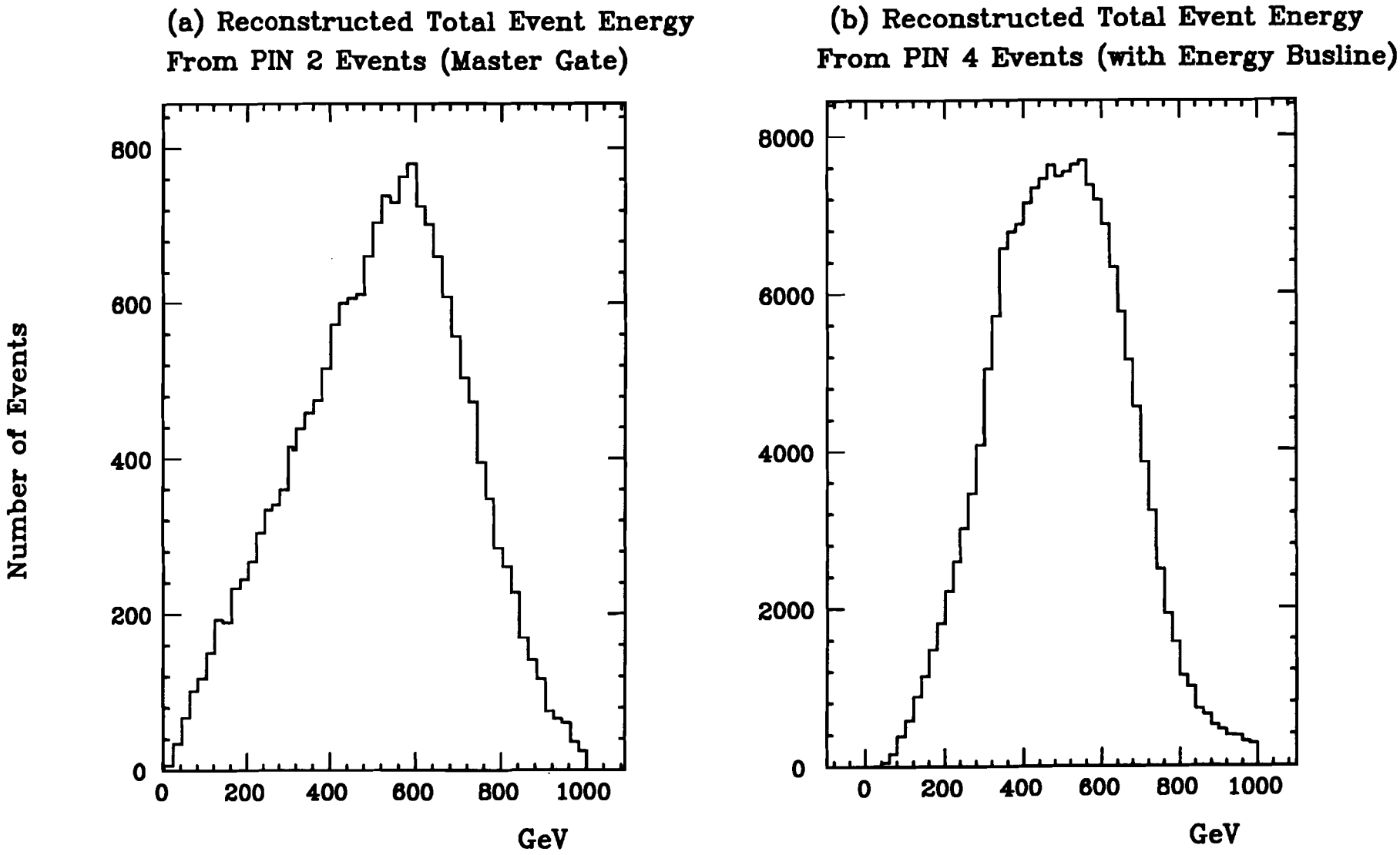
(a) Reconstructed Total Event Energy
From PIN 2 Events (Master Gate)
(b) Reconstructed Total Event Energy
From PIN 4 Events (with Energy Busline)
Number of Events
800
600
400
200
0
8000
6000
4000
2000
0
200
400
600
800
1000
GeV

Figure 3.5

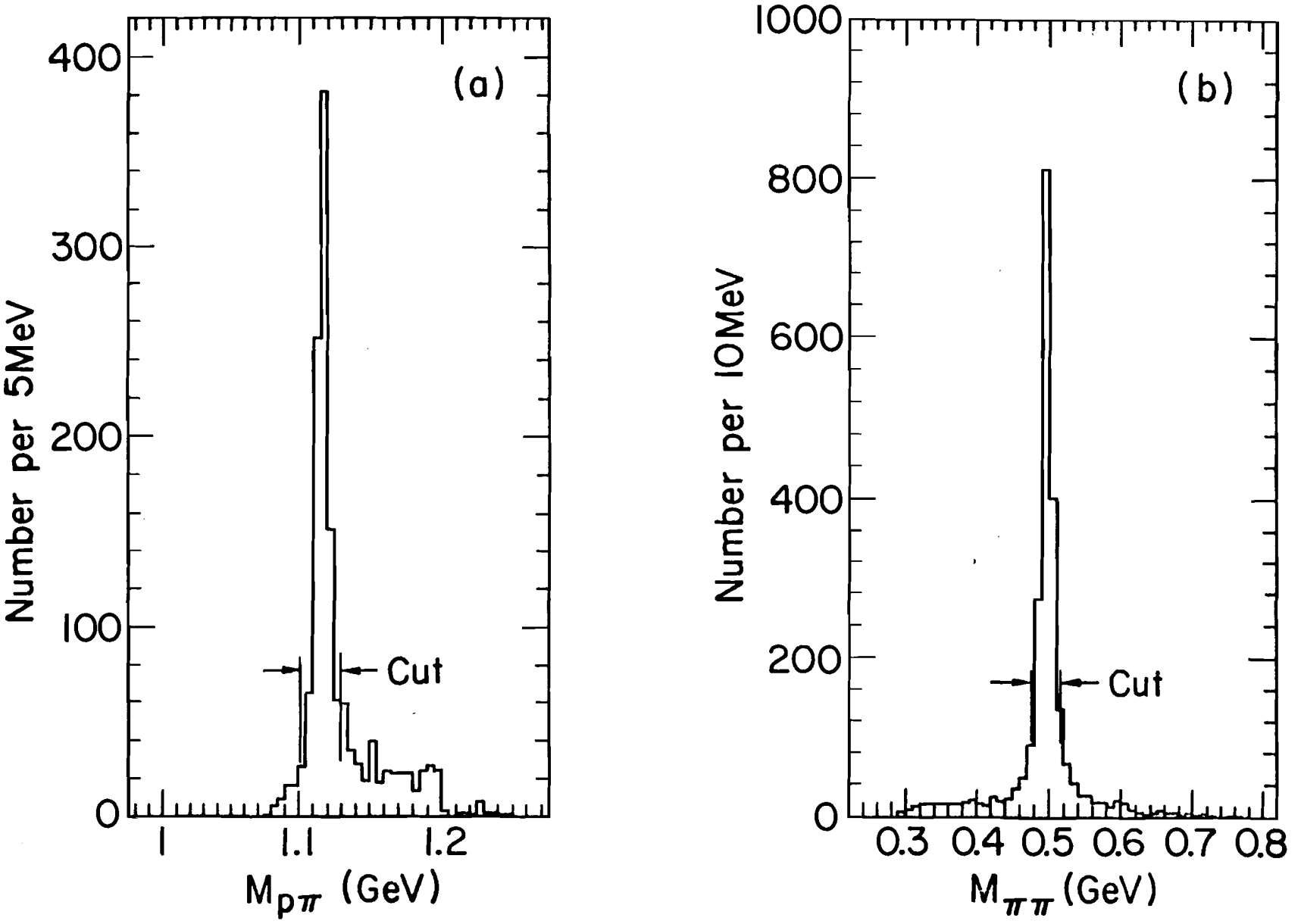
(a)
Number per 5MeV
400
300
200
100
0
Cut
1
1.1
1.2
$M_{p\pi}$ (GeV)
(b)
Number per 10MeV
1000
800
600
400
200
0
Cut
0.3
0.4
0.5
0.6
0.7
0.8
$M_{\pi\pi}$ (GeV)

Figure 3.6

CHAPTER 4

The Λ_c Signal

4.1 Introduction

Results on the inclusive production of Λ_c are presented in this chapter. The data examined below only include the portion of Experiment 400's running which accepted neutrons from collisions of 800 GeV protons on Beryllium. The search for $\Lambda_c^+ \rightarrow pK^-\pi^+$ (and $\Lambda_c^- \rightarrow \bar{p}K^+\pi^-$) was motivated by the following:

1. Of the observed specified decay modes for Λ_c , this one has the largest reported branching ratio[5] (2.2% $\pm$ 1.0%).
2. With two "heavy" particles in this decay mode, Čerenkov identification may be effectively used. Also the M7 trigger was designed to select events having one or more tracks indicating "heavy" particle Čerenkov identification. Note, a "heavy" particle is one that is more massive than the pion.
3. Lifetime analysis techniques may be used on this decay mode. Other modes, such $\Lambda_c^+ \rightarrow pK_s$ or $\Lambda_c^+ \rightarrow \Lambda\pi^+$, can not easily use lifetime techniques since neutral V^0's can not be detected in E400's vertex chamber.
4. Because of the relatively small phase space available for $\Lambda_c^+ \rightarrow pK^-\pi^+$, the momentum resolution of the particles from this 3-body decay is better than that from a 2-body decay.
5. Large cross sections for inclusive $\Lambda_c\bar{D}$ have been reported by four ISR experiments at center of mass energies near 60 GeV[12,14–18]. Specifically, mass peak signals for $\Lambda_c^+ \rightarrow pK^-\pi^+$ of over three standard deviations were seen. These Λ_c^+ 's were observed at high x_f, suggesting that charmed baryons from baryon beams may be produced abundantly in the forward direction. However, the exact interpretation of these results is somewhat controversial[12,19]. Perhaps the observation of this signal in E400 (although at a somewhat lower center of mass energy (ranging from 25 to 40 GeV)) may be helpful.

One disadvantage of this decay mode is the large combinatorics that exist due to the abundance of pions in a typical event. As discussed in Chapter 3, after the data were processed through momentum analysis and particle identification (Pass 2), events were selected from the data in an effort to isolate specific charm searches. The selection of $\Lambda_c^+ \rightarrow pK^-\pi^+$ and the antiparticle equivalent (event selection item # 7 in section 3.4) required that the events had to have multiplicities less than 12. This was done to

keep the combinatorics down and to make the final event sample a reasonable size. Other requirements on this event selection were that the proton had to be unambiguous identified by the Čerenkov system and that the pKπ invariant mass had to be within 150 MeV of the Λ_c mass (2.282 GeV). Finally, the charges on the proton and pion were required to be opposite the kaon charge. After this event selection was completed, the data were required to pass two more analysis "cuts". One of these "cuts" requires the kaon to be unambiguously identified by the Čerenkov system. The other "cut" takes only those pKπ combinations that have good quality tracks. The quality of a track is determined from a χ^2 (called χ^2_{wires}) that is generated from a fit (done at the Pass 2 level) which assigns main spectrometer wire hits to the track. Specifically, this track quality "cut" demands that the χ^2_{wires} for each track is less than 0.25 which is out on the tail of the distribution (see Fig. 4.1). To summarize, the analysis requirements (or "cuts") on the data described so far include the following:

Cut 1. Event multiplicities must be lower than 12.
Cut 2. The pKπ invariant mass must be within 150 MeV of the Λ_c mass (2.282 GeV).
Cut 3. The pKπ combination must have the appropriate charges.
Cut 4. The proton is unambiguously identified by the Čerenkov system.
Cut 5. The kaon is unambiguously identified by the Čerenkov system.
Cut 6. The tracks must have reasonable χ^2_{wires} (each less than 0.25).

Even with all of these demands on the pKπ combination, a large level of background exists in the signal region (see Fig. 4.2(a)). This indicates that some special analysis technique, such as the correlated impact parameter fit (see Appendix A), is needed to drastically improve the signal to background ratio. Indeed, one can pass this selection of events through the correlated impact parameter fit and find a drastic improvement in the ratio of signal to background by applying the following cuts to the pKπ combinations (see Fig. 4.2(b)):

Cut 7. The χ^2 from the fit must not be unreasonably large (i.e., the fit must reveal a "good" secondary vertex).

Cut 8. The decay length from the fit must be relatively large (i.e., the lifetime is positive and away from zero).

Cut 9. The minimal radial impact parameter of the three tracks is required to be away from zero (i.e., none of the tracks point directly back to the primary interaction).

Specifically, the signal in Figure 4.2(b) was brought out by demanding that each pKπ combination gave a $\chi^2_* < 10$, a $L_*/\sigma > 6$, and a minimal radial impact parameter $> 50\mu$m. This signal, which has a significance just over 5σ, can be subdivided into Λ_c^+'s and Λ_c^-'s (see Fig. 4.3). The mean mass suggested in these figures (and also indicated in later fits to the signal) is about 10 MeV lower than the current world average[5] of 2.281 GeV, but the value is well within E400's systematic error $\pm$ 30 MeV (as determined by mass distributions of other charm signals as well as mass distributions of K_s and Λ's). Definitions of these "lifetime" cutting variables are given in Appendix A, and their distributions as determined from pKπ combinations are shown in Figures 4.4 and 4.5. Notice that the drastic reduction in the background level is primarily a result of the stiff demand made on L_*/σ . The effects of the L_*/σ cut can be seen in Figure 4.6(a)-(j) which reveals what happens to the Λ_c^+ signal as the cut on L_*/σ is gradually made stiffer. The fitted signals in Figure 4.6 (and in later Λ_c distributions) have constrained widths of about 10 MeV which is consistent with the Λ_c distributions generated by the Monte Carlo (described below). In order to extract a cross section from this Λ_c signal, a reliable Monte Carlo is needed to determine the overall acceptance of this signal. In particular, the effects of cutting on L_*/σ must be well understood since this is the principal cut which rejects background.

4.2 The Monte Carlo

A computer simulation program is written to produce a "fake" raw data tape with chamber wire hits and ADC counts. The program assumes a particular pro-

duction model and then simulates data by swimming the generated tracks through the spectrometer where the appropriate detector responses can be modeled. Input into this program includes geometric settings (such as the locations of wire chambers and Čerenkov cells, etc.), magnetic field maps, and ADC calibration constants. Detector inefficiencies, "spurious" wires hits, and multiple scattering are also simulated. Completed Monte Carlo (MC) raw data tapes are then processed through the Reconstruction program, Pass 2 and Pass 3 just as was done with actual data tapes.

In order to obtain a cross section for $\Lambda_c^+ \rightarrow pK^-\pi^+$, the information needed from the MC is the overall acceptance of this final state. To study this specific final charmed state (and this specific decay mode) a production model must be assumed which will give the desired final charmed state with an accompanying "debris" of particles. The model chosen, however, will only have a mild effect on the acceptance of this state since the acceptance is primarily shaped by model-independent contributions, specifically the geometry of E400's detector and the Čerenkov momentum range of identification. The acceptance resulting from these contributions is largely dependent on the energy of the charmed state, and as such, the acceptance is calculated as a function of the energy of the final state. In the cross section calculations which follow, the acceptance as a function of the Λ_c energy will be seen to be relatively model-independent.

In any case, the principal model used in generating Λ_c's was chosen to be gg fusion (see Fig. 1.1(b)). The explicit expressions developed for this subprocess are given by R. K. Ellis and J. C. Sexton[29]. Let x_1 and x_2 be the fraction of momentum carried off by the interacting gluon from the beam and the interacting gluon from the target, respectively. Then in the center of mass frame, values for x_1 and x_2 are chosen to be consistent with $\hat{\sigma}(\hat{s})_{gg\rightarrow c\bar{c}}$ where $\hat{s} = sx_1x_2$ is the subprocess center of mass energy, and where the gluon momentum distributions are given by $g(x_i) \propto (1-x_i)^N/x_i$ with

$N = 5$ and $i = 1, 2$ (see Eq. (2) of Chapter 1). The c and $\bar{c}$ quarks become final charmed states with unit probability and with no change in momentum. The "debris" is generated as two Feynman Field II jets[30]. One jet carries the remaining beam momentum (i.e., this jet's 4-vector momentum is $(1 - x_1)$ times the incoming beam 4-vector momentum), and the other jet carries the remaining target momentum (i.e., this jet's 4-vector momentum is $(1 - x_2)$ times the target 4-vector momentum). The multiplicity resulting from these jets rises logarithmic in P_{jet}, where in the rest frame of the "debris" $P_{jet} = \sqrt{s(1-x_1)(1-x_2)}/2$. The "debris" is necessary to simulate inefficiencies at the track reconstruction level and confusion in Čerenkov counters at the Pass 2 level.

Since the signal is brought out primarily by a stiff cut on the variable L_*/σ , the interpretation of this cut in the MC should be well understood. First, the resolution of L_*/σ from the data is compared with that found in the MC. To do this, the MC generates Λ_c with no lifetime so that the distribution of L_*/σ from the MC should be similar to that found in **background** pKπ combinations from the data. Comparisons of these "zero lifetime states" are shown in Figures 4.7 and 4.8. Notice that MC and the data agree rather nicely except at the tails of the distribution. This is probably due to hard Coulomb scattering which is not taken into account in the MC, or due to the data having occasional "stray" tracks (i.e., poorly measured tracks which do not point back to the primary vertex). However, for the cross section measurements which follow, the cut on L_*/σ will be less stiff than that which was used earlier (in Fig. 4.2(b)). Instead the cut will be moved in towards the central region of the L_*/σ distribution (say, $L_*/\sigma > 2$) where good agreement between the data and the MC exists. Also notice that Figure 4.8 indicates that resolution on L_*/σ has only a mild energy dependence, changing by about 25% as the energy of the "state" quadruples from 25 GeV to 100 GeV. This mild energy dependence is a direct consequence of

ignoring the error in the primary vertex in the derivation of L_*/σ (see Appendix A - the Correlated Impact Parameter Fit as well as Appendix B which shows how the resolution on the decay vertex can be effected by error on the primary vertex).

Next, the distribution of L_*/σ , of course, depends on the lifetime of Λ_c , and so the MC's choice of the Λ_c lifetime must be taken into account. The resolution of proper lifetime in this experiment is about 0.19 ps (as shown in Appendix A) which is nearly as large as the current world average[5] Λ_c lifetime of $0.23\ ^{+0.8}_{-0.5}$ ps. Even though the Λ_c lifetime can not accurately be measured in this experiment, a natural question arises pertaining to the consistency of the data signal with regards to this current world average Λ_c lifetime. Note, however, that the reported error on this lifetime is nearly 35%. In any case, the amount of signal seen for various cuts on L_*/σ is examined both in the data and in the MC (where $\tau = 0.23$ ps). A comparison is given in Table 4.1. The signal used in this table is represented in Figure 4.6(a)-(g), where only Λ_c^+ is examined since the signal dominates in this sign, and the cuts are identical to those listed earlier (in section 4.1). Once again, there appears to be good agreement between the MC and the data except out at the tails of the L_*/σ distribution.

4.3 Determination of the Λ_c^+ Cross Section

At the present time experimental estimates of total charm cross sections in hadroproduction have large systematic errors (of the order of 50% or more). A major contribution to these errors is due to the uncertainties in the branching ratios of charmed particles decays. Another major source of error results from uncertainty in determining the fraction of charm signal that falls outside the region of acceptance for a given detector or the fraction of signal excluded by a significant trigger bias. The total charm cross section measurements for such experiments depend heavily on the chosen production model. In the cross section measurements below, a special effort

has been made to minimize model dependence by adopting a "weighting" method.

The basic idea of this method is to first extract the acceptance corrected signal strength by fitting a weighted mass distribution of Λ_c^+ candidates. A given Λ_c^+ candidate is entered into the mass histogram weighted by the reciprocal of its total acceptance (as determined by geometric acceptance and the efficiencies of the applied analysis cuts including trigger efficiencies). This total acceptance is primarily dependent on the candidate's energy. Then a value for $\sigma \cdot BR$ can be determined from the ratio of this acceptance corrected signal strength to the data sample luminosity which is derived from the number of "live" master gates combined with information on the total inelastic cross section per nucleon.

The calculation presented gives an estimate of $\sigma \cdot BR$ for $\Lambda_c^+ \rightarrow \mathrm{pK}^-\pi^+$ over a specified region of acceptance. Estimates of the total charm cross section will be highly model dependent and somewhat speculative and will not be addressed here (but more details on the total cross section are given in the conclusion – Chapter 5). The calculation for $\sigma \cdot BR$ can be expressed as follows:

$$\sigma(\text{n-nucleus} \rightarrow \Lambda_c^+ X) \cdot BR(\Lambda_c^+ \rightarrow pK^-\pi^+) = \frac{N_{obs} \cdot \sigma_{eff} \cdot \epsilon_{MG}}{N_{MG} \cdot \epsilon_L \cdot \epsilon_{Si33} \cdot \epsilon_{spectrum}}$$

where

1. N_{obs} is the number of Λ_c^+'s observed weighted by the overall acceptance including the M7 trigger efficiency. An additional weighting factor exists on only those events that were collected with the PIN 4 Lo Mult trigger, which rejected high multiplicity events.
2. The value for $\sigma_{eff} \cdot \epsilon_{MG}$ is the effective inelastic cross section per nucleon times the efficiency of the master gate (MG). When assuming a linear A dependence, σ_{eff} can be computed for the various target materials as the average of *density* × *thickness* × *inelastic cross section per nucleon* (where the effects of different A dependence assumptions are presented later). This gives σ_{eff} at approximately 16mb. The MG efficiency factor (85% ± 15%) is necessary to take into account event topologies not observed in E400's detector, for example, events having all tracks opening at angles large enough to miss E400's spectrometer or events with all neutral particles. This efficiency was determined from the topological cross

sections measured in a recent bubble chamber experiment conducted at FNAL near E400's energies[31].

3. $N_{MG} \cdot \epsilon_L \cdot \epsilon_{Si33} \cdot \epsilon_{spectrum}$ is the number of master gates as determined by a counting scaler ($\sim 675 \times 10^6$) times the product of three fractions. The first fraction, ϵ_L, gives the overall livetime (also found by counting scalers and is about 49%). The second term, $\epsilon_{Si33} \simeq 65\%$, is the fraction of luminosity observed by demanding that a "live" Silicon wafer fires "on" in the target region (see busline # 2 in Chapter 2, section 4). The final fraction, $\epsilon_{spectrum} \simeq 82\%$, is the observed fraction of the incident neutron energy spectrum (i.e., neutron energies below 300 GeV are not recorded). Note that the N_{MG} value given excludes a small portion of E400's data which was taken with an anomalously high event energy trigger.

To calculate N_{obs}, a signal plot has been chosen that requires a minimal number of "stiff" analysis cuts. This is done in hopes of reducing systematic biases. The unweighted (or "raw") signal is shown in Figure 4.9(a). The cuts are identical to those listed earlier in section 4.1, except the minimal radial impact parameter cut (i.e., Cut # 9 on page 68) has been completely removed and the cuts associated with the impact parameter fit variables are now:

Cut 7. $\chi^2_* < 6$ to ensure a "good" secondary vertex, and

Cut 8. $L_*/\sigma > 2$ to ensure a "long" decay length without cutting out on the tail of the distribution.

In addition to these cuts, a selected pKπ combination was required to have an energy that fell within the measured acceptance range as determined by the MC (see Fig 4.10 (a), which is described in detail shortly):

Cut 10. 50 GeV $< E_{pK\pi} <$ 140 GeV to ensure "reasonable" acceptance.

Note that the fit shown it Figure 4.9(a) reveals a "raw" Λ_c^+ signal that has about 72 $\pm$ 21 events. The choice to use only Λ_c^+ in measuring the cross section was motivated by the fact that the observed signal is dominated by this charge and by the fact that other hadroproduction experiments[14-18] which have seen this signal report the cross section for only this charge. The ratio of Λ_c^+ to Λ_c^- will be examined in the next section.

This signal must be weighted by acceptance and by the M7 trigger efficiency. The acceptance is plotted as function of the energy of MC Λ_c^+'s (see Figure 4.10(a)). The acceptance fraction is determined by dividing the number of MC Λ_c^+'s that remain (after requiring geometric acceptance and analysis cuts) by the number that was initially generated for a given energy of the state. The Λ_c^+'s were generated through the decay mode $\Lambda_c^+ \rightarrow pK^-\pi^+$ using the current world average of 0.23 ps for the lifetime[5]. Note, that the Λ_c^+'s which appear in the numerator of this fraction survived the usual data processing phases and also passed all PIN 4 trigger requirements (such as the energy busline) excluding the M7 trigger which is handled as described shortly because of it's complexity and excluding the demand that a Silicon wafer fire "on" in the target region (which is handled as a separate correction to N_{MG}).

As stated earlier, the acceptance curved is only mildly dependent on the production model. In gluon-gluon fusion the final charmed states generated have a momentum distribution function that goes as $(1- \mid x_f \mid)^8$ for large x_f, but suppose a model is used that invokes a much broader x_f distribution, say $(1- \mid x_f \mid)^2$. Such a model has only a mild effect on the acceptance curve as can be seen in Figure 4.10(b).

The acceptance curve does depend on the lifetime of Λ_c^+ , but within the reported errors[5] , only about a 15% change in acceptance occurs at the peak of the curve. Figure 4.11(b) is the acceptance curve for Λ_c^+'s generated with a lifetime of 0.31 ps.

The M7 trigger efficiency was studied with unbiased master gate data events (i.e., PIN 2 events) where a formula was derived which expresses the probability of the M7 "taking" the event as a function of the number of particles falling into categories of specified Čerenkov ID's and specified momentum regions (see Table 4.2). The effectiveness of this M7 trigger probability expression can be seen in a direct comparison of this prediction to the actual M7 trigger fraction as measured by the

master gate data events (see Fig. 4.12). Each event in Figure 4.9(a) must be weighted by the M7 triggering probability which is typically around 50%. The distribution of the M7 trigger antecedent efficiency is shown in Figure 4.13.

Finally, those events which were collected under the PIN 4 Lo Mult trigger must be weighted by that trigger efficiency. The main effect of the Lo Mult trigger is to pass only those events which have somewhat lower multiplicities than those accepted under the PIN 4 Hi Mult trigger (see section 2.4 for more details). However, a demand made later by the event selection process imposed a hard multiplicity cut on all pKπ combination events (see Cut # 1 in section 4.1). This event selection cut required that the event multiplicity had to be less than 12, as such, the differences between PIN 4 Lo Mult and PIN 4 Hi Mult are rather minor. In any case, the Lo Mult trigger efficiency for events which have multiplicities less than 12 is about 85%.

Using the appropriate event weighting factors described above, Figure 4.9(a), is now re-plotted to give the distribution shown in Figure 4.9(b). Note, that this weighted distribution falls within an energy region of 50 to 140 GeV. This energy region corresponds to reasonable levels of acceptance (above 0.1%) as determined by the acceptance curve (Fig. 4.10(a)). The fit reveals that N_{obs} is 27464 $\pm$ 14301 events, giving

$$\sigma(\text{n-nucleus} \rightarrow \Lambda_c^+ X) \cdot BR(\Lambda_c^+ \rightarrow pK^-\pi^+) \;=\; 2.1 \pm 1.1(\pm 0.74)\mu\text{b/nucleon}$$

where the Λ_c^+ energies are between 50 and 140 GeV and the incident neutron energy is between 300 GeV and 800 GeV. The first error is statistical (as established by the fit to the weighted Λ_c^+ mass distribution), and the second error is systematic (35%) which includes the effects of luminosity uncertainty ($\pm$20%), model dependence($\pm$20%), life-time uncertainty($\pm$15%), and differences ($\pm$10%) found by assuming various $E_{pK\pi}$ ranges in Cut # 10.

To determine an energy independent cross section, the average beam energy can be computed. Let the average neutron energy be expressed as ω. An estimate of the x_f of a given Λ_c^+ with energy E and transverse momentum $P_\perp = \sqrt{P_x^2 + P_y^2}$ is given by

$$x_f = \frac{E}{\omega} - \frac{M_\perp^2}{2M_N E} \quad \text{with} \quad M_\perp \equiv \sqrt{M_{\Lambda_c}^2 + P_\perp^2}.$$

So, by plotting the energy of Monte Carlo accepted Λ_c^+'s as a function of their x_f one can find the best value of ω. Figure 4.14 shows such a plot, and the solid line represents the above expression with ω set to 565 GeV (giving $\sqrt{s} = 33$ GeV). Thus, $\sigma \cdot BR = 2.1 \pm 1.1 \pm 0.74 \mu$b/nucleon at $\sqrt{s} \simeq 33$ GeV and for $0.028 < x_f < 0.226$.

Table 4.3 list $\sigma \cdot BR$ measurements for various final state energy ranges and for various model assumptions. As an additional example, the "raw" signal and the acceptance weighted signal for the energy range between 70 and 120 GeV is shown in Figure 4.15(a) and (b), respectively. Also given in the table are differential cross sections with respect to x_f evaluated at $x_f = 0.13$. Since the momentum distribution function of the final charmed state is of the form $(1- \mid x_f \mid)^N$ with $N > 1$, a small value for x_f, such as $x_f = 0.13$, gives a differential cross section which is relatively model independent. Over a sufficiently small x_f range, where the x_f dependance is approximately linear, the differential cross section at $\bar{x}_f = \frac{x_1+x_2}{2}$ will equal the integrated cross section (from $x_1 \rightarrow x_2$) divided by $x_2 - x_1$. Or, alternatively, the differential cross section can be calculated by setting $N = 4$ (which is an average value obtained in recent charm hadroproduction experiments[12] including E400[34]) and applying the formula:

$$BR \cdot \frac{\partial \sigma}{\partial x} = BR \cdot \sigma_{tot} \left(\frac{N+1}{2} \right) (1 - |\bar{x}|)^N \quad \text{where} \quad \bar{x} = \frac{x_2 + x_1}{2},$$

and where $BR \cdot \sigma_{tot}$ is deduced from $BR \cdot \sigma(x_1 \rightarrow x_2)$ by appropriate integration of the $(1 - |x|)^N$ form. Only a 12 % variation in this differential cross section will occur

as N is varied from 0 to 8. To facilitate comparisons, the differential cross sections for different energy ranges is evaluated at the common average value of $x_f = 0.13$. Notice, that these differential cross sections are consistent for the various final state energy ranges being considered. The final column in the table gives $\sigma \cdot BR$ over the entire x_f range (i.e., $BR \cdot \sigma_{tot}$) assuming the final charmed state has a momentum distribution function of the form $(1- \mid x_f \mid)^N$ where $N = 2$, 4 or 6.

The values of $\sigma \cdot BR$ given above assume a linear A dependence. If instead, $A^{0.75}$ is used as suggested by a couple of experimental results[32], then $\sigma_{eff} = 36.6$ μb which increases $\sigma \cdot BR$ by over a factor of 2. More recent calculations[33], including results from this experiment[34], have indicated that $A^{0.90}$ is perhaps a better choice, which increases $\sigma \cdot BR$ by about 30%. More formally, for charm cross sections with an A^α dependence, the value of σ_{eff} is given by:

$$\sigma_{eff} = \frac{\sum \rho_i t_i \sigma_i / A_i}{\sum \rho_i t_i A_i^{\alpha-1}}$$

where the sum is over the different target materials (W, Be, and Si) and the density times thickness of each material is represented as $\rho_i t_i$ (– for qualitative information on the target, see Chapter 2). The effect of the A^α dependence on the Λ_c^+ differential cross section (using the first entry in Table 4.3) is illustrated in Figure 4.16.

Additional uncertainty in the cross section estimates above results from the total event multiplicity found in the Λ_c signal. The Monte Carlo event multiplicity generated for accepted Λ_c^+'s is shown in Figure 4.17. The requirement that the selected events have fewer than 12 tracks (Cut # 1 in section 4.1) gave a weighting factor that nearly doubled the number of signal events since about half the MC signal exists below this cut. A theoretical model which accurately predicts the multiplicities accompanying charm signals in hadroproduction does not exist. If one makes the unlikely assumption that essentially all Λ_c^+'s are produced with event multiplicities below 12, then the

cross sections given above would be lowered by a factor of 2. On the other, if one assumes that essentially all Λ_c^+'s are produced with multiplicities above 12, then the cross sections must be greatly increased.

4.4 Properties of the Λ_c Signal

This section focuses on whether or not the observed Λ_c^+ and Λ_c^- signals are produced symmetrically (i.e., whether or not these states have similar production rates and/or similar momentum). One indication of the production differences may be given by the ratio of Λ_c^+ to Λ_c^- as seen from fits to the unweighted mass distributions. Using acceptance weighted distributions would result in large uncertainties (as can been seen from the weighted signal histograms of the previous section). As stated earlier, the dominate contribution to the signal appears to be Λ_c^+ . Figures 4.2(b) and 4.3 (referred to in section 4.1) reveal that Λ_c^+ does indeed dominate the observed signal. Using the same analysis cuts, but "loosening" the L_*/σ cut to $L_*/\sigma > 2$ (to obtain somewhat better statistics) gives the comparison shown in Figure 4.18. Fits to these signals reveal that the fraction $\Lambda_c^+ /(\Lambda_c^+ + \Lambda_c^-)$ is at about 78% $\pm$ 18% indicating that equal production of these signals is inconsistent with these fits at about the 1.5σ level.

Using the same cuts, the Λ_c^+ signal can be divided into two separate final state energy regions (above and below 70 GeV, which is roughly the mid-point of the energy distribution of unweighted pKπ combinations). Figures 4.19 reveals that just over half of the Λ_c^+ signal has lab energies above 70 GeV. The fit (in fig. 4.19) suggests that the fraction of the Λ_c^+ signal with lab energies greater than 70 GeV relative to the total Λ_c^+ signal is about 64% $\pm$ 18% which is within 1σ of equally dividing the Λ_c^+ signal. Because of the poor signal to background ratio in the Λ_c^- category it is difficult to make the same comparisons in this category as done in the Λ_c^+ category. Somewhat more

restrictive cuts on L_*/σ (i.e., demanding $L_*/\sigma > 4$ or 6 rather than $L_*/\sigma > 2$) help to improve the Λ_c^- signal to background level. However, attempts to fit these Λ_c^- signals (which are shown in Figs. 4.20 and 4.21) result in very poor χ^2's. Even though the majority of the Λ_c^- signal appears to have final state energies below 70 GeV (rather than above 70 GeV as mildly suggested in the Λ_c^+ signal), the large uncertainties in the number of Λ_c^- signal events indicates that this signal is not inconsistent with being equally divided at 70 GeV. Fits to the sum of Λ_c^+ and Λ_c^- for final states with energy above 70 GeV (in Figure 4.22) indicate that the fraction $\Lambda_c^+ /(\Lambda_c^+ + \Lambda_c^-) \simeq 85\% \pm 25\%$ which is nearly the same as the fraction found without the energy cut.

The Λ_c^+ signal can also be divided into two separate regions of its transverse component of momentum (or $P_\perp \equiv \sqrt{P_x^2 + P_y^2}$), where one region accepts $P_\perp < 700$ MeV , and the other region accepts $P_\perp > 700$ MeV. The value of 700 MeV is chosen since it is nearly the mid-point on the $P_\perp$ distribution of pKπ combinations. The fits in figure 4.23 indicate that about half of the observed Λ_c^+ signal has $P_\perp$ above 700 MeV where the fraction of Λ_c^+ signal with $P_\perp$ above 700 MeV is $52\% \pm 15\%$.

Table 4.1 Lifetime consistency check.
Percentages of Λ_c^+'s above a specified L_*/σ cut relative to $L_*/\sigma > 0$.
Lifetime of Λ_c's in the Monte Carlo is set to 0.23 ps.

Cut on L_*/σ	Monte Carlo (8099 events)	Data (187 $\pm$ 66.8 events)
$L_*/\sigma > 0$	100%	100%
$L_*/\sigma > 1$	62.7% $\pm$ 0.5%	74.0% $\pm$ 22.4%
$L_*/\sigma > 2$	34.3% $\pm$ 0.5%	33.5% $\pm$ 14.1%
$L_*/\sigma > 3$	17.4% $\pm$ 0.4%	14.5% $\pm$ 8.3%
$L_*/\sigma > 4$	9.58% $\pm$ 0.3%	12.7% $\pm$ 6.7%
$L_*/\sigma > 5$	5.72% $\pm$ 0.3%	13.8% $\pm$ 6.1%
$L_*/\sigma > 6$	3.57% $\pm$ 0.2%	10.9% $\pm$ 5.0%

Table 4.2 Parameterization of M7 efficiency.

5 catagories of particles are considered. The individual firing probabilities are denoted p_i. For events with N_i particles of type i the firing probability is:

$$P_{M7} = 1 - \prod_{i=1,5} (1 - p_i)^{N_i}.$$

i	ISTATL	P RANGE	p_i
1	4	$P > 21GeV$	0.33
2	12	$10 < P < 25GeV$	0.082
3	12	$P > 25GeV$	0.29
4	8	$P > 40GeV$	0.25
5	$\tilde{\pi}^*$	All P	$0.03 + 0.00125 \times N_{\tilde{\pi}}$

* A $\tilde{\pi}$ is any particle other than those in entry $1 \rightarrow 4$

Thus:

$$N_5 = NTBIG - \sum_{i=1,4} N_i.$$

Table 4.3 Estimates of $\sigma(np \to \Lambda_c^+ X) \cdot BR(\Lambda_c^+ \to pK^-\pi^+)$.

Λ_c^+ Energy (GeV)	$\sigma \cdot BR$, (μb)	x_f Range	$\frac{\partial\sigma}{\partial x}(\bar{x} = .13) \cdot BR$, ($\mu$b)	$\sigma_{tot} \cdot BR$, For $-1 < x < 1$ $N = 2$, $N = 4$, $N = 6$ (μb)
50 to 140	2.12 ± 1.10(±0.74)	.028 to .226	10.3 ± 5.3 (±3.6)	9.23, 7.11, 6.42
60 to 130	1.81 ± 0.68(±0.63)	.056 to .207	11.9 ± 4.4 (±4.2)	10.55, 8.29, 7.67
70 to 120	1.62 ± 0.50(±0.57)	.081 to .187	15.4 ± 4.7 (±5.4)	13.50, 10.72, 10.10
80 to 110	0.69 ± 0.36(±0.24)	.104 to .167	11.1 ± 5.8 (±3.9)	9.70, 7.77, 7.39

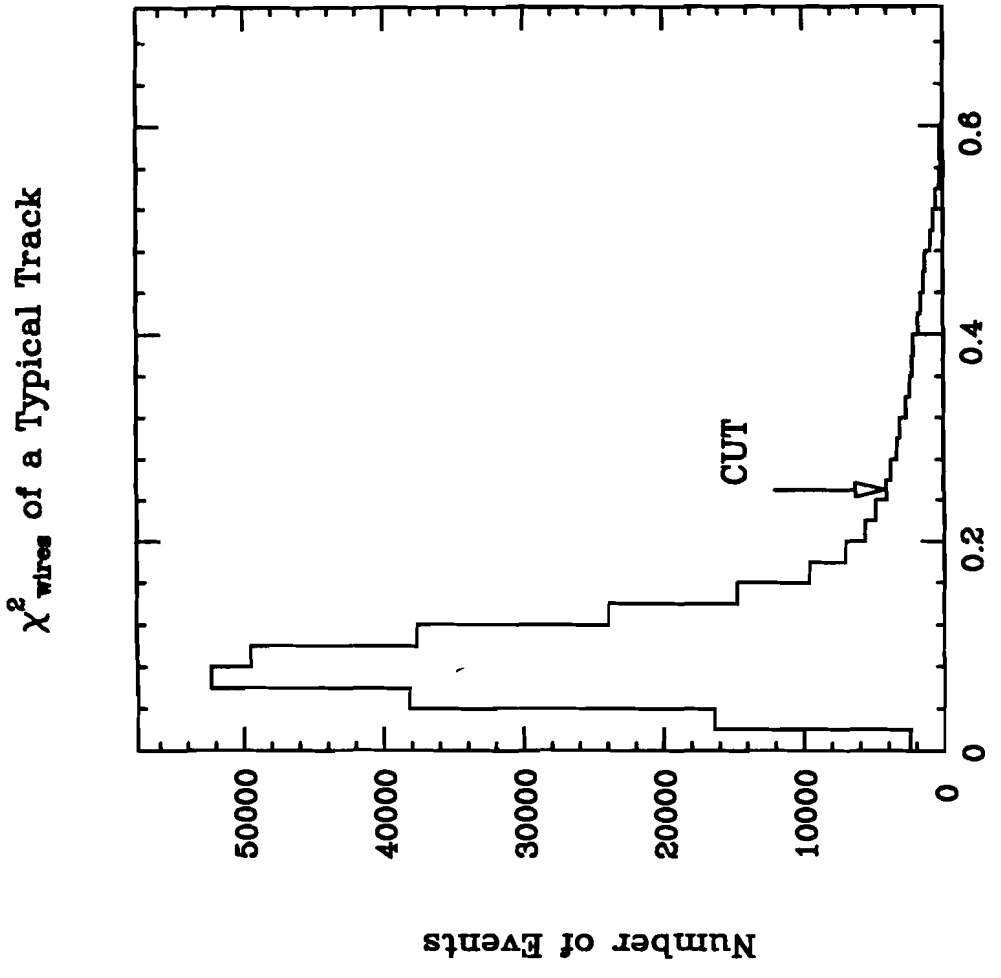
χ^2_{wires} of a Typical Track
Number of Events
50000
40000
30000
20000
10000
0
0
0.2
0.4
0.6
CUT

Figure 4.1

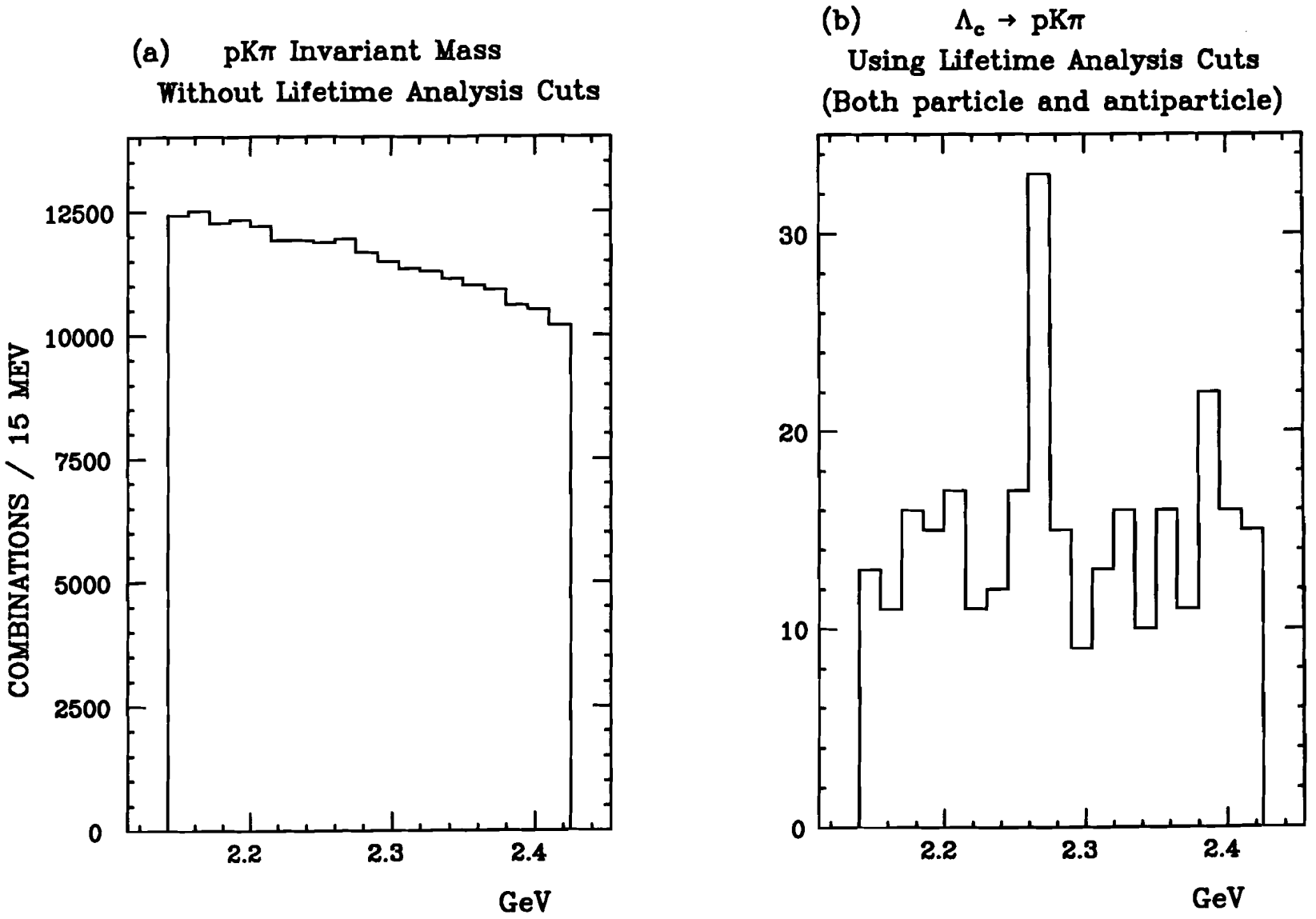
(a) pKπ Invariant Mass
Without Lifetime Analysis Cuts
COMBINATIONS / 15 MEV
12500
10000
7500
5000
2500
0
2.2
2.3
2.4
GeV
(b) $\Lambda_c \rightarrow pK\pi$
Using Lifetime Analysis Cuts
(Both particle and antiparticle)
30
20
10
0
2.2
2.3
2.4
GeV

Figure 4.2

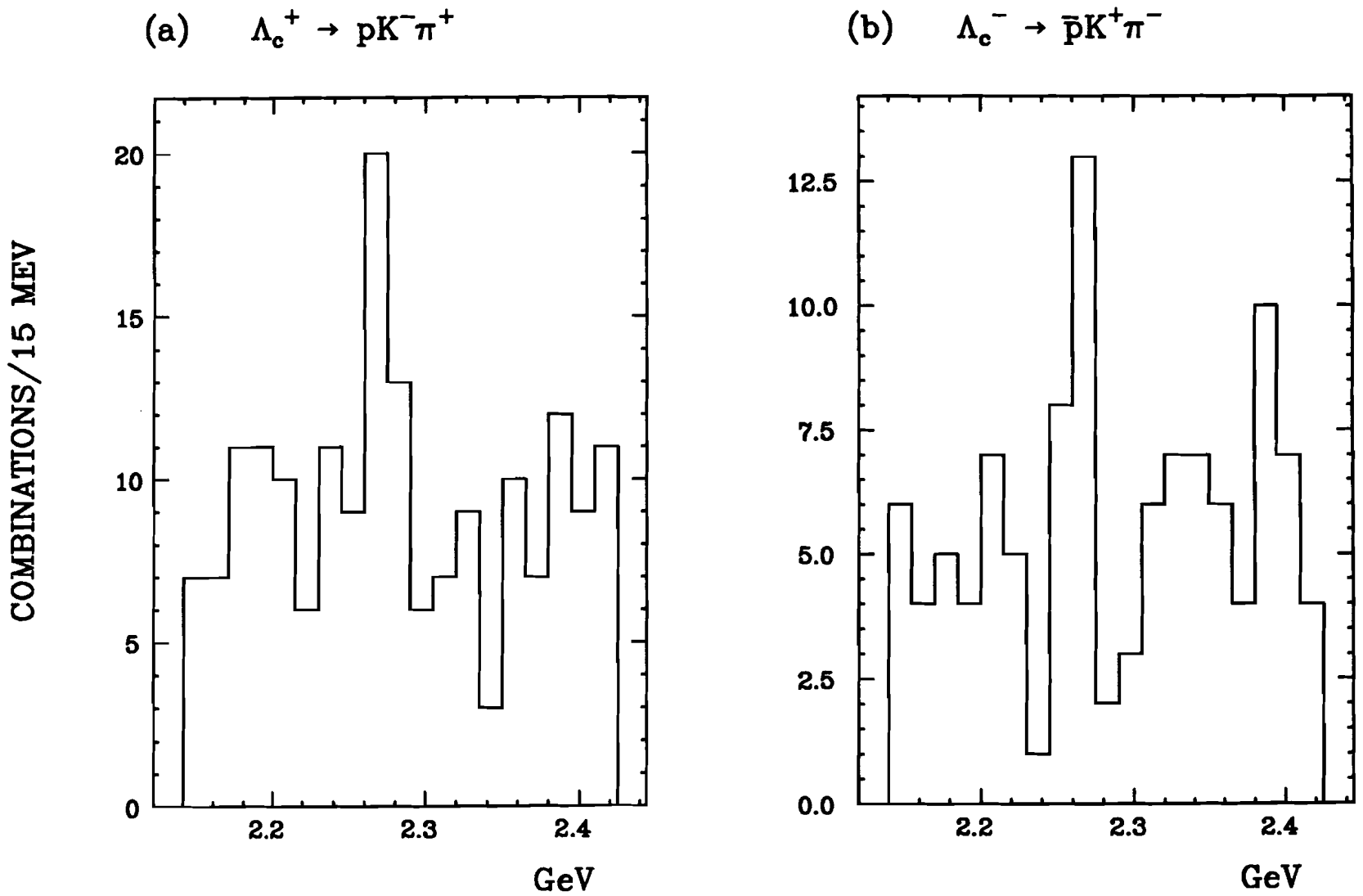
(a) $\Lambda_c^+ \rightarrow pK^-\pi^+$
(b) $\Lambda_c^- \rightarrow \bar{p}K^+\pi^-$
COMBINATIONS/15 MEV
0
5
10
15
20
2.2
2.3
2.4
GeV
0.0
2.5
5.0
7.5
10.0
12.5
2.2
2.3
2.4
GeV

Figure 4.3

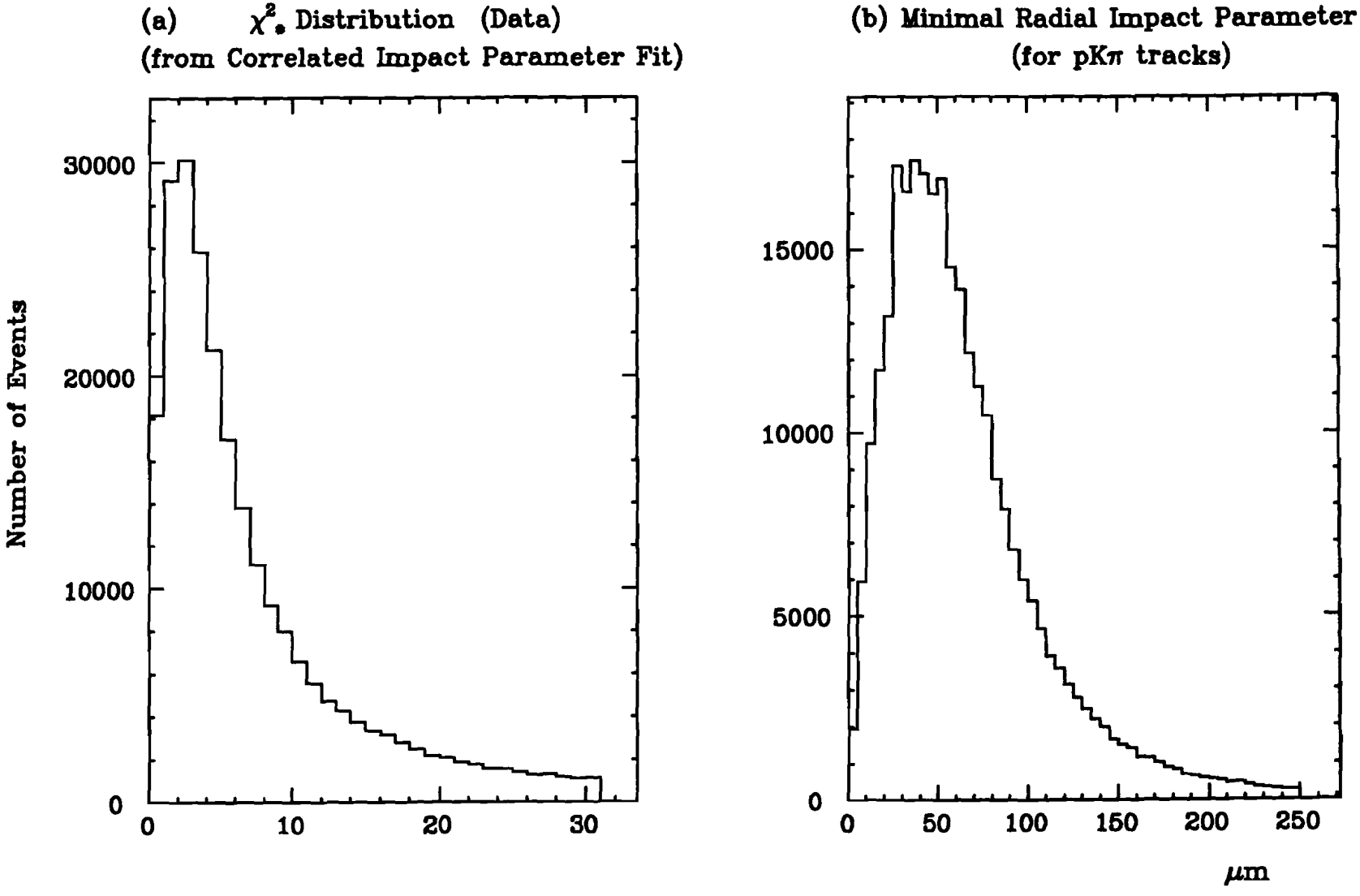
(a) χ^2_* Distribution (Data)
(from Correlated Impact Parameter Fit)
Number of Events
30000
20000
10000
0
0
10
20
30
(b) Minimal Radial Impact Parameter
(for pKπ tracks)
15000
10000
5000
0
0
50
100
150
200
250
μm

Figure 4.4

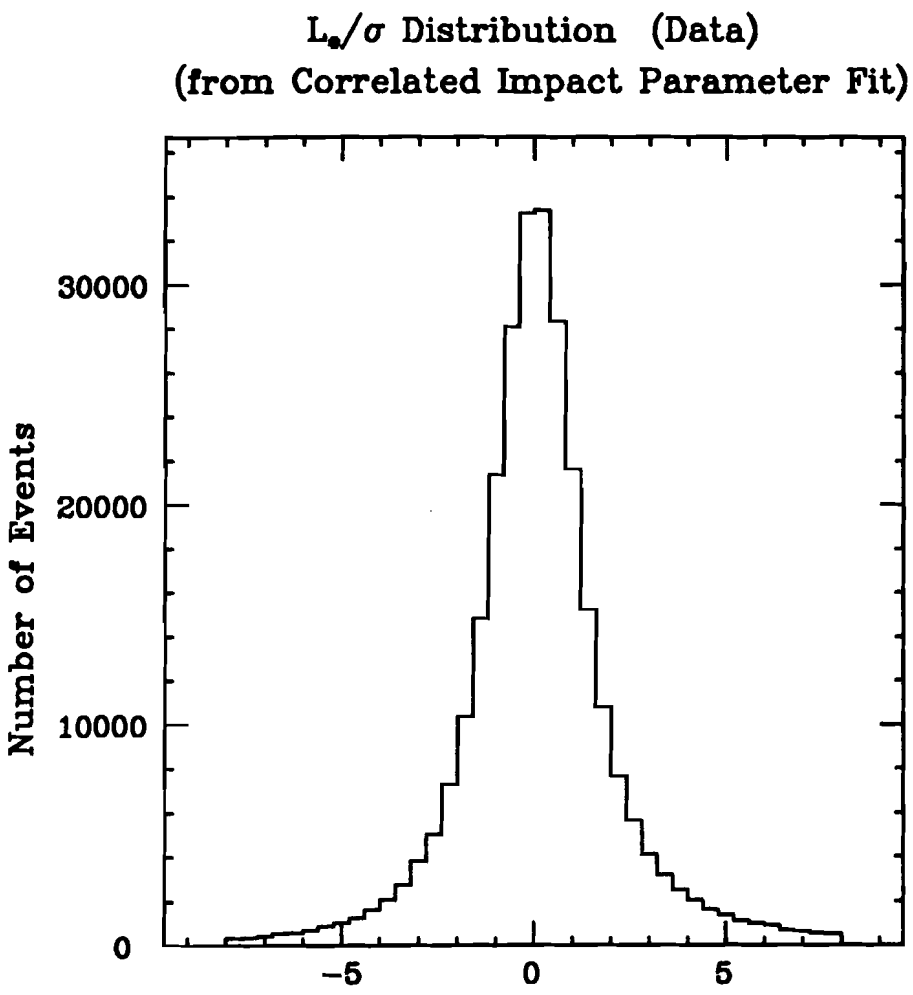
L$_s$/σ Distribution (Data)
(from Correlated Impact Parameter Fit)
Number of Events
30000
20000
10000
0
−5
0
5

Figure 4.5

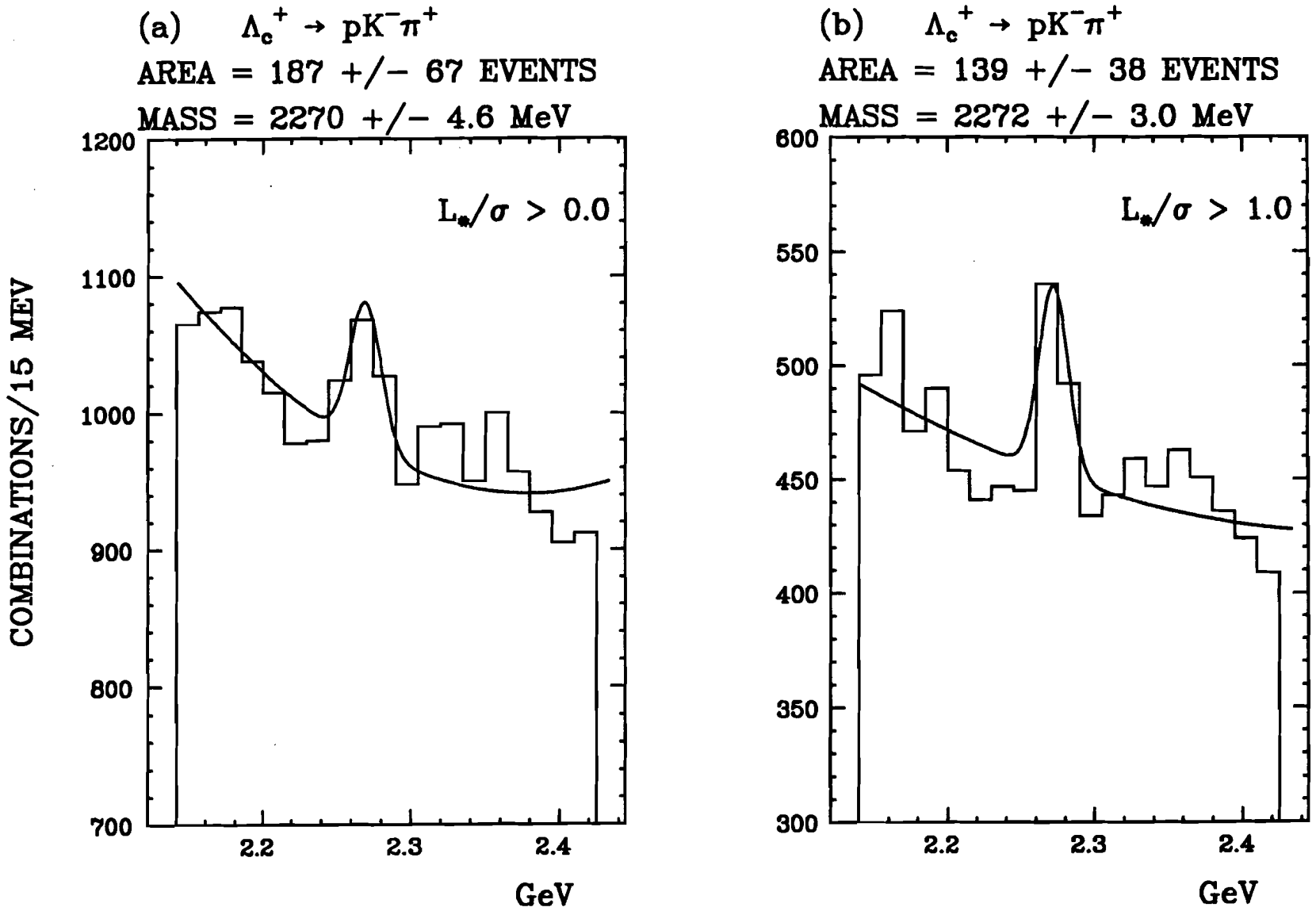

Figure 4.6 Λ_c^+ signal, applying incremental L_*/σ cuts.

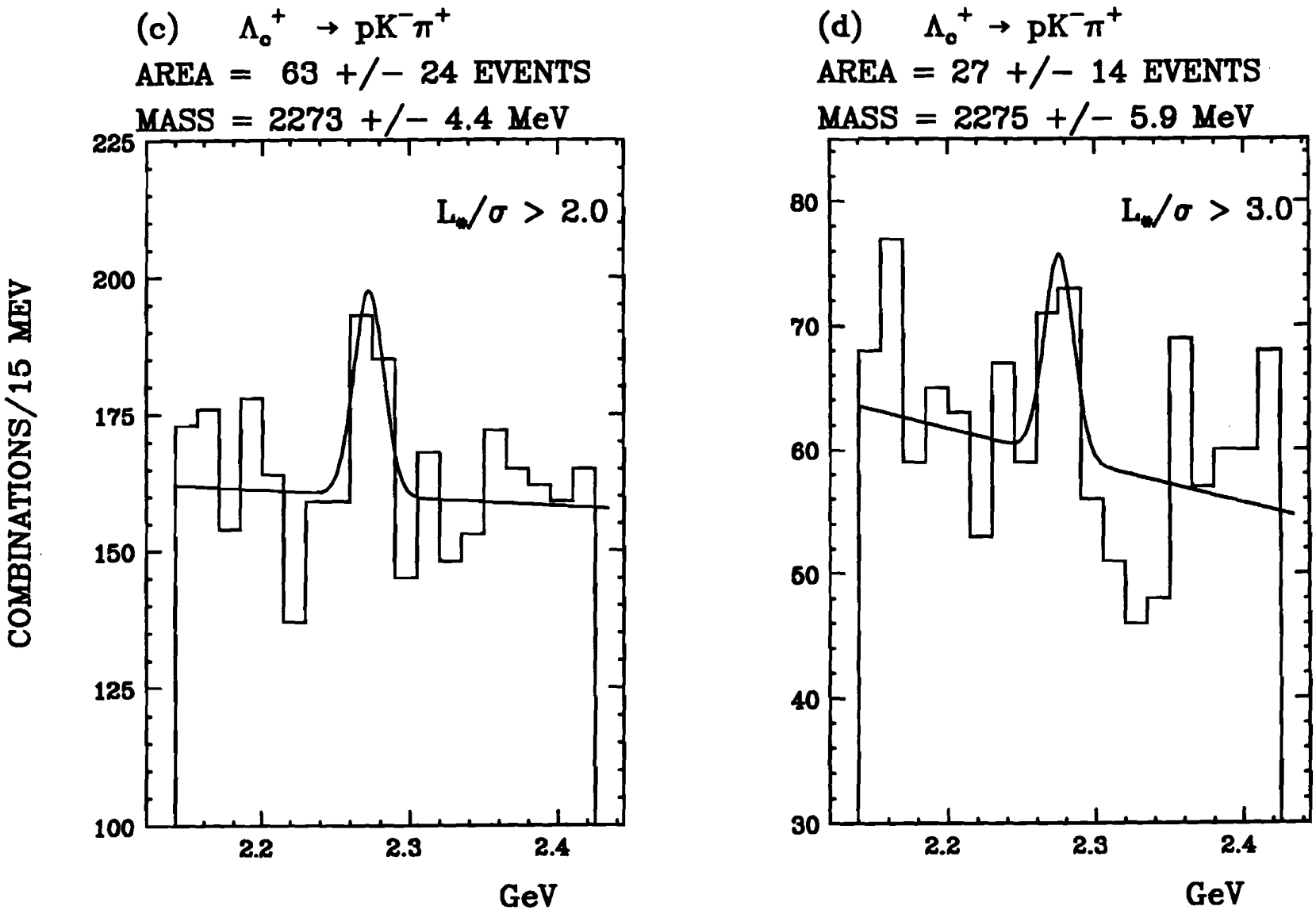

Figure 4.6 (continued)

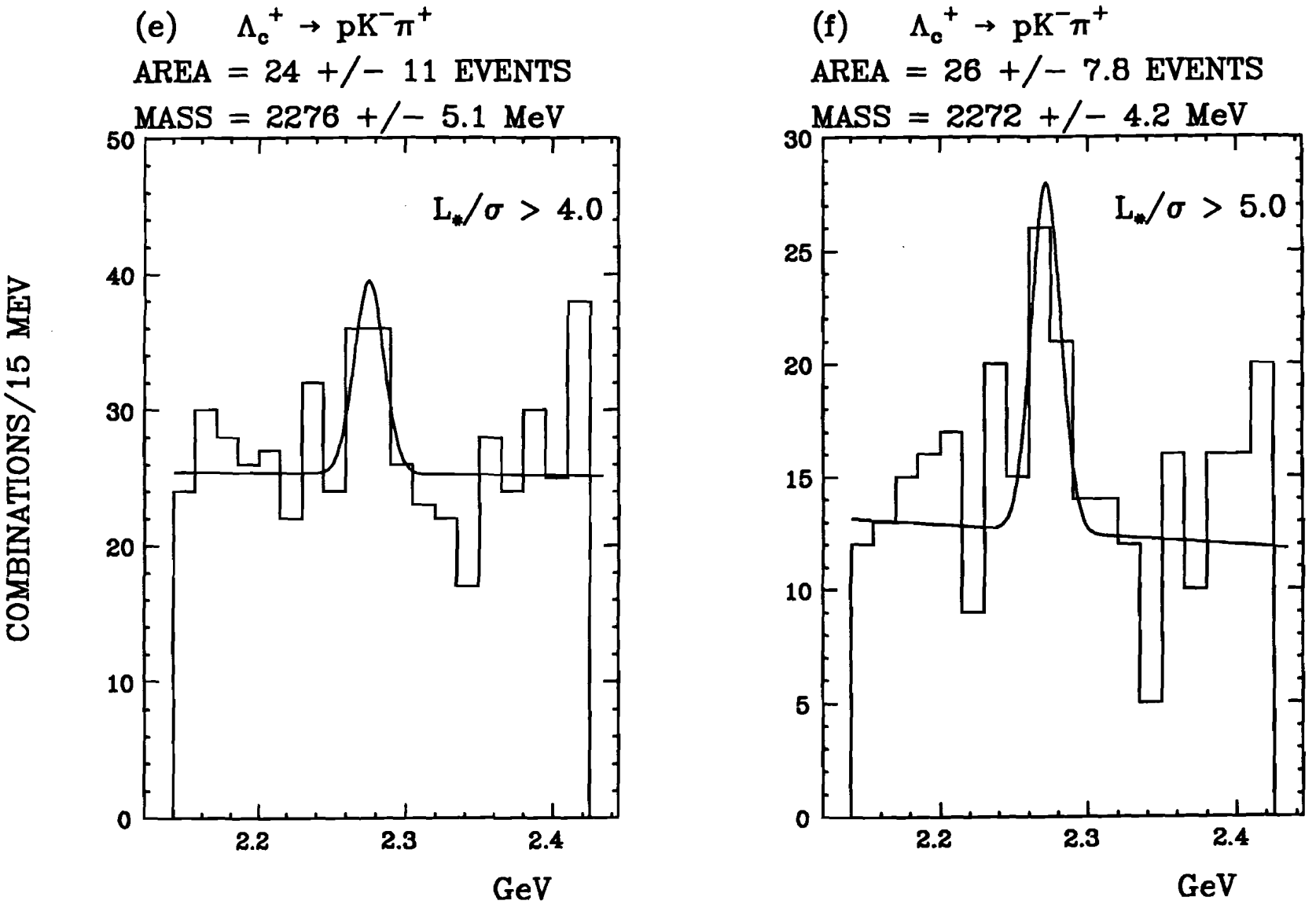

Figure 4.6 (continued)

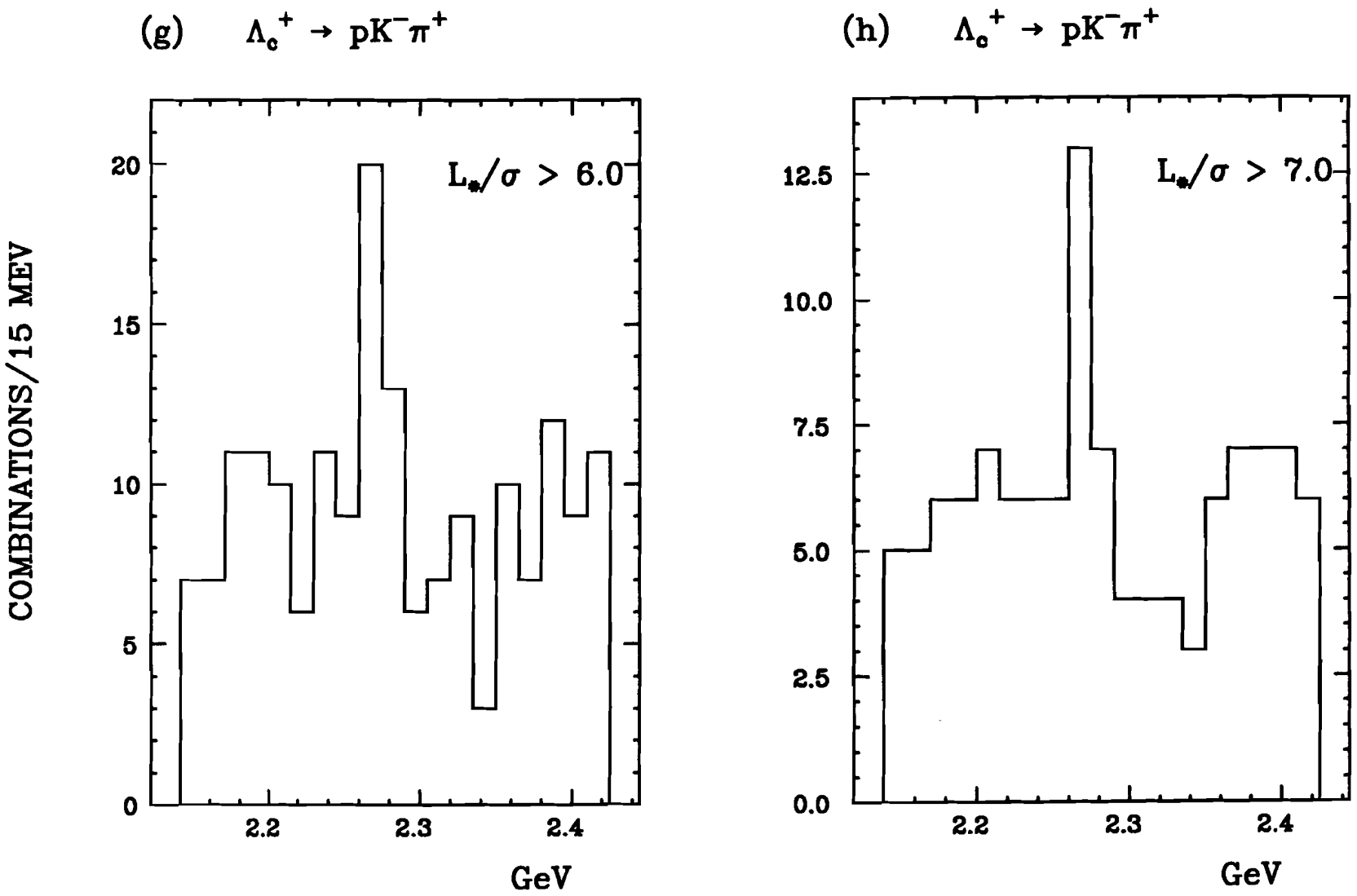

Figure 4.6 (continued)

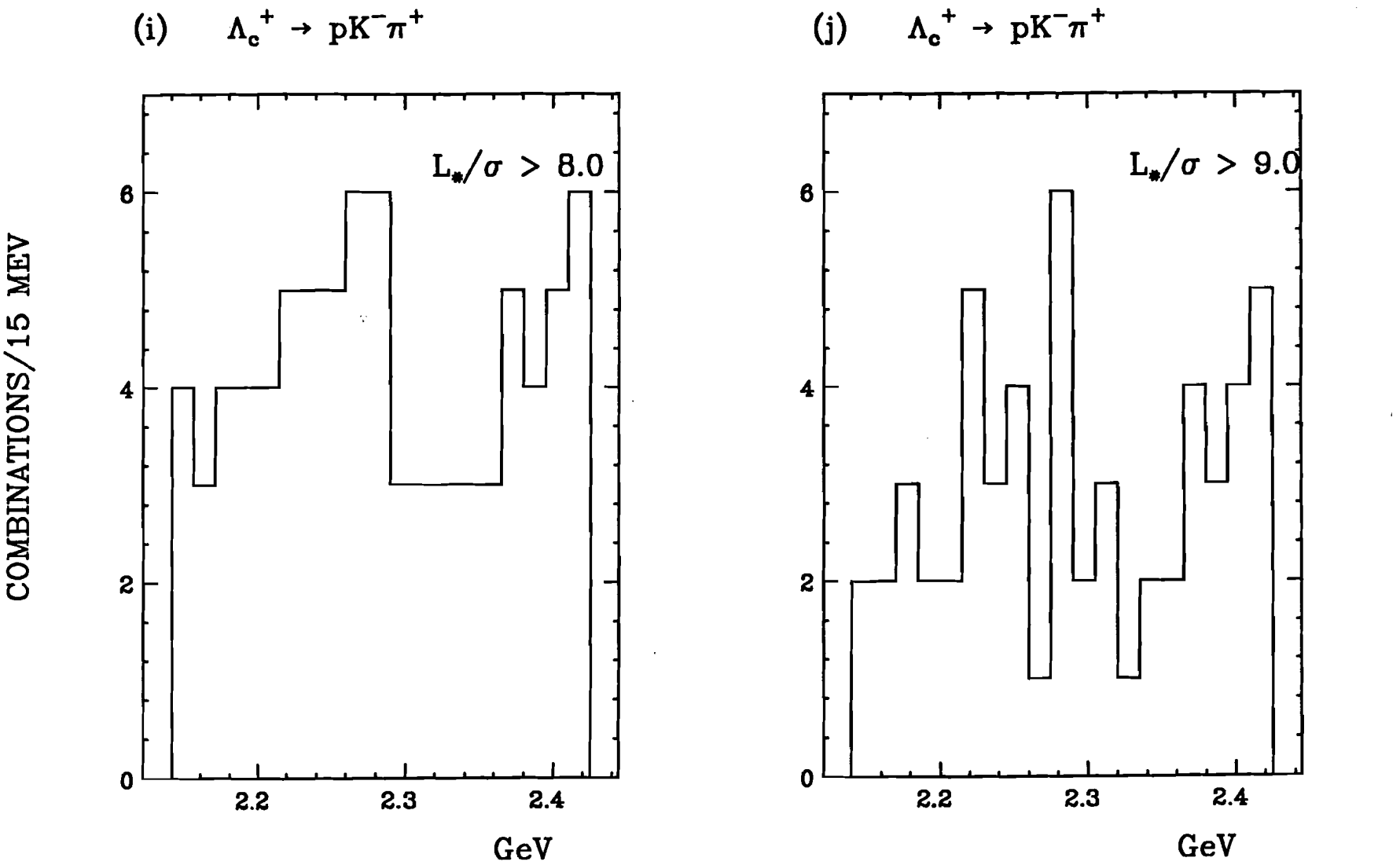

Figure 4.6 (continued)

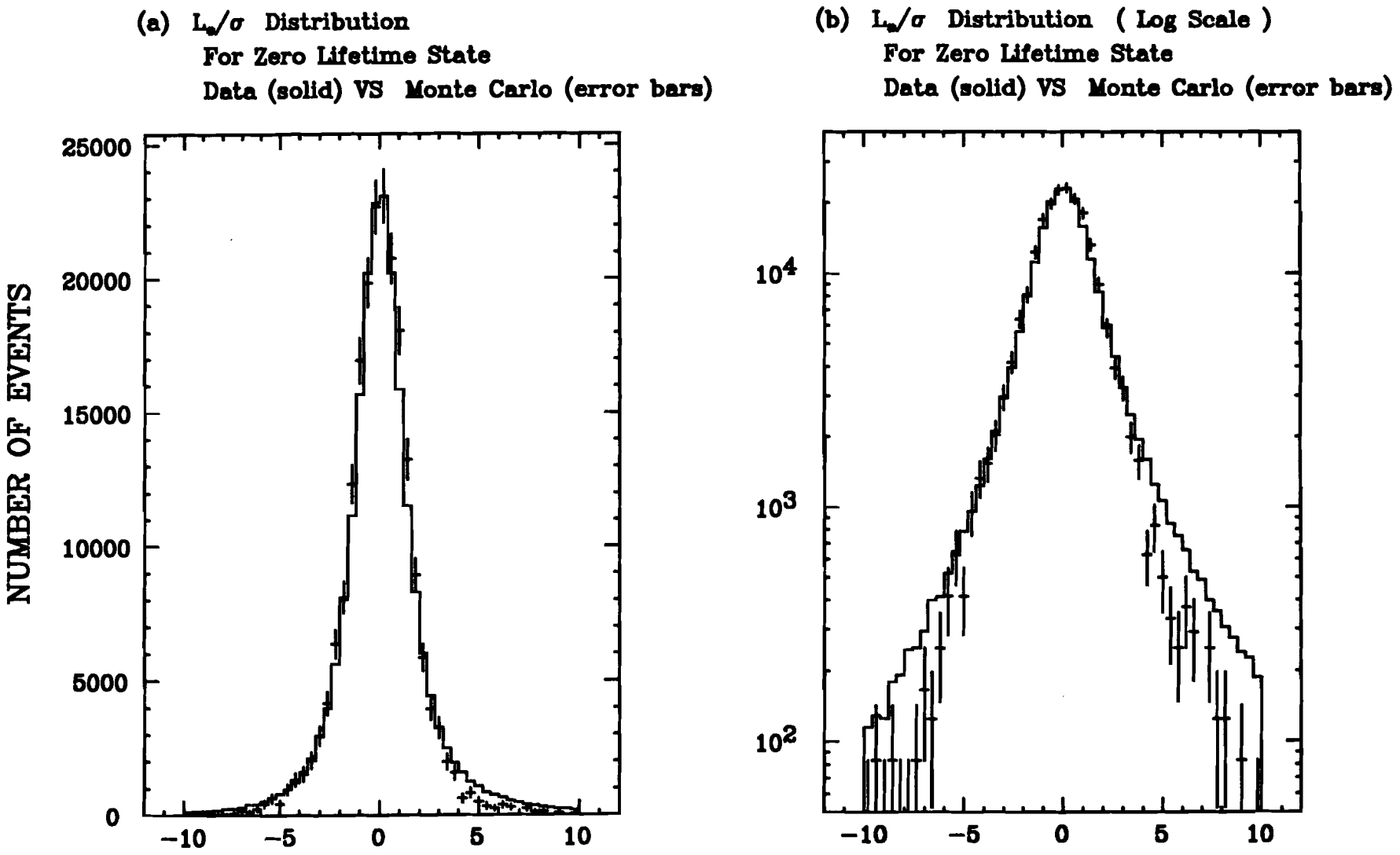
(a) L_{xy}/σ Distribution
For Zero Lifetime State
Data (solid) VS Monte Carlo (error bars)
NUMBER OF EVENTS
25000
20000
15000
10000
5000
0
−10
−5
0
5
10
(b) L_{xy}/σ Distribution (Log Scale)
For Zero Lifetime State
Data (solid) VS Monte Carlo (error bars)
10^4
10^3
10^2
−10
−5
0
5
10

Figure 4.7

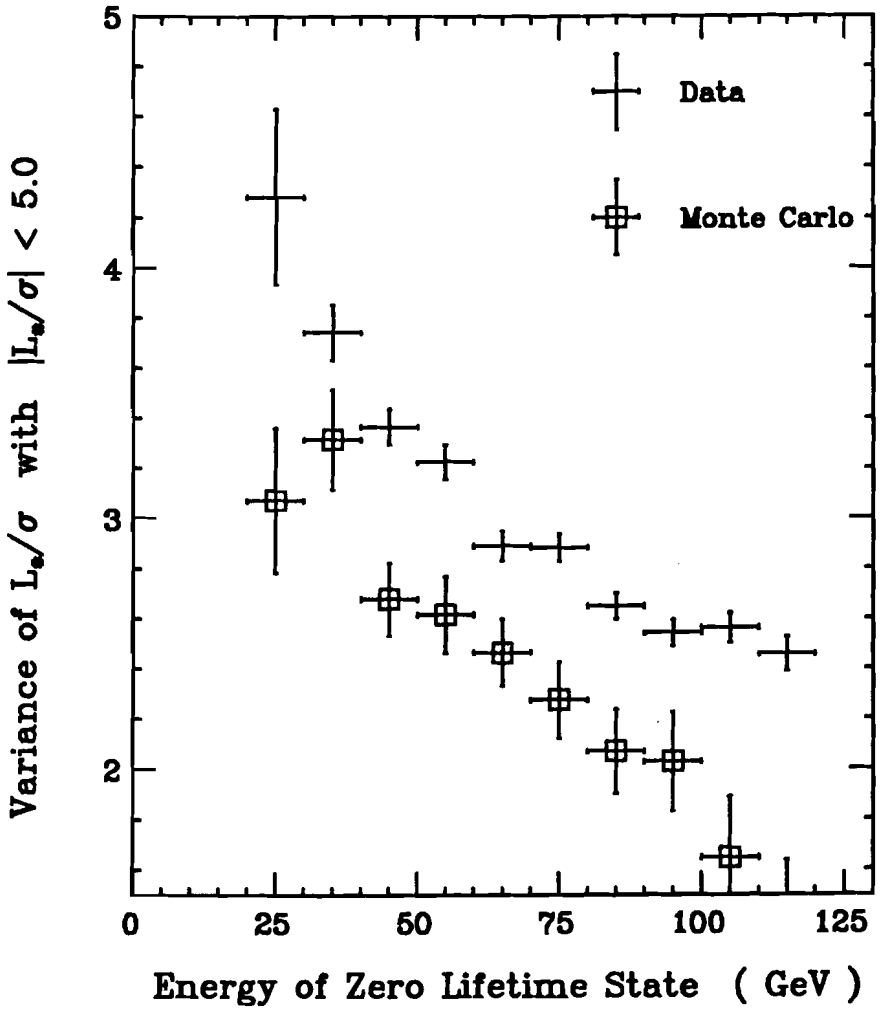
Data
Monte Carlo
Variance of L_e/σ with $|L_e/\sigma| < 5.0$
Energy of Zero Lifetime State (GeV)
0
25
50
75
100
125
2
3
4
5

Figure 4.8

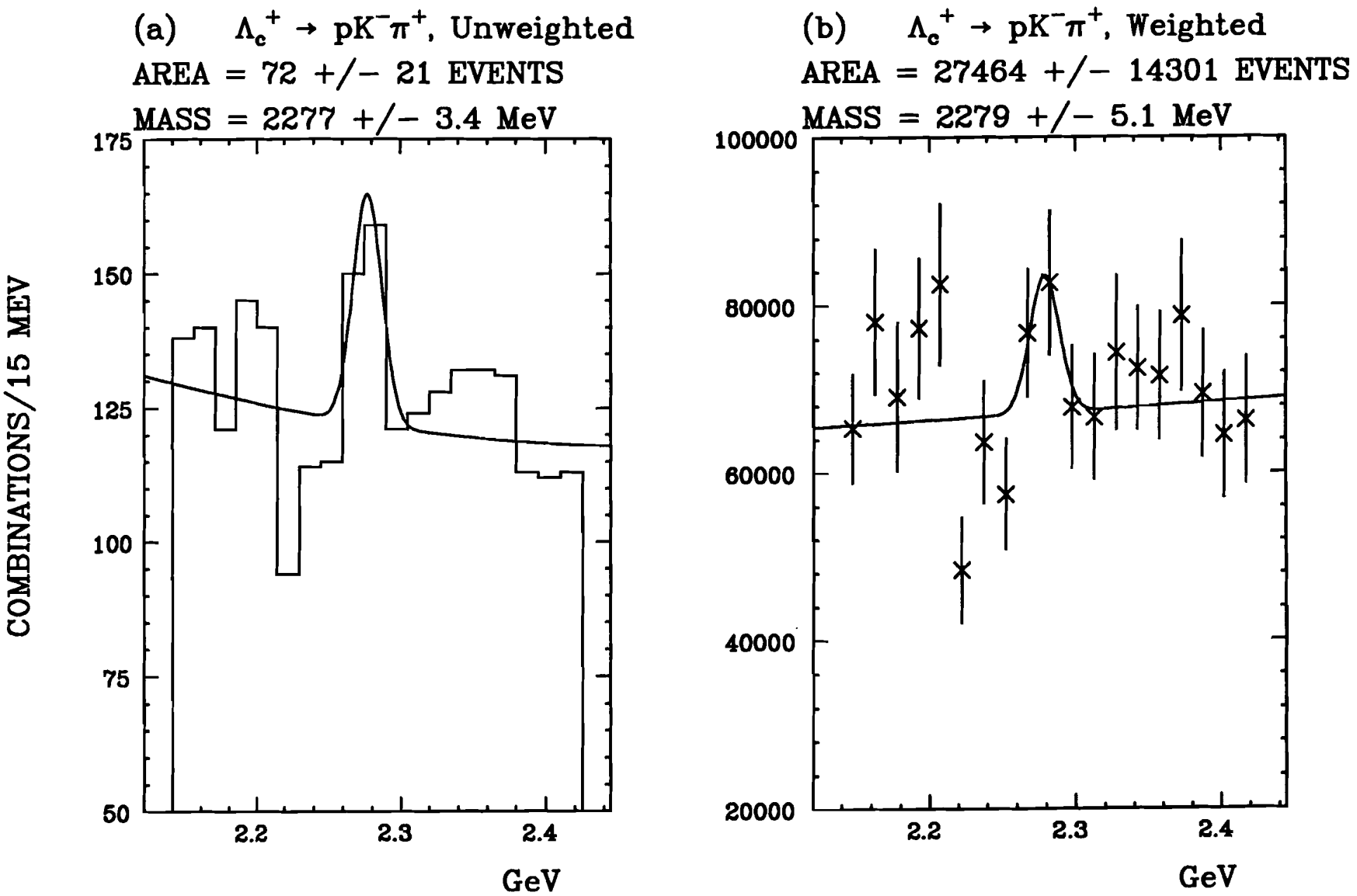

Figure 4.9 Λ_c^+ signal with final state energies of 50 to 140 GeV.

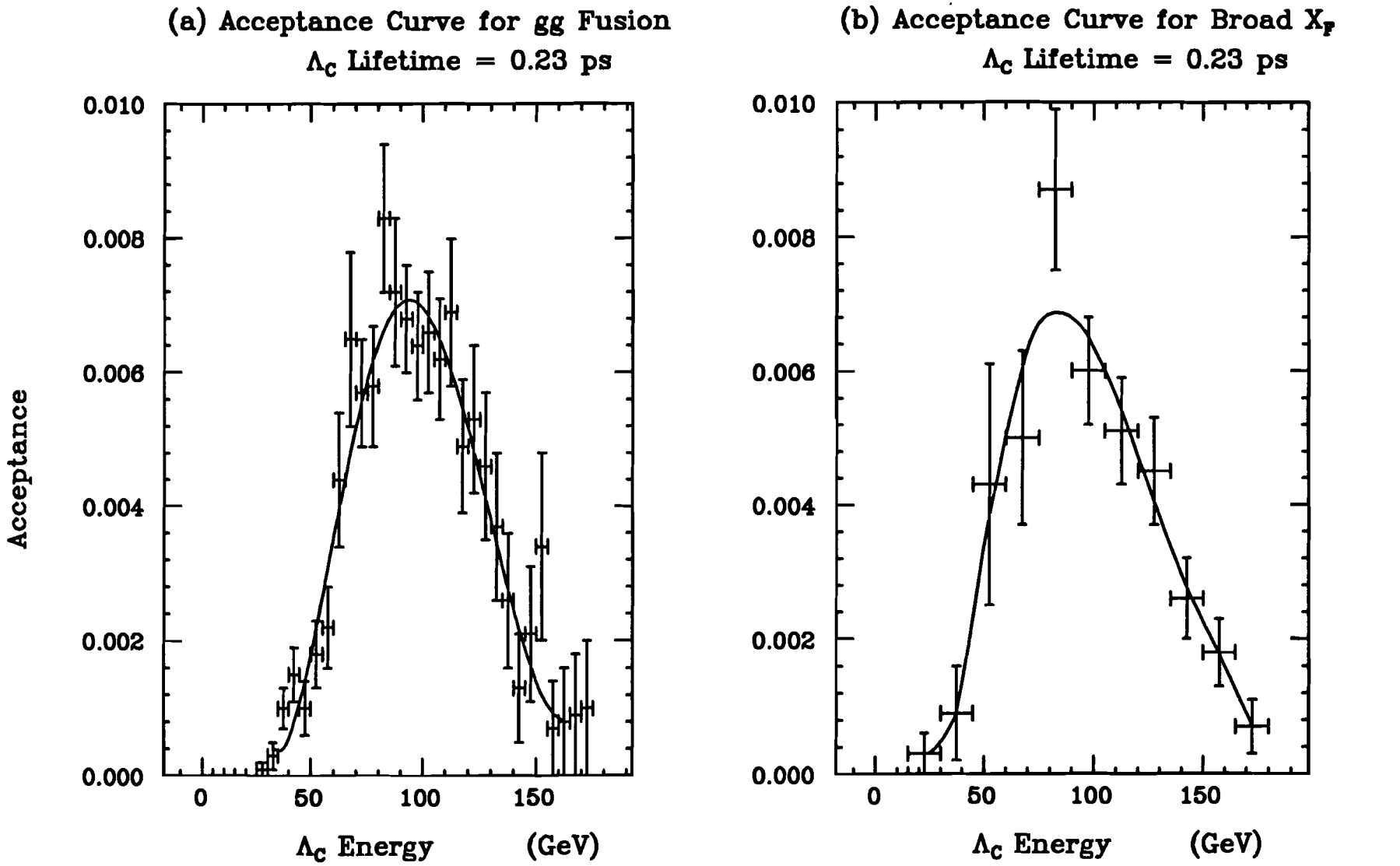
(a) Acceptance Curve for gg Fusion
Λ_c Lifetime = 0.23 ps
(b) Acceptance Curve for Broad X_F
Λ_c Lifetime = 0.23 ps
Acceptance
0.010
0.008
0.006
0.004
0.002
0.000
0
50
100
150
Λ_c Energy (GeV)

Figure 4.10

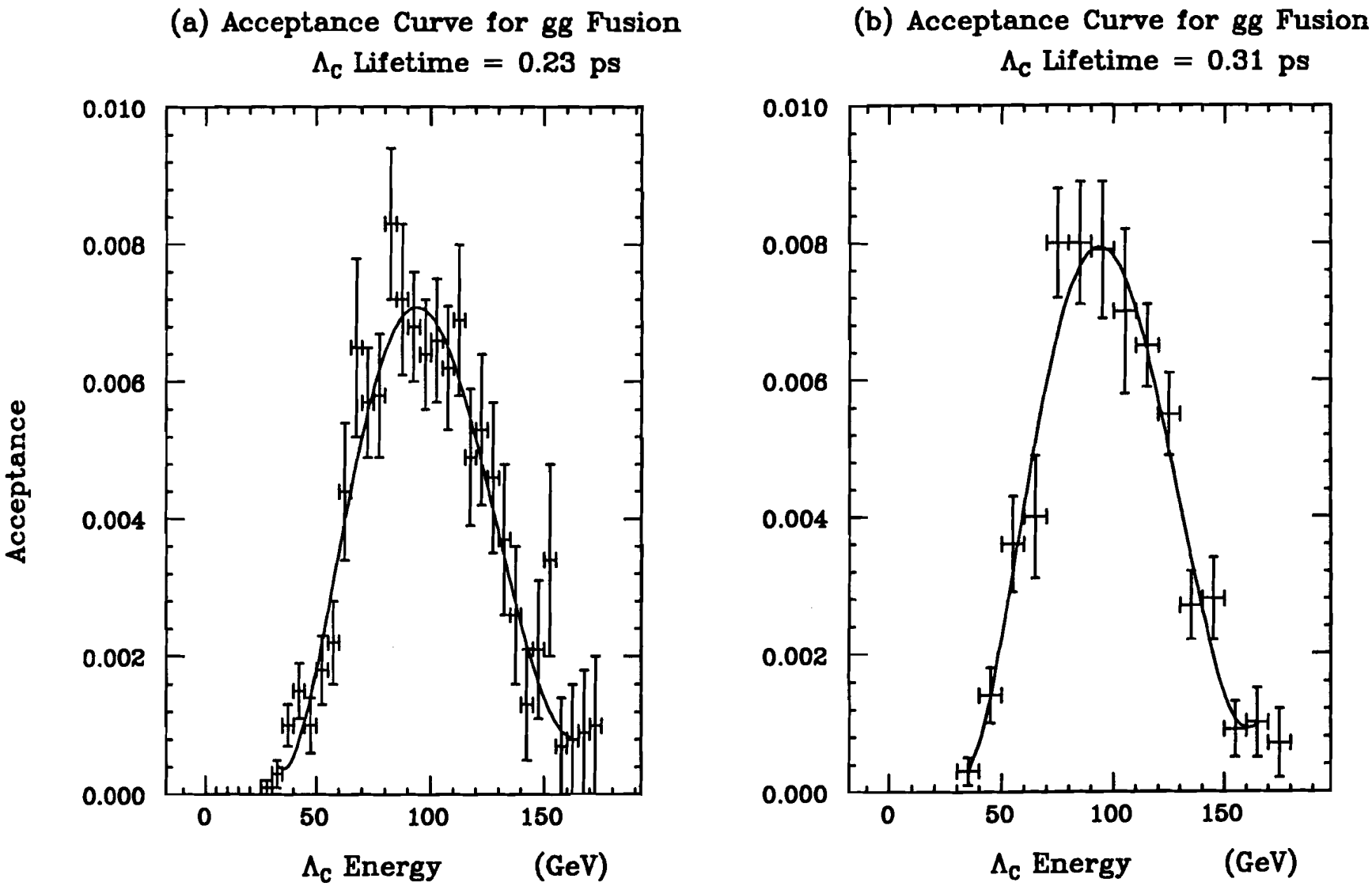
(a) Acceptance Curve for gg Fusion
Λ_c Lifetime = 0.23 ps
(b) Acceptance Curve for gg Fusion
Λ_c Lifetime = 0.31 ps
Acceptance
0.010
0.008
0.006
0.004
0.002
0.000
0
50
100
150
Λ_c Energy (GeV)

Figure 4.11

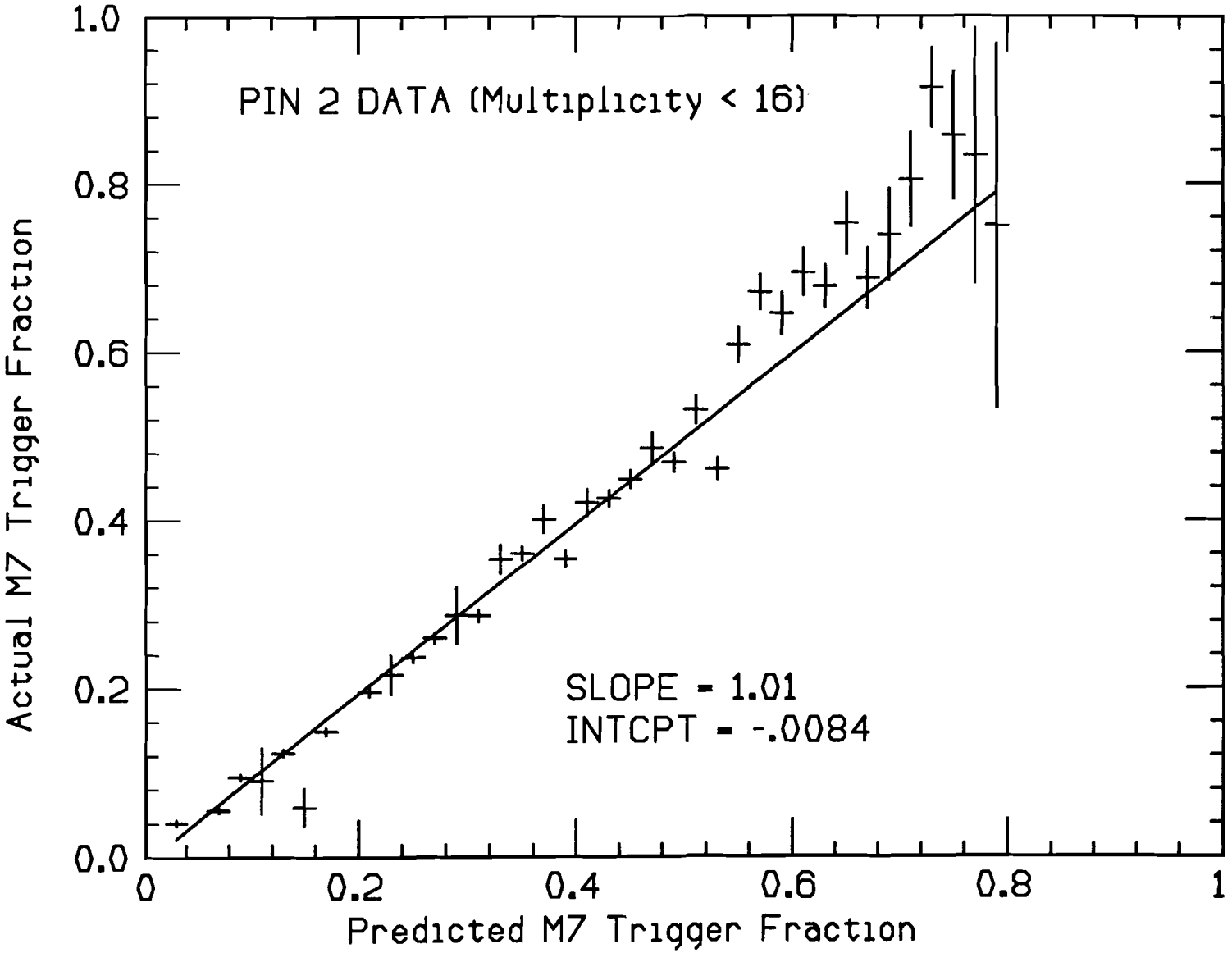
PIN 2 DATA (Multiplicity < 16)
SLOPE = 1.01
INTCPT = -.0084
Actual M7 Trigger Fraction
Predicted M7 Trigger Fraction
0.0
0.2
0.4
0.6
0.8
1.0
0
0.2
0.4
0.6
0.8
1

Figure 4.12

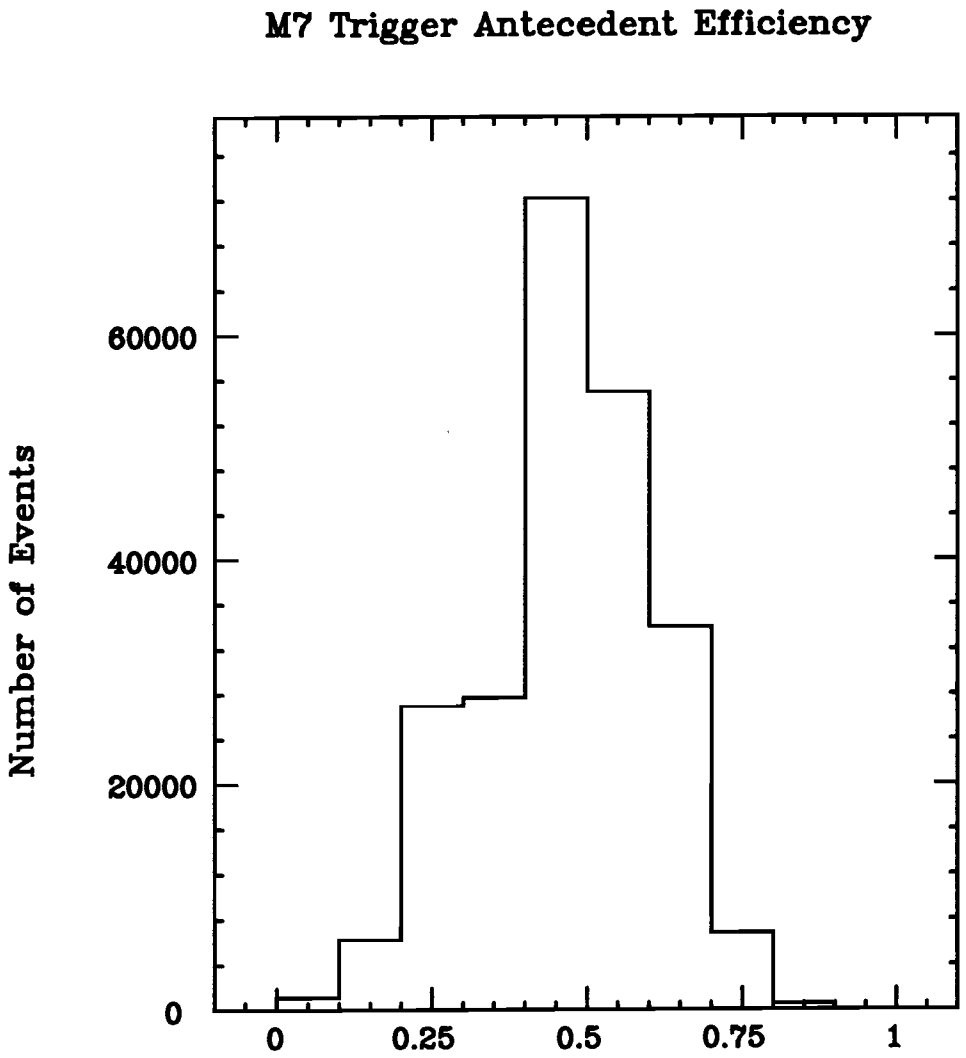
M7 Trigger Antecedent Efficiency
Number of Events
60000
40000
20000
0
0
0.25
0.5
0.75
1

Figure 4.13

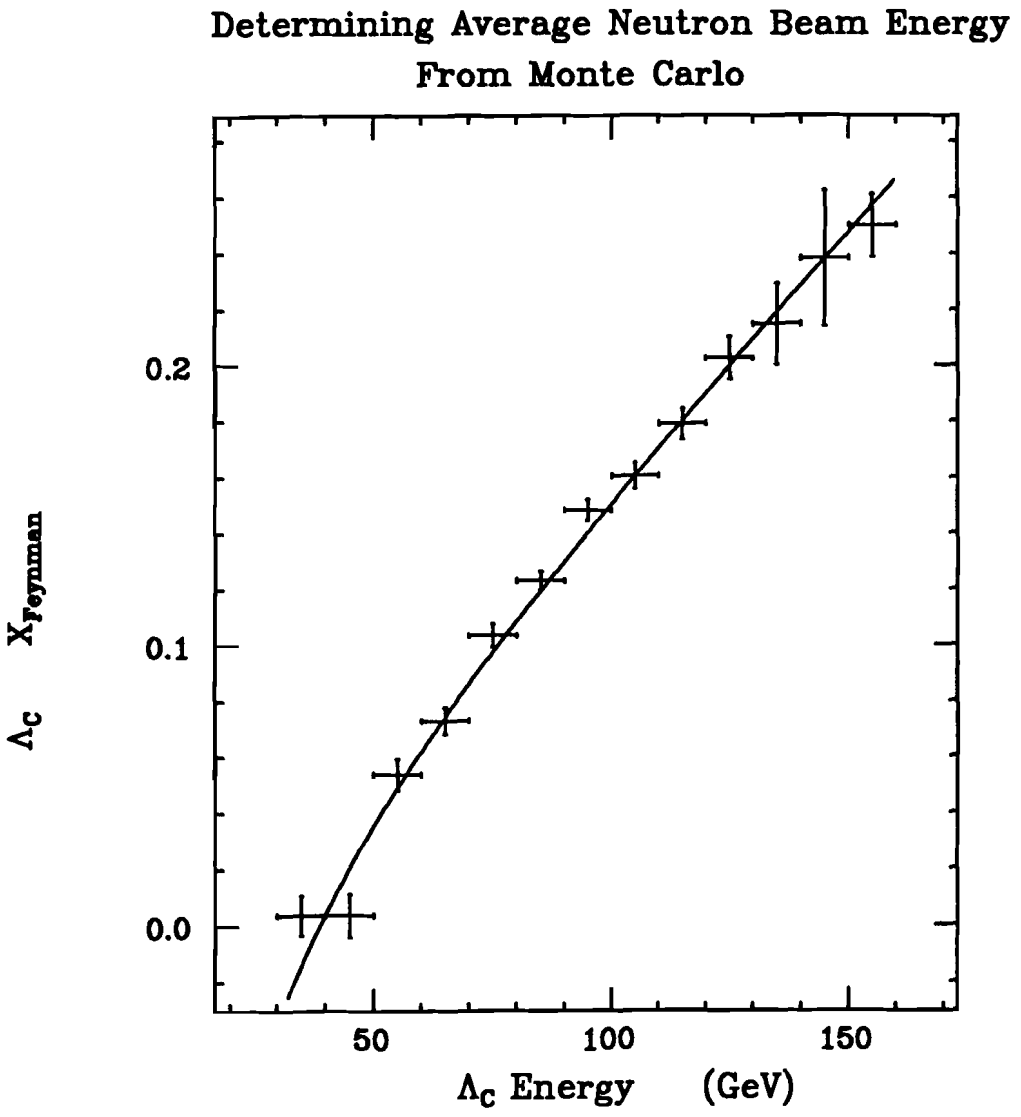
Determining Average Neutron Beam Energy
From Monte Carlo
Λ_c $X_{Feynman}$
0.2
0.1
0.0
50
100
150
Λ_c Energy (GeV)

Figure 4.14

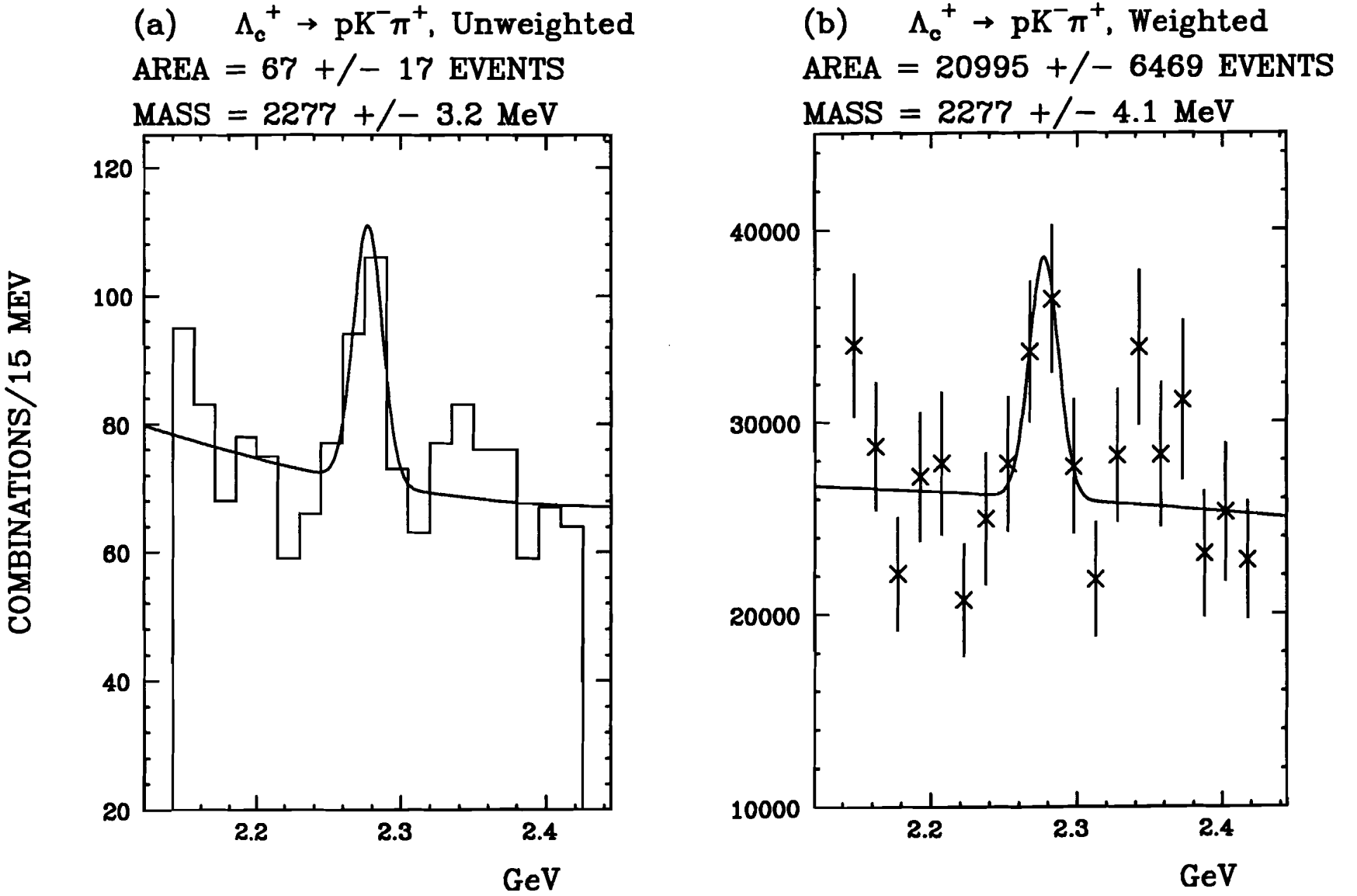

Figure 4.15 Λ_c^+ signal with final state energies of 70 to 120 GeV.

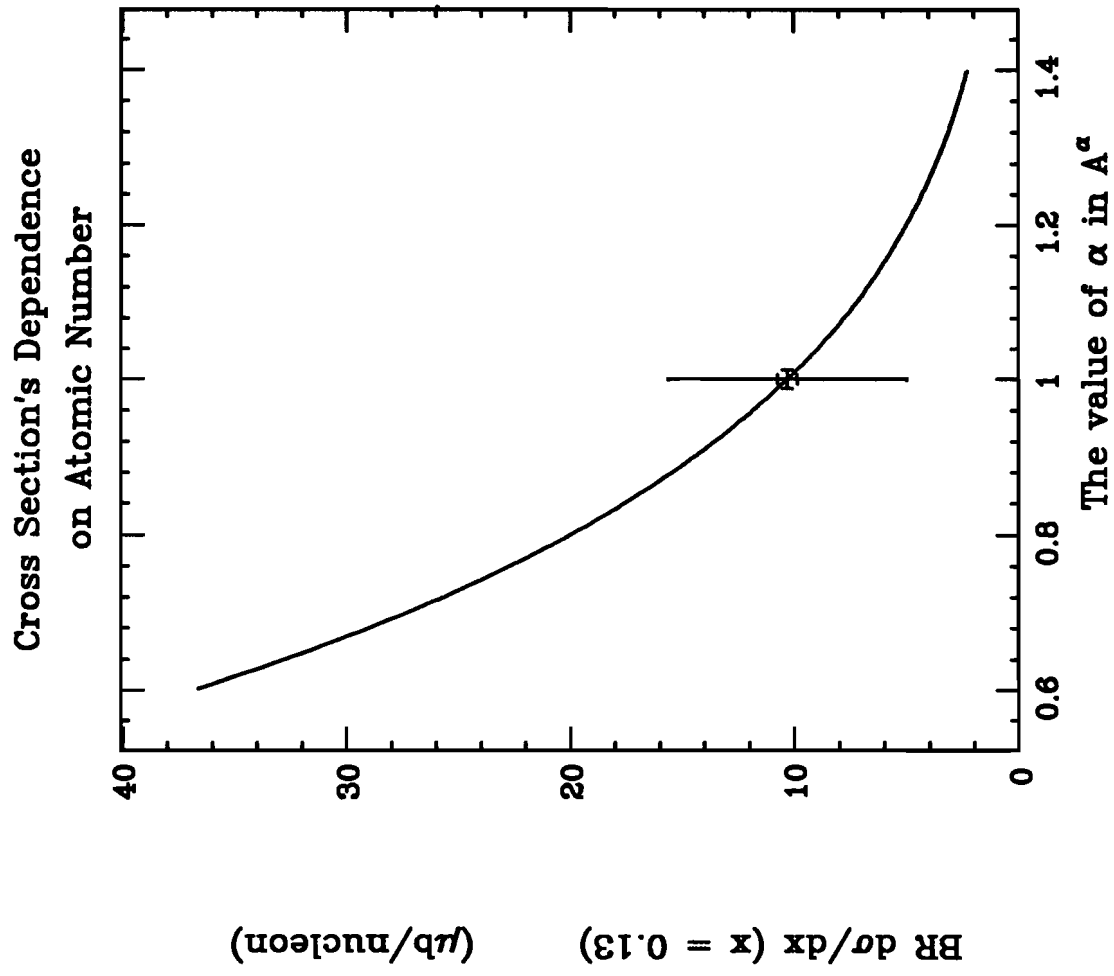
Cross Section's Dependence
on Atomic Number
BR dσ/dx (x = 0.13)
(μb/nucleon)
40
30
20
10
0
0.6
0.8
1
1.2
1.4
The value of α in A^α

Figure 4.16

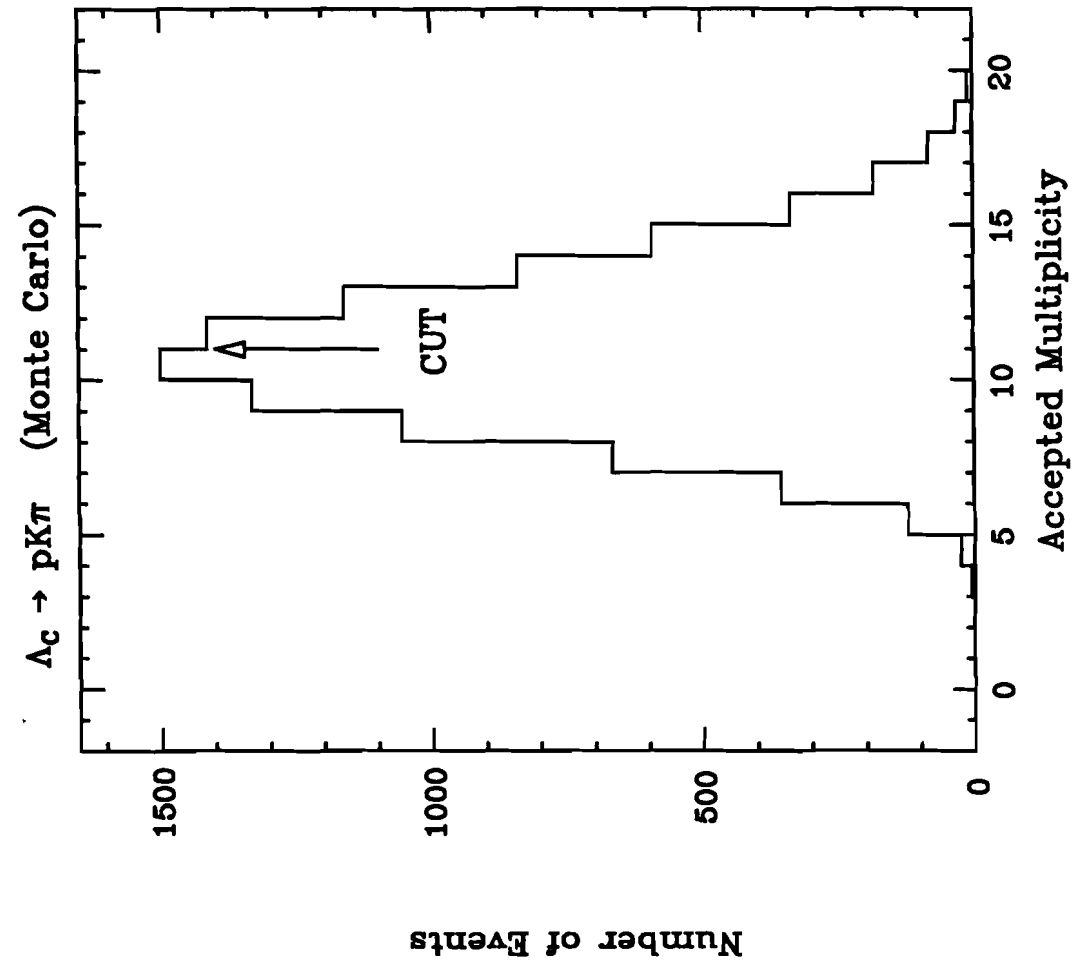
$\Lambda_c \rightarrow pK\pi$ (Monte Carlo)
CUT
Number of Events
Accepted Multiplicity
0
500
1000
1500
0
5
10
15
20

Figure 4.17

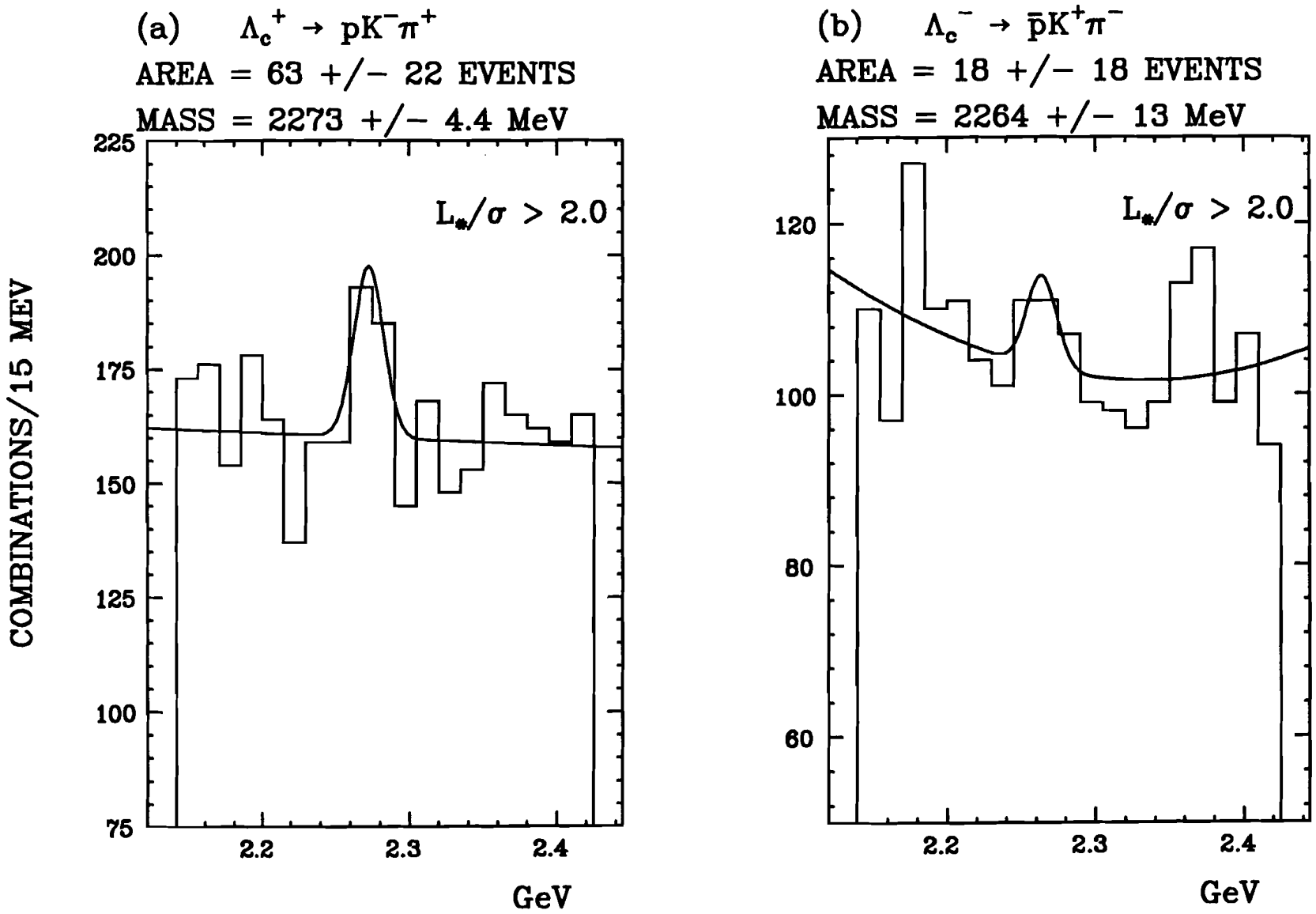
(a) $\Lambda_c^+ \rightarrow pK^-\pi^+$
AREA = 63 +/− 22 EVENTS
MASS = 2273 +/− 4.4 MeV
$L_*/\sigma > 2.0$
COMBINATIONS/15 MEV
225
200
175
150
125
100
75
2.2
2.3
2.4
GeV
(b) $\Lambda_c^- \rightarrow \bar{p}K^+\pi^-$
AREA = 18 +/− 18 EVENTS
MASS = 2264 +/− 13 MeV
$L_*/\sigma > 2.0$
120
100
80
60
2.2
2.3
2.4
GeV

Figure 4.18

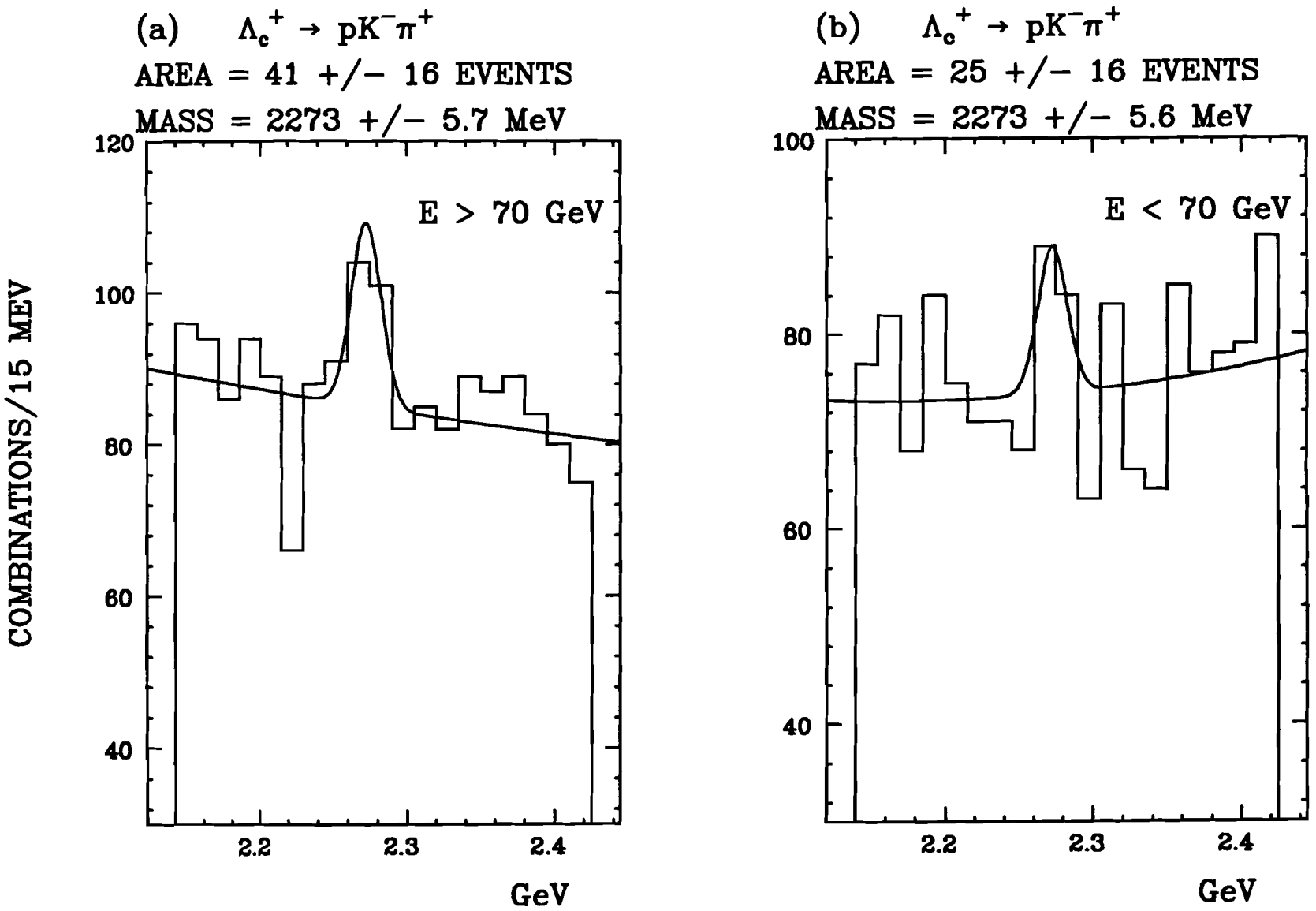

Figure 4.19 Λ_c^+ signal with $L_*/\sigma > 2$.

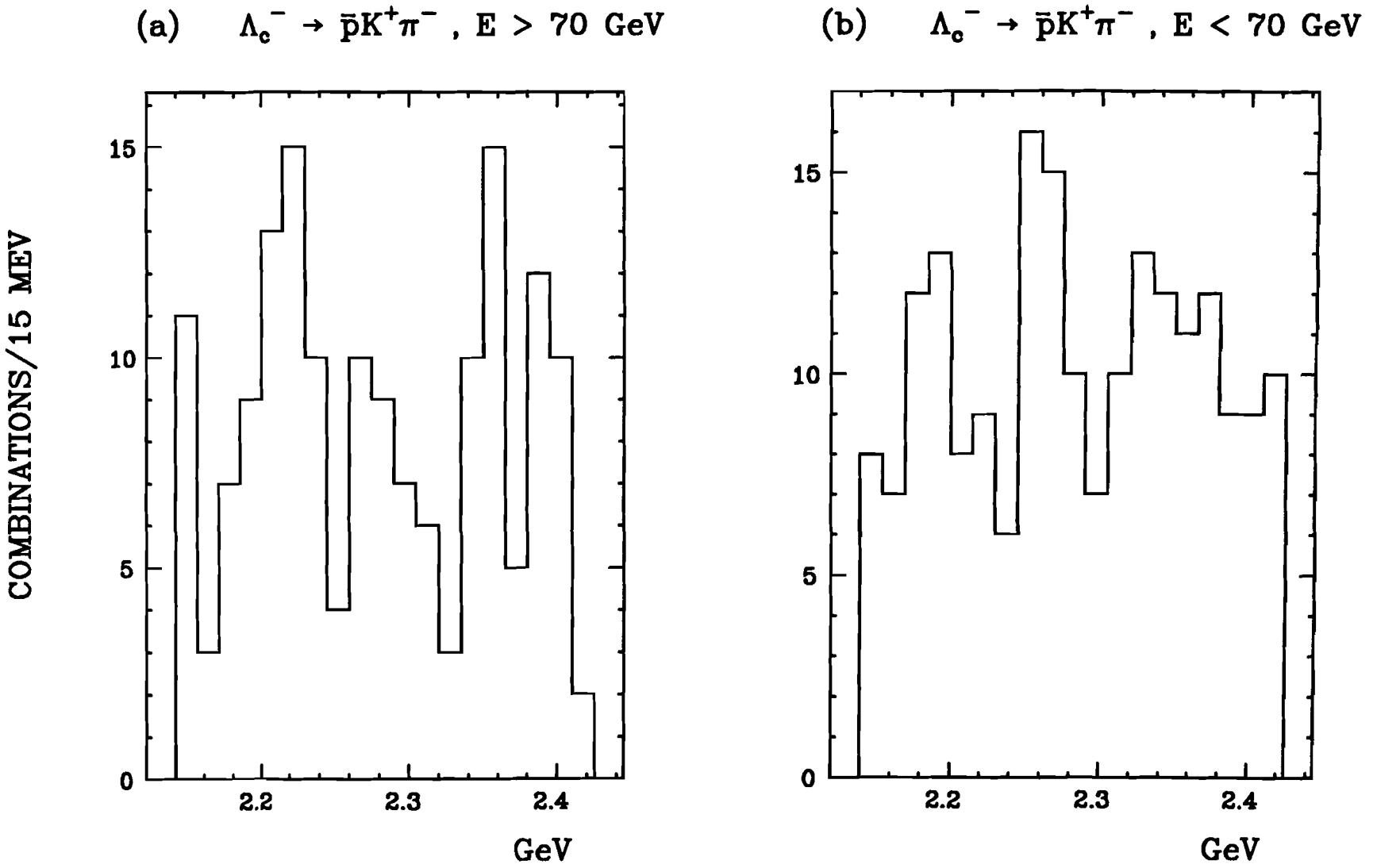
(a) $\Lambda_c^- \to \bar{p}K^+\pi^-$, E > 70 GeV
(b) $\Lambda_c^- \to \bar{p}K^+\pi^-$, E < 70 GeV
COMBINATIONS/15 MEV
0
5
10
15
2.2
2.3
2.4
GeV

Figure 4.20

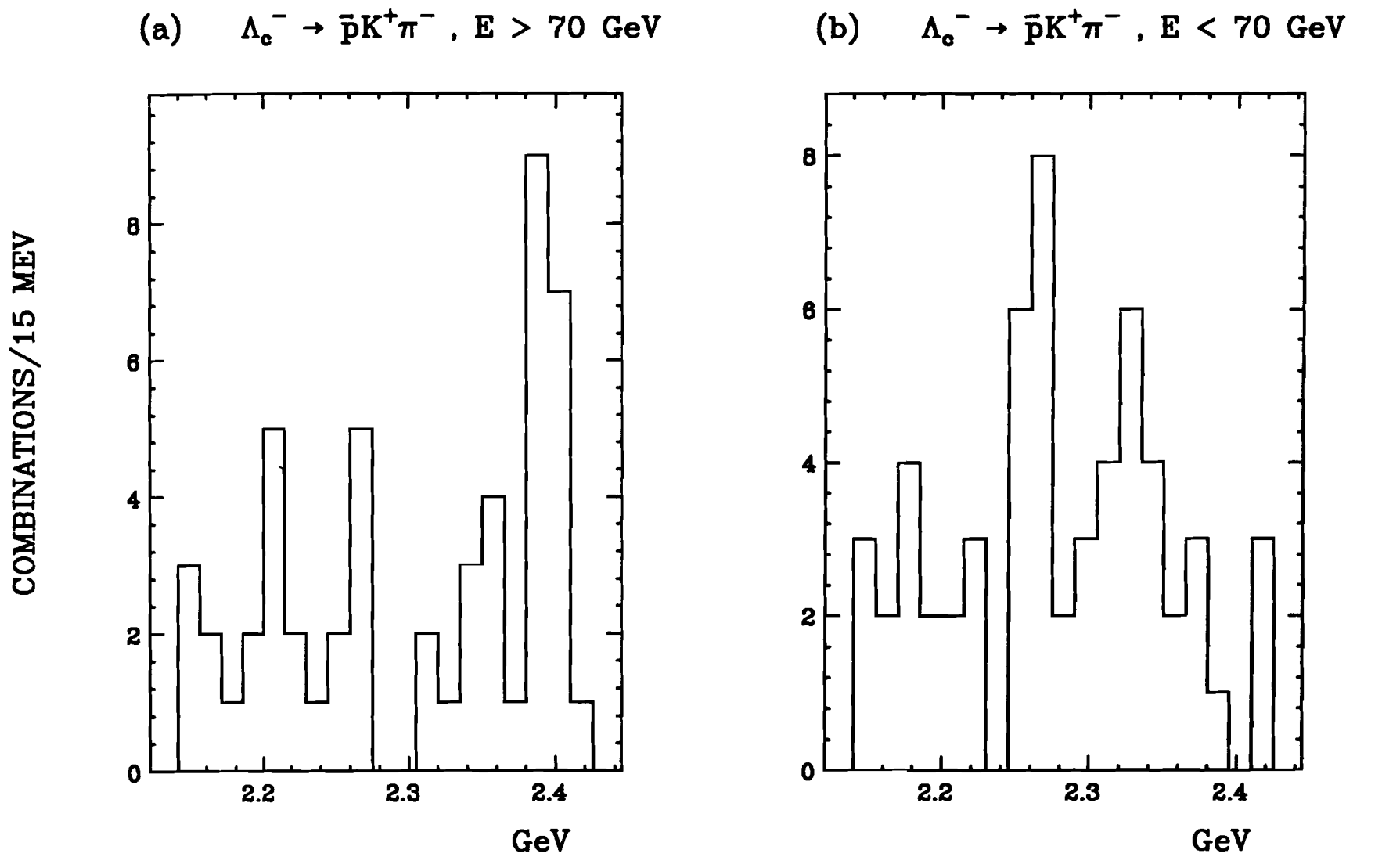

Figure 4.21 Λ_c^- signal with $L_*/\sigma > 6$.

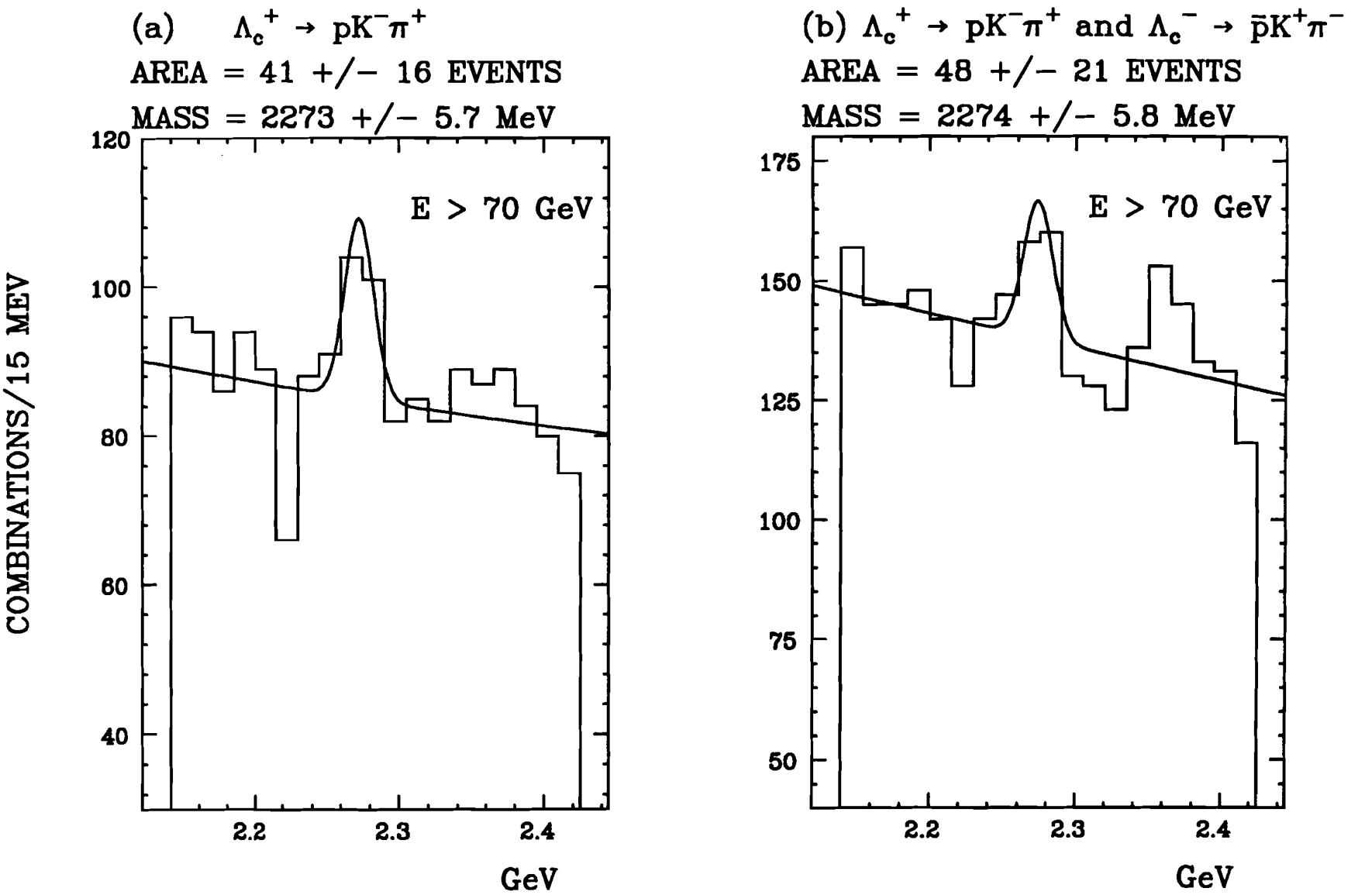

Figure 4.22 Λ_c signal with $L_*/\sigma > 2$.

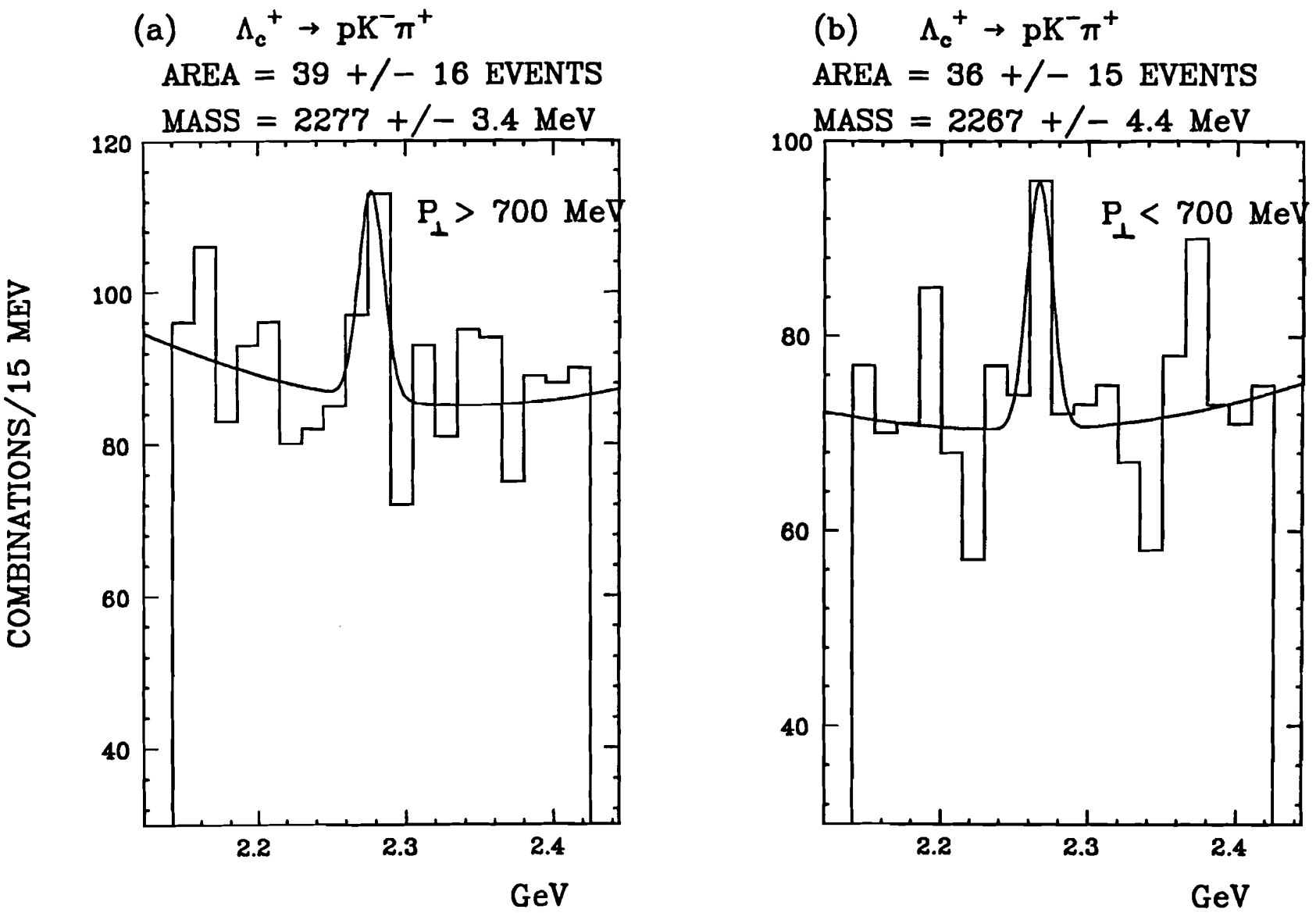

Figure 4.23 Λ_c^+ signal with $L_*/\sigma > 2$.

CHAPTER 5

Conclusions

This final chapter gives a short summary of the results on the production of inclusive Λ_c's from FNAL Experiment 400 and compares these results with those from other charm hadroproduction experiments. The Λ_c state is observed at the 5σ level when lifetime analysis cuts are applied on appropriately charged pKπ combinations. These lifetime cuts are consistent with the world average Λ_c lifetime of 0.23 ps. The results from E400 can be summarized as follows:

1. Cross section estimates of the inclusive production of Λ_c were measured in the central region of Feynman x. A value for σ (n-nucleus $\rightarrow \Lambda_c^+ X) \cdot BR(\Lambda_c^+ \rightarrow pK^-\pi^+)$ measured over the x_f range of 0.028 to 0.226 is given as 2.1 $\pm$ 1.1 ($\pm$0.74) μb/nucleon for an average neutron beam energy of 565 GeV ($\sqrt{s}$ = 33 GeV). A relatively model independent value of $BR \cdot \frac{\partial \sigma}{\partial x}(x_f = 0.13)$ gives 10.3 $\pm$ 5.3 ($\pm$3.6)μb/nucleon. Additional cross section estimates are listed in Table 4.3.

2. The signal is dominated by Λ_c^+ , where the fraction of observed Λ_c^+ 's is about 78% $\pm$ 18%. The final state energies of Λ_c^+ appear to be greater than those of Λ_c^- , but the difference is not statistically significant. Also the final state Λ_c^+ has a mean $P_\perp$ at about 700 MeV with 52% $\pm$ 15% of the Λ_c^+ signal above 700 MeV.

A summary of charm cross section results from various hadroproduction experiments is given in Table 5.1 (two pages). Additional information on these experiments can be found in published experimental summaries[9,12]. Also specific references (to update the summaries) are provided for many entries in the table. This table is not intended to be complete but attempts to give a fair representation of the available information which is most relevant for the comparisons presented below. The cross sections are listed in μb per nucleon, and the charm cross section calculations

assumed linear A dependence. Many of these calculations were based on model dependent extrapolations over the full x_f range unless stated otherwise. No correlation was assumed between the charmed and anti-charmed states being produced. Where possible, the current reported branching ratio values (as given by the Particle Data Group[5]) were used. Notice that several of the experiments listed used a meson beam as opposed to a baryon beam. Also notice that a number of experiments measure charm cross sections without plotting invariant masses. For example, beam dump experiments frequently look for single, high $P_\perp$, "prompt" leptons (i.e., leptons not originating from long-lived particle decays) as an indication of charm. Also, bubble chamber experiments look for secondary vertices with specific topologies to "flag" charm events.

In E400, the inclusive Λ_c cross section result (given above) is rather unique, and thus experimental comparisons must be done with care. E400 has a unique beam, target configuration, and energy. Also E400 is unique in that it has a very open trigger as opposed to experiments which trigger on "prompt" leptons or experiments which trigger on diffractive events. This open trigger tends to minimize any production model bias. With regards to Λ_c production, no experiment near E400's energy reports an inclusive Λ_c cross section. Also, only one other experiment (SFM - ACCDHW[18]) presents a Λ_c cross section in the central x_f region, but this signal was observed in association with a "prompt" lepton (to catch electrons from weak decays of D's).

As mentioned in Chapter 1, there appears to be a tremendous rise in the charm cross section as the center of mass energy increases from roughly 25 GeV to 60 GeV with the latter energies found at CERN - ISR. To examine where E400 enters in this scheme, the branching ratio[5] for $\Lambda_c^+ \rightarrow pK^-\pi^+$ is taken to be 2.2%. Using the differential cross section (evaluated at $x_f = 0.13$), a relatively model independent

value can be expressed as

$$\frac{\partial\sigma}{\partial x}(x_f = 0.13) \simeq 470 \pm 240\ (\pm 290)\mu\text{b/nucleon}$$

for an effective $\sqrt{s}$ of 33 GeV. Note that the systematic error now includes the error in the $\Lambda_c^+ \rightarrow pK^-\pi^+$ branching ratio ($\pm$ 50%) as well as the systematic errors described earlier in Chapter 4. However, most experiments do not report differential cross sections evaluated at a specific value of x_f. Instead the cross section is frequently evaluated over the range of x_f acceptance, and so, using the $\sigma \cdot BR$ value given at the beginning of this section leads to:

$$\Delta\sigma_{\Lambda_c^+} = 96 \pm 50(\pm 60)\mu\text{b/nucleon} \quad \text{for } 0.028 < x_f < 0.226 \text{ only.}$$

Alternatively, $\sigma \cdot BR$ may be evaluated over the full range of x_f frequently introducing a strong model dependence. To make comparisons with these values, a model assumption must be made, say for example, $\frac{\partial\sigma}{\partial x} \propto (1 - \mid x \mid)^4$, then the total inclusive Λ_c^+ cross section can be estimated to be

$$\sigma_{tot}\ (\text{n-nucleus} \rightarrow \Lambda_c X) \simeq 380 \pm 160(\pm 230)\ \mu\text{b/nucleon} \quad \text{at } \sqrt{s} \simeq 33\text{GeV}$$

where the the $\sigma_{tot} \cdot BR$ value used in the above calculation was the average value (with $N = 4$) found in Table 4.3. This value appears to be considerably larger than the cross sections presented in Table 5.1 for energies just below E400's c.m. energy. Even one recent charm cross section estimate from a bubble chamber experiment[37] (LEBC - MPS, E743) which ran at FNAL Tevatron energies (with c.m. energy just **above** E400's energy) reveals a cross section estimate of only $59^{+29}_{-15}\mu$b; however, this cross section is given for inclusive $D/\bar{D}$ production (i.e., the sum of inclusive D production and inclusive $\bar{D}$ production). LEBC - MPS (E743) has not yet reported an inclusive Λ_c cross section. D mesons are considerably easier to identify than

Λ_c 's in many experiments because of their much longer lifetime. Information on the hadroproduction of Λ_c's is very limited. In fact, other than the ISR results, only the ACCMOR collaboration[39], the BIS-2 collaboration (at Serpukhov)[40] and E400 have measured inclusive Λ_c cross sections. The ACCMOR collaboration estimates the $\Lambda_c^+\bar{D}$ inclusive cross section to be about 75 $\pm$ 50 μb. The $\bar{D}$ meson is flagged by a "prompt" electron (which is demanded in their trigger). This cross section does not include the baryon-antibaryon contribution to the inclusive Λ_c^+ cross section. Furthermore, ACCMOR's c.m. energy (of 17.5 GeV) is about half the c.m. energy used in E400. The BIS-2 collaboration gives $\sigma(\Lambda_c^+X) = 40 \pm 10\mu$b for linear A dependence in neutron carbon collisions at an average $\sqrt{s}$ of 10.5 GeV. Both ACCMOR and BIS-2 have acceptance in the forward x_f region only, but the above quoted cross sections are over the full x_f range (see Table 5.1). For completeness sake, one other experimental results on Λ_c^+ production should be mentioned. A 1983 result from LEBC-EHS[36] at $\sqrt{s} = 26$ GeV estimated the inclusive cross section of $\Lambda_c^+\bar{D}$ to be $\approx$ 20 μb (over the full x_f range); however, Λ_c^+'s were not directly observed - instead this estimate is based on the fact that more $\bar{D}$'s were seen than D's in a low statistics bubble chamber experiment.

A number of ISR experiments (with c.m. energies nearly doubled that of E400) report Λ_c cross sections at about the same value as E400 or at about 2 or 3 times larger, but again, some of these results (as listed in part B of Table 5.1) are stated as $\Lambda_c^+\bar{D}$ inclusive cross sections omitting the baryon -antibaryon contribution to the inclusive Λ_c^+ cross section.

To summarize, E400's value for the inclusive Λ_c^+ cross section may be consistent with the available experimental results on the Λ_c production rate (see Fig. 5.1). However, this consistency is somewhat misleading because different x_f acceptance

regions were applied and different production models were assumed. The results from ACCMOR, BIS-2, and most of the results from ISR are based on detectors (and triggers) which have acceptance at large x_f whereas E400 has acceptance in the central x_f region. ACCMOR, BIS-2 and the ISR results just described assumed a model where Λ_c^+ 's are produced such that $\frac{\partial\sigma}{\partial x}$ is constant or approximately of the form $(1- \mid x \mid)$ which is considerably broader than the x_f distribution assumed in the calculation of the Λ_c^+ cross section presented above (for E400). If the ACCMOR, BIS-2 or ISR data is interpreted assuming a model with x_f peaking towards zero (as done in E400), then their cross section would increase rather dramatically. Using the ISR results, for example, the increase could be a factor of 5 or so[12]. Conversely, assuming a flat x_f distribution would increase the Λ_c^+ cross section presented here significantly (– by a factor of 3, with $N = 0$, for example). Note that the popular gg fusion models[6] give rise to x_f distributions which peak towards zero.

The large cross section measured by the ISR experiments are controversial[12,19]. Among the expressed concerns is that the ISR detector acceptances have large uncertainties that are a consequence of a lack of information on $c\bar{c}$ production kinematics. Furthermore, the application of numerous analysis "cuts" tends to bias the selection of events towards mass distributions showing the most significant signals. Also, several Split Field Magnet (SFM at ISR) experiments had mass calibration problems; for example, the Λ_c mass in one experiment[18] was measured to be about 50 MeV above the current average. Finally the e^-/π^- ratios measured at the ISR suggest that charm cross sections may be a factor of two lower than those obtained from their mass distributions.

As explained in Chapter 1, an accurate theoretical picture of the results from hadroproduction of open charmed states does not exist. The gg fusion model can

appropriately account for the production of closed charm (such as ψ's), but underestimates the production rate of open charm[6,7,9]. Two aspects of open charm hadroproduction are addressed here. First, a dominance of Λ_c^+ signal over Λ_c^- signal appears in experiments using baryon beams (as measured in ACCMOR, BIS-2, ISR and E400 experiments). This observation can be explained as a hadronization process that allows for the produced c quarks to recombine with valence quarks in the beam to give a forward charmed baryon (- see the discussion on the Recombination Model and the Spectator Model in Chapter 1). Since the beams (whether protons (uud) or neutrons (udd)) do not contain valence antiquarks, the production of charmed antibaryons may be suppressed (i.e., the generated $\bar{c}$ quarks are more likely to pick-up single quarks from the general quark-antiquark sea to give anticharmed mesons). This asymmetry is also seen in the production of neutral strange baryons (i.e., Λ's) when baryon beams are used[20]. However, the theory expects the valence quark effects to be suppressed for the production of charmed states since the slow moving (relatively massive) charm quark must wind up carrying a large fraction of the beam momentum. Production rates for Λ_c^+ in the above experiments do not indicate suppression. Incidentally, a similar asymmetric production has been observed for charmed mesons by experiments using meson beams (CCFRS and LEBC-EHS[36]).

Another aspect of open charm hadroproduction which must be explained by the theorists is the dramatic rise in charm cross sections as $\sqrt{s}$ increases. Not only does the gg fusion model tend to underestimates the measured charm cross sections, but the model also fails to explain the dramatic rise as $\sqrt{s}$ increases (see Fig 1.3, again). One recent result from a FNAL bubble chamber experiment (LEBC-MPS[37] which uses a proton beam) suggests a slower rise for charm cross sections in agreement with

the fusion model. They reported[37]:

$$\frac{\sigma(D/\bar{D} \text{ at } \sqrt{s} = 38.8\, GeV)}{\sigma(D/\bar{D} \text{ at } \sqrt{s} = 27.4\, GeV)} = 1.7\, ^{+0.7}_{-0.5}$$

which can be accounted for in the gg fusion model assuming a low value for the charm quark mass (at about 1.2 GeV). Although measurements on charmed meson production in E400 are not presented in this thesis, the results presented here indicate that charmed baryon cross sections obtained with baryon beams are considerably larger than those calculated in the fusion model. The cross section measured here may be consistent with experimental measurements reported at energies above and below E400. However, a consistent production model for charmed baryons can not accommodate the cross section results from this thesis as well as those obtained at other energies.

The data on open charm hadroproduction are still very puzzling, and clearly there is a need for more investigations. A better understanding of the branching ratios of charmed particle decays and the A dependence in charm cross sections would help remove some of the systematic uncertainties. Recent technological developments (such as very high resolution vertex detectors) show promise for isolating charmed particle decays and for obtaining higher statistical charmed particle samples. A clearer picture of open charm hadroproduction may help to provide new insights into the nature of parton interactions.

Table 5.1 Charm hadroproduction experiments.

A. Lepton beam dumps.

Expt.	Reaction	Final States	$\sqrt{s}$ (GeV)	x_f Region	Cross Section†(μb)	Model Dependence, $E\frac{d^3\sigma}{dp^3}$
CCFRS	π^-Fe $\rightarrow \mu X$, high p_μ	$D\bar{D}$	23.6	$x_f \geq 0.1$	$\sigma_{D\bar{D}} = 17^{+5.4}_{-3.7}$	$\sim a\cdot(1-\lvert x\rvert)^{6.3}+b\cdot(1-\lvert x\rvert)^{0.2}$ For $x > 0$ only
BEBC	pp$\rightarrow \nu X$, low p_T ν	$D\bar{D}$	27.4	$x_f \geq 0.5$	$\sigma_{D\bar{D}} = 30 \pm 10$	$\sim (1-\lvert x \rvert)^3$
CHARM	pCu$\rightarrow \nu X$, low p_T ν	$D\bar{D}$	27.4	$x_f \geq 0.5$	$\sigma_{D\bar{D}} = 19 \pm 6$	$\sim (1-\lvert x \rvert)^3$
CIT-Stanford	pFe$\rightarrow \mu X$, high p_T μ	$D\bar{D}$	27.4	$x_f \geq 0.1$	$\sigma_{D\bar{D}} = 31^{+29}_{-18}$	$\sim (1-\lvert x \rvert)^5$
CIT-Stanford	pFe$\rightarrow \mu X$, low p_T μ	$D\bar{D}$	27.4	$x_f \geq 0.$	$\sigma_{D\bar{D}} = 22 \pm 9$	Central

B. Mass peaks with lepton triggers.

Expt.	Reaction	Final States	$\sqrt{s}$ (GeV)	x_f Region	Cross Section†(μb)	Model Dependence, $\frac{\partial\sigma}{\partial x}$
ABCCMR	π^-Be $\rightarrow eX$	$D\bar{D}$	19	$x_f \geq 0.2$	$\sigma_{D\bar{D}} = 48 \pm 15$	$\sim (1-\lvert x \rvert)^{0.8}$
ACCMOR[38]	π^-Be $\rightarrow eX$	$D\bar{D}$	20	$x_f > 0.2$	$\sigma_{D\bar{D}} = 25 \pm 11$	$\sim (1-\lvert x \rvert)^{2.9}$
ACCMOR[39]	pBe $\rightarrow eX$	$\Lambda_c^+ \rightarrow K^-p\pi^+$	17.5	$x_f > 0.2$	$\sigma_{\Lambda_c^+ D} = 75 \pm 50$	For $\bar{D}$ $\sim(1-\lvert x\rvert)^{4.5}$ For Λ_c^+ $\sim(1-\lvert x\rvert)$
IFHOT	$\pi^-p \rightarrow \mu pX$	$D^\pm \rightarrow K^\pm\pi^\pm\pi^\pm$	20.2	$0<x_f<0.8$ recoil p	$\Delta\sigma_{D^+D^-} = 28 \pm 13$	Flat x, $0.25 < x < 0.55$ only
LSM[17]	pp, 30^0 e^-	$D^+\rightarrow K^-\pi^+\pi^+$ $\Lambda_c^+\rightarrow K^-p\pi^+$	62	$0.14 < x_f < 0.9$	$\sigma_{D\bar{D}}<530\pm30\%$ $\sigma_{\Lambda_c^+ D}=840\pm50\%$	For $\bar{D}$ $\sim(1-\lvert x\rvert)^3$ For Λ_c^+ $\sim$const.
SFM[18] (ACCDHW)	pp, 90^0 e^-	$D^0\rightarrow K^-\pi^+$ $\Lambda_c^+\rightarrow K^-p\pi^+$	62	$0 < x_f < 0.3$	$\sigma_{D^0 D}=400\pm60\%$ $\sigma_{\Lambda_c^+ D}=254\pm50\%$	For D or $\bar{D}$ $\sim(1-\lvert x\rvert)^3$ For Λ_c^+ $\sim$const.

† Cross sections measured in μb/nucleon, assuming linear A dependence.

Table 5.1 (continued)

C. Vertexing techniques.

Expt.	Reaction	Final States	$\sqrt{s}$ (GeV)	x_f Region	Cross Section†(μb)	Model Dependence, $\frac{\partial\sigma}{\partial x}$
BIBC	π^-Freon	$D\bar{D}$	25	$x_f > 0$	$\sigma_{D\bar{D}} = 28.2 \pm 10.5$	Central
LEBC – EHS[36]	π^-p	$D/\bar{D}$	26	$x_f > 0$	$\sigma_{D/\bar{D}} = 15.8 \pm 2.7$	$\sim a\cdot(1-\lvert x\rvert)^{7.5}+b\cdot(1-\lvert x\rvert)^{0.7}$ For $x>0$ only
LEBC–EHS[35] NA16	pp	$D/\bar{D}$	26	$x_f > 0$	$\sigma_{D/\bar{D}} = 15.5^{+8.2}_{-4.6}$	$\sim(1-\lvert x\rvert)^{3.0}$ For $x > 0$ only
LEBC–MPS[37] E743	pp	$D/\bar{D}$	38.8	$x_f > 0$	$\sigma_{D/\bar{D}} = 59^{+22}_{-15}$	$\sim(1-\lvert x\rvert)^{5.0}$ For all x

D. Mass peaks without lepton triggers.

Expt.	Reaction	Final States	$\sqrt{s}$ (GeV)	x_f Region	Cross Section†(μb)	Model Dependence, $\frac{\partial\sigma}{\partial x}$
BIS–2 Serpukhov[40]	nC	$\Lambda_c^+ \to pK^\circ\pi^+\pi^-$ $\Lambda_c^+ \to \Lambda^\circ\pi^+\pi^+\pi^-$	Ave. 10.5	$x_f > 0.5$	$\sigma_{\Lambda_c^+} = 40 \pm 10$	$\sim$ constant
E400	nW, nBe, nSi "heavy" ID	$\Lambda_c^+ \to K^-p\pi^+$	Ave. 33	$.028 < x_f < .226$	$\Delta\sigma_{\Lambda_c^+} = 96 \pm 60$	mild model dependence $.028< x <.226$ only
SFM[14] CCHK	pp, Forward K^-	$D^+ \to K^-\pi^+\pi^+$	53	$0.2 < x_f < 0.8$	$\sigma_{D^+} = 210 \pm 60\%$	$\sim$ constant
SFM[14] CCHK	pp, Forward K^-	$\Lambda_c^+ \to K^{*0}p$ $\to K^-\pi^-$	53	$0.4 < x_f < 0.8$	$\sigma_{\Lambda_c^+} = 300 \pm 50\%$	$\sim$ constant
LSM[15] ACHMNR	pp, Diffractive	$\Lambda_c^+ \to K^-p\pi^+$	63	$0.5 < x_f < 0.8$	$\Delta\sigma_{\Lambda_c^+} = 240 \pm 120$	Diffractive For $.5 < x < .8$ only
UCLA[16] Saclay	pp, Inclusive	$\Lambda_c^+ \to K^-p\pi^+$	53, 62	$0.75 < x_f < 0.9$	$\Delta\sigma_{\Lambda_c^+} = 700 \pm 50\%$	For $.75 < x < .9$ only

† Cross sections measured in μb/nucleon assuming linear A dependence.

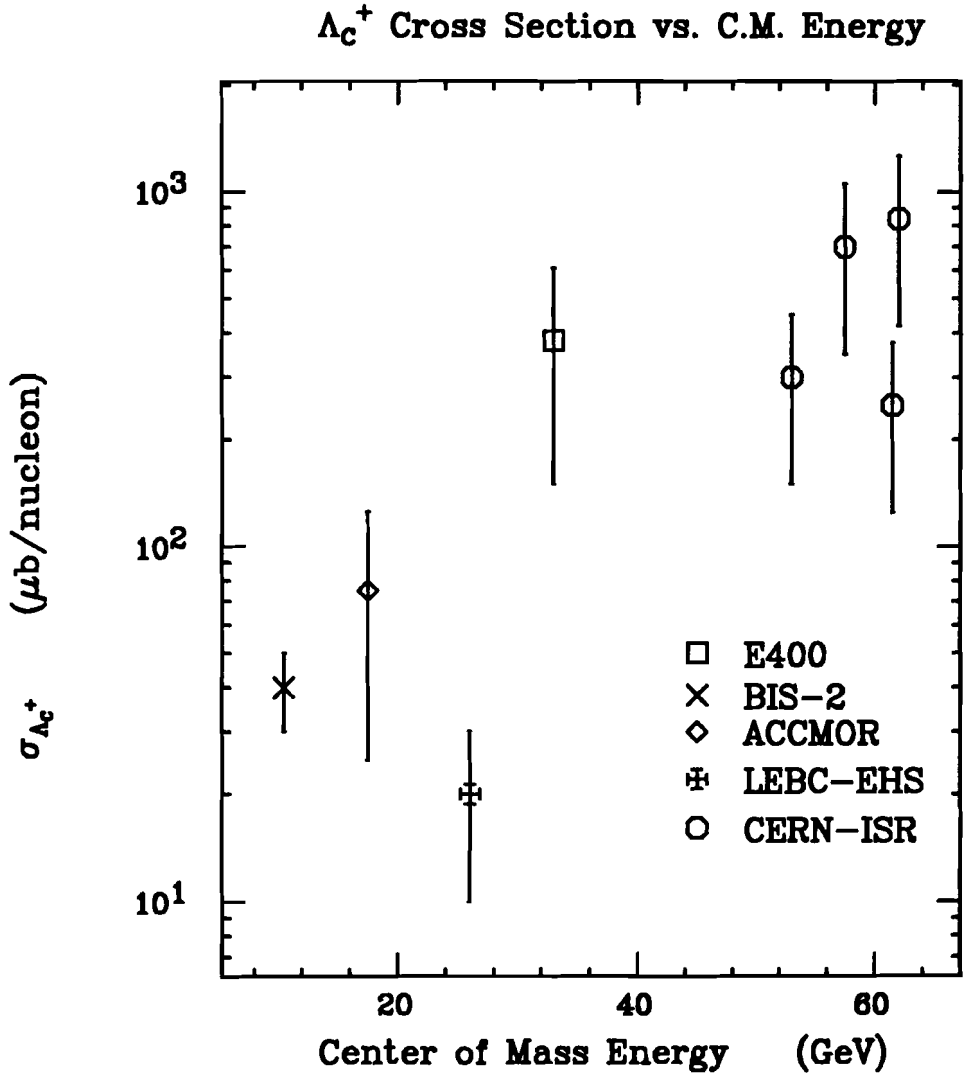
Λ_c^+ Cross Section vs. C.M. Energy
$\sigma_{\Lambda_c^+}$ (μb/nucleon)
10^3
10^2
10^1
20
40
60
Center of Mass Energy (GeV)
E400
BIS-2
ACCMOR
LEBC-EHS
CERN-ISR

Figure 5.1

APPENDIX A

The Correlated Impact Parameter Fit

Consider a charmed state decaying into n charged tracks at a distance L from the primary vertex (as measured in the lab frame). The i^{th} track emerging from the decay is predicted to have signed X and Y component impact parameters (see Fig. A.1) given by:

$$\Delta X^i = L\left[\frac{P_x^C}{P^C} - \left(\frac{P_z^C}{P^C}\right)\frac{P_x^i}{P_z^i}\right]$$

$$\Delta Y^i = L\left[\frac{P_y^C}{P^C} - \left(\frac{P_z^C}{P^C}\right)\frac{P_y^i}{P_z^i}\right]$$

where P^C is the momentum of the charmed state and P^i is the momentum of the i^{th} track. Although the exact expressions above were used in the algorithm written for the fit described below, a simple (yet approximate) form for the impact parameters is given for small opening angles as

$$\Delta X^i \simeq L \cdot \theta_x^i$$

$$\Delta Y^i \simeq L \cdot \theta_y^i$$

where θ^i is the opening angle between the i^{th} track and the charmed particle (in the lab frame).

Now, consider n tracks which may potentially be associated with the charmed state decay mentioned above. Let the measured X and Y component impact parameters be represented as ΔX_*^i and ΔY_*^i, then the best value of L (denoted as L_*) for this potential charmed state is determined by minimizing a χ^2 defined as

$$\chi^2(L) = \sum_{i=1}^{n}\left[\left(\frac{\Delta X^i(L) - \Delta X_*^i}{\sigma_x}\right)^2 + \left(\frac{\Delta Y^i(L) - \Delta Y_*^i}{\sigma_y}\right)^2\right]$$

where σ_x and σ_y are the transverse component position errors. Note, that the determination of the primary vertex was done with a fit that excluded the n tracks under consideration. The minimized χ^2 found from this fit (which can be written as $\chi^2(L_*) \equiv \chi^2_*$) must be smaller the χ^2 associated with the n tracks originating at the primary vertex, $\chi^2(L=0) \equiv \chi^2_o$. Real charmed particle decays will favor $L_* > 0$ and small χ^2_* . Since L_* is essentially proportional to the lab momentum of a charmed particle, a direct cut on L_* will introduce an unnecessary momentum dependent efficiency correction. To remove this momentum bias, one could use the proper decay length, L_*/γ, as an analysis tool to cut away background. Alternatively one could cut on the variable L_*/σ where σ is the anticipated error on the decay length L_*. Neglecting the errors on the Z of the primary vertex (which are typically 50 mills ,or about 1300 μm, as shown in Appendix B), the value of σ is given by the expression:

$$\frac{1}{\sigma} \equiv \sqrt{\sum_{i=1}^{n} \left(\frac{\theta_x^{i\,2}}{\sigma_x^2} + \frac{\theta_y^{i\,2}}{\sigma_y^2} \right)}$$

Note that for a given charmed particle decay configuration (in the charmed particle center-of-mass frame) the angles θ_x^i and θ_y^i scale as 1/P where P is the lab momentum of the charmed state. For this reason, a cut in L_*/σ is essentially equivalent to a cut in L_*/γ when one averages over all possible decay configurations, and is thus essentially momentum independent as well. The advantages of an L_*/σ cut is that the significance of the vertex detachment is correctly computed for **each** separate decay configuration as well as for the average decay configuration.

The demand that the secondary vertex for a charmed particle candidate must be significantly downstream of the primary vertex is usually accompanied with the demand that the tracks comprising a candidate converge into a reasonable secondary vertex based on χ^2_* . This cut tends to eliminate possible background vertices which include badly measured tracks, and tracks which are part of neutral V^0's. A little

algebra gives

$$\chi^2_* = \chi^2_o - \left(\frac{L_*}{\sigma}\right)^2 .$$

To improve signal to background, one can demand that χ^2_* be small and that L_*/σ be positive (since negative lifetimes are obviously dominated by background) and relatively large. This expression for χ^2_* shows that a stiff cut on L_*/σ will insure that χ^2_* is considerable smaller than χ^2_o , i.e., the tracks "prefer" originating from the secondary vertex.

For the algorithm used in this dissertation, the transverse errors for full tracks and stubs were the same. Also the X and Y component errors were equal and constant, such that $\sigma_x = \sigma_y = \sigma_{x,y} = 2.8$ mills (or 71 μm). These errors were chosen to closely match the actual measured transverse position error which was determined in Appendix B. One can use this measurement of the transverse position error to determine the anticipated resolution on the proper lifetime of the charmed state. The proper lifetime of a charmed particle decay is given by:

$$\tau = \frac{ML_*}{cP}$$

where M is the mass of the charmed state and P is its momentum. Using the expression for the error on L_* and assuming $\sigma_{x,y} = 2.8$ mills gives the result:

$$\sigma_\tau = \frac{M\sigma_{x,y}}{cP\,\Theta} \quad \text{where} \quad \Theta = \sqrt{\sum_{i=1}^{n}\left(\theta_x^{i\,2} + \theta_y^{i\,2}\right)}$$

The value of $P\ \Theta$ for a symmetric $\Lambda_c^+ \rightarrow \mathrm{pK}^-\pi^+$(where all decay particles equally share the available energy in the center of mass system) is calculated to be $P\ \Theta \approx$ 3 GeV. The E400 Monte Carlo, which incorporates the effects of geometrical acceptance and particle identification gives the result $P\ \Theta \approx 2.8$ GeV which is constant to within 5 % over the full accepted momentum region. Using this value for $P\ \Theta$ and the

known mass of the Λ_c of 2.281 GeV, we obtain a proper lifetime resolution of σ_τ = 0.19 ps, which is nearly as large as the current world average Λ_c lifetime of $\tau = 0.23$ ps.

This algorithm perhaps can be improved by investigating the exact nature of the transverse error relative to different types of tracks, component biases, and possible momentum dependences. In addition, one could incorporate the error associated with the primary vertex, which is essentially ignored by the algorithm described above.

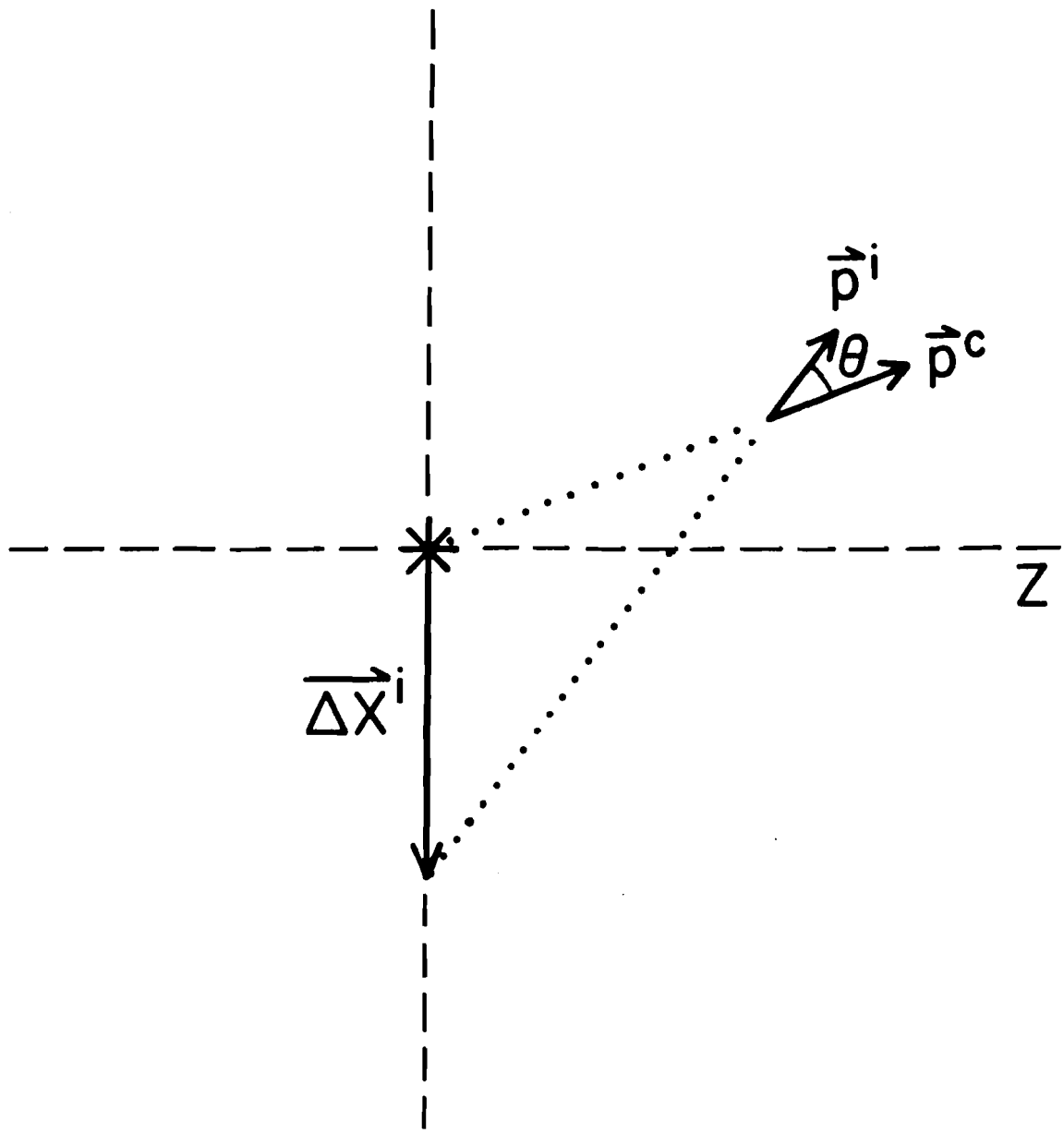

Figure A.1 The impact parameter, ΔX^i, of the i^{th} track emerging from a charm state decay.

APPENDIX B

Determination of the Transverse Position Error

The ability of the vertex chamber (also called the D5) to "tag" charmed particles by their short but finite lifetime can be characterized by the transverse position error which is the error in X or Y when a track is extrapolated to a given Z location, say the center of a given target segment. These transverse errors are identified as σ_x and σ_y. This section begins by discussing the theoretical limits on σ_x and σ_y and compares these limits to the experimental determination of σ_x and σ_y. In Appendix A these measurements are used to compute the anticipated resolution on the proper lifetime for charmed states.

It is useful to recall the following features of the E400 spectrometer when considering the anticipated transverse position errors. In the E400 spectrometer, the wire spacing of the D5 is eight times finer than the wire spacing of the chambers comprising the main spectrometer. Hence the intercept resolution is essentially the position resolution of the 9 chamber planes of the D5. Conversely, the angular information provided by the main spectrometer is better by a factor of about 8 than the angular information provided by the D5 owing to the much longer length of the main spectrometer. Hence the angular resolution of full tracks and stubs is essentially the angular resolution of the main spectrometer. These considerations lead one to consider three sources of transverse position error:

1. Error in determining intercept of the track with the D5 due to the D5 wire spacing.
2. Error due to extrapolating from the intercept of the track with the D5 center to the Z location of the primary vertex due to the main spectrometer angular error.
3. Error due to multiple coulomb scattering of the track from matter located between the D5 and the primary vertex.

For a single D5 plane with wire spacing W , the RMS error in a single coordinate is given by $\sigma = W/\sqrt{12}$. For a D5 station consisting of 3 planes oriented at 0° and ±60° , the expected X and Y errors can be shown to be $\sigma_x = \sigma_y = W/\sqrt{18}$. For three such stations one then expects:

$$\sigma_{ws} = \sigma_x = \sigma_y = W/\sqrt{54} = 1.34 \text{ mills}$$

where the D5 wire spacing is given as W = 9.85 mills (or 250μm). Multiple coulomb scattering, adjacent wire hits and confusion in the D5 will seriously degrade the performance relative to these theoretical limits.

In order to reduce the effects of extrapolation errors, the D5 was placed as close as possible to the target assembly. By considering the wire spacing and positions of the chamber stations of the main spectrometer, typical angular errors of 50 μrad and 100 μrad are computed for full tracks and stubs, respectively. The distance from the most upstream target segment (tungsten) is 7 inches. Hence the transverse error due to trajectory extrapolation from the D5 is at most expected to be 0.7 mills. Including the effects of this error increases the theoretical limit to $\sigma_x = 1.6$ mills , $\sigma_y = 1.5$ mills for stubs and a nearly negligible increase for full tracks.

Multiple coulomb scattering of a track (with momentum P) passing through the slabs of matter which constitute the target assembly and detectors contributes a momentum dependent term to the transverse position error of the form

$$\sigma_x = \sqrt{{\sigma_{ws}}^2 + \frac{C_{ms}^2}{P^2}} \quad \text{where} \quad C_{ms} = 14 \text{ MeV} \sqrt{\sum_i \left(\frac{t_i}{X_i}\right)(Z_i - Z_v)^2}$$

where t_i/X_i is the thickness of a given slab in radiation lengths, Z_i is the position of the slab, and Z_v is the position of the primary vertex. In E400, the material between

the tungsten target and the D5 results in $C_{ms} \approx 10$ mill GeV with a significant portion due to the material of the D5 itself. The effects of multiple coulomb scattering from matter downstream of the D5 will increase the value of C_{ms} but by an amount which is difficult to calculate since much of this matter is between planes of the main spectrometer. Hence much of the effect of this multiple scattering is compensated by the track fitting process.

However, an experimental measurement of the transverse extrapolation errors, σ_x and σ_y, can be made by examining the resolution on the Z of the primary vertex. The coordinates of the primary vertex are determined by minimizing the χ^2 given by the expression:

$$\chi^2 = \sum_i \frac{(x_i' Z_v + X_i - X_v)^2}{\sigma_x^2} + \frac{(y_i' Z_v + Y_i - Y_v)^2}{\sigma_y^2}$$

where the sum ranges over all tracks which are considered part of the primary vertex, x_i' and y_i' are the slopes of the i'th track (upstream of M1), and x_i and y_i are the intercepts of the track at some convenient reference plane (such as the bend center of M2). By forming $\frac{d^2\chi^2}{dZ_v^2}$ one computes that the error on Z_v ,(σ_{Z_v}) should be given by:

$$\sigma_{Z_v} = \frac{\sigma_{x,y}}{\sqrt{\sum_i \left(x_i'^2 + y_i'^2\right)}}$$

where a single error $(\sigma_{x,y})$ is assumed for all tracks and both X and Y projections.

By comparing the above primary vertex error expression to the observed Z_v distribution width, one can obtain an estimate for $\sigma_{x,y}$. The distributions for the tungsten and downstream Si triggering wafers are studied since they are extremely thin (with total lengths of 12 mills and 43 mills respectively). Monte Carlo calculations demonstrate that the effects of multiple coulomb scattering somewhat complicates the analysis of the primary vertex resolution. These calculations indicate that adding a

term in quadrature with the value of σ_{Z_v} is necessary. Including a constant in quadrature implies that the true resolution will approach this constant even as the calculated error (as given by σ_{Z_v} in the above equation) approaches zero. A probable explanation for this effect is that primary vertices which are predicted to be very well resolved must include very wide angle stubs. Since hadroproduction is typified by limited $P_\perp$, the wide angle stubs must have very low momentum and must therefore have transverse position errors dominated by multiple scattering which has a 1/P dependence. Since for a given $P_\perp$, the stub production angle also has a 1/P dependence, the contribution of a given wide angle stub in reducing σ_{Z_v} approaches an upper limit typified by C_{ms} and $< P_\perp >$.

By including an additive term in quadrature, one can successfully predict the observed error in Z_v. Figure B.1a shows the observed error in Z_v for the tungsten target. This figure compares the distribution of the normalized Z_v deviation (i.e., the deviation of Z_v from the nominal tungsten target center divided by the predicted error in the deviation) to a Gaussian distribution of unit (RMS) width shown by the solid curve. The agreement with a unit Gaussian distribution is impressive although there are non-Gaussian tails clearly visible when this data is histogrammed on a logarithmic scale as shown in Figure B.1b. The value for the predicted error (σ_{pred}) used in Figures B.1a or B.1b consists of the calculated error from the slope of the tracks in the primary vertex (as given by the previous equation) as well as a constant added in quadrature to take into account finite target thickness, multiple scattering effects, etc. The predicted width expression used was:

$$\sigma_{pred} = \sqrt{\sigma_{Z_v}^2 + (28.6 \text{ mills})^2}$$

where σ_{Z_v} was computed assuming $\sigma_{x,y} = 2.69$ mills.

The above predicted width expression was found using a constant transverse

position error ($\sigma_{x,y}$), independent of track momentum. However, a Monte Carlo study reveals that the error in Z_v can be appropriately reproduced by assuming a momentum dependent transverse position error given by:

$$\sigma_{x,y} = \sqrt{(2.13 \text{ mills})^2 + (21 \text{ mill GeV/P})^2}$$

Notice, the asymptotic resolution on $\sigma_{x,y}$ is thus roughly 30 - 40 % larger than the earlier calculated theoretical limit for the chamber assuming "perfect" data (i.e., no missing hits or adjacent wire hits).

Fig. B.1c and Fig. B.1d show the normalized deviation for the three upstream triggering Si target segments using the identical constants for σ_{pred} as found for the tungsten target. The dashed curve is a Gaussian with an RMS width of 0.82 which indicates that the primary vertices in the triggering Si target segments are slightly better resolved than vertices in the tungsten. The improved resolution in the triggering Si target is probably due to a considerably reduced multiple coulomb scattering contribution and a much shorter extrapolation distance from the D5. To summarize –the analysis of the primary vertex width for the two thin targets indicates an effective transverse position error ranging from 2.20 to 2.69 mills (or 56 to 68 μm) depending on the target segment. Incidentally, the error on the primary vertex is typically 50 mills (or 1300 μm).

An alternative method for investigating the magnitude of the transverse position error involves studying errors in the determining the secondary vertex for potential charm candidates using the correlated impact parameter fit described in APPENDIX A. To study the errors we plot L_*/σ for background candidates which presumably have no finite lifetime and hence a **background** L_*/σ plot represents nothing but resolution effects. The anticipated error in the secondary vertex is related to the transverse position error in a manner highly analogous to the error in the primary

vertex:

$$\sigma_Z = \frac{\sigma_{x,y}}{\sqrt{\sum_i \left(\theta_x^{i\,2} + \theta_y^{i\,2}\right)}} .$$

where θ_x^i , and θ_y^i are the angles of the given charm constituent track with respect to the total charmed particle momentum vector. Figure B.2a shows the normalized deviation plot for **background** $\Lambda_c \rightarrow PK\pi$ candidates with momentum exceeding 125 GeV compared to a Gaussian distribution of unit RMS width. The normalized error which was computed using Eqn. 2 with $\sigma_{x,y} = 2.8$ mills agrees very well with the unit Gaussian distribution giving additional support to this value for the effective transverse position error. Figure B.2b shows the normalized deviation plot for **background** $\Lambda_c \rightarrow PK\pi$ candidates with momentum less than 50 GeV. The solid curve is a unit RMS width Gaussian while the dashed curve has an RMS width of 1.60. Clearly the P $<$ 50 GeV candidates have a worse resolution on the secondary vertex than the P $>$ 125 GeV candidates. This broadening of the resolution presumably reflects the effects of multiple coulomb scattering as well as the effects of the typically 50 mill resolution on the location of the primary vertex which is not taken into account in the anticipated secondary vertex error.

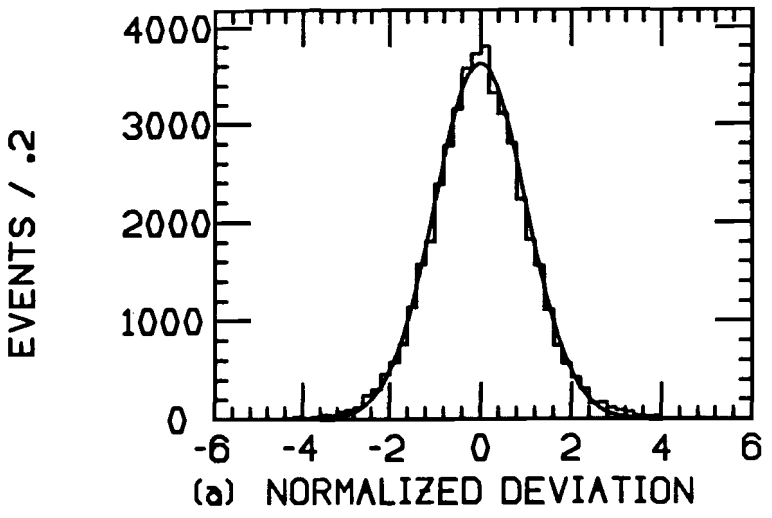
EVENTS / .2
4000
3000
2000
1000
0
-6 -4 -2 0 2 4 6
(a) NORMALIZED DEVIATION

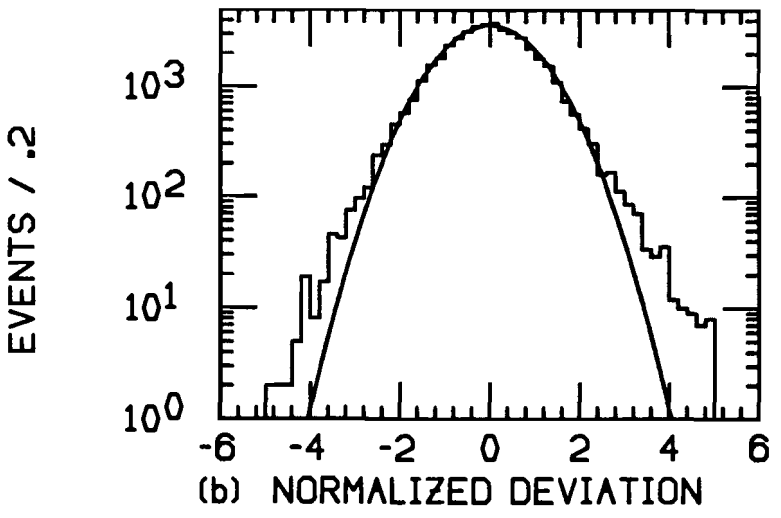
EVENTS / .2
10^3
10^2
10^1
10^0
-6 -4 -2 0 2 4 6
(b) NORMALIZED DEVIATION

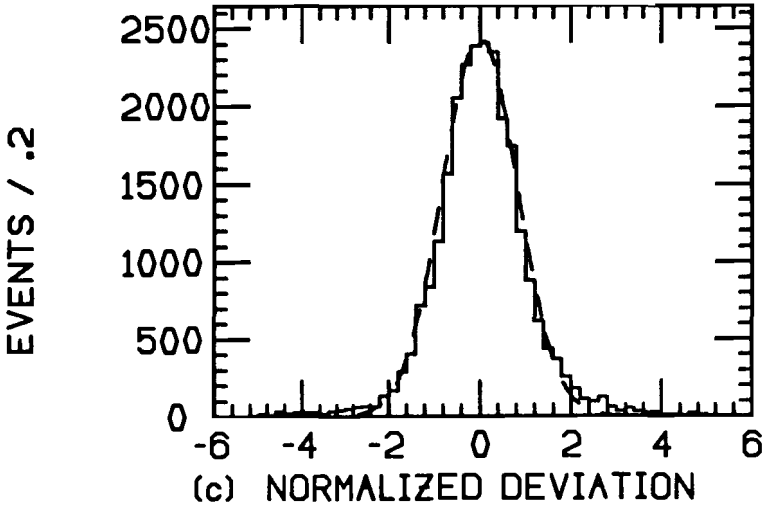
EVENTS / .2
2500
2000
1500
1000
500
0
-6 -4 -2 0 2 4 6
(c) NORMALIZED DEVIATION

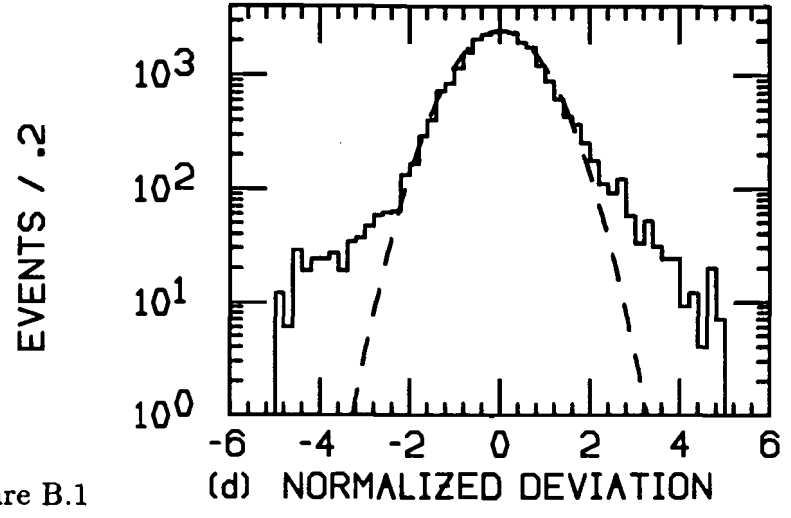
EVENTS / .2
10^3
10^2
10^1
10^0
-6 -4 -2 0 2 4 6
(d) NORMALIZED DEVIATION

Figure B.1

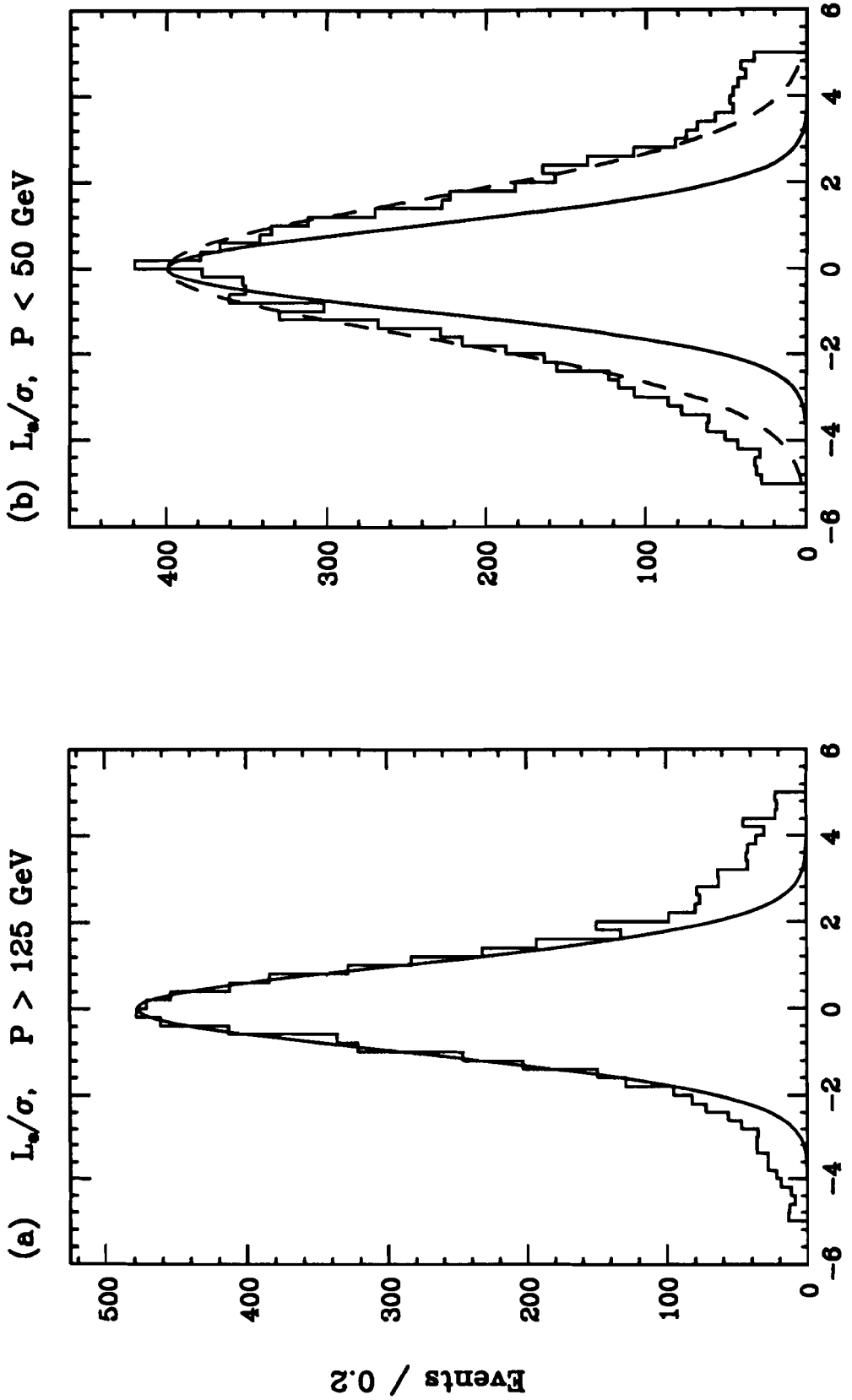
(a) L_e/σ, P > 125 GeV
(b) L_e/σ, P < 50 GeV
Events / 0.2
0
100
200
300
400
500
−6
−4
−2
0
2
4
6

Figure B.2

REFERENCES

1. S.L. Glashow, J. Iliopoulos, and L. Maiani, *Phys. Rev.* **D2** (1970) 1285.
2. J.E. Augustin et al., *Phys. Rev. Lett.* **33** (1974) 1406.
3. J.J. Aubert et al., *Phys. Rev. Lett.* **33** (1974) 1404.
4. G. Goldhaber et el., *Phys. Rev. Lett.* **37** (1976) 255;
   J.E. Wiss, Ph.D. thesis, University of California, Berkeley (1977).
5. Particle Data Group, Review of Particle Properties, *Phys. Lett.* **170B** (April 1986).
6. M.B. Einhorn and S.D. Ellis, *Phys. Rev.* **D12** (1975) 2007;
   C.E. Calrson and R. Suaya, *Phy. Rev.* **D14** (1976) 3115;
   L.M. Jones and H.W. Wyld, *Phys. Rev.* **D17** (1978) 1782;
   R.K. Ellis and C. Quigg, A Pinacoteca of Cross Sections For Hadroproduction of Heavy Quarks, FNAL preprint FN-445/2013.000, January 1987.
7. J. Gunion, *Phys. Rev.* **D10** (1974) 242;
   G. Farrar, *Nucl. Phys.* **B77** (1974) 429.
8. V. Barger et al., *Phys. Lett.* **91B** (1980) 253;
   S.D. Holmes, W. Lee, and J.E. Wiss, *Ann. Rev. Nucl. Part. Sci.* **35** (1985) 397.
9. F. Muller, Hadroproduction of Charmed Particles, Invited talk at the Warsaw Symposium on Elementary Particle Physics, May 1981, Kazimierz, Poland;
   S. Wojcicki, New Flavor Production in γ, μ, ν, and Hadron Beams, Proc. XX ICHEP, Madison, Wisc., 1980, eds. L. Durand and L.G. Pondrom (AIP, New York, 1981) p.1431 (hereafter referred to as ICHEP-80).
10. B.L. Combridge, *Nucl. Phys.* **B151** (1979) 429.
11. V. Barger and R.J.N. Phillips, *Phys. Rev.* **D31** (1985) 215.
12. For a thorough experimental review see A. Kernan and G. VanDalen, *Phys. Rep.* **106** (1984) 298.
13. J.F. Gunion, *Phys. Lett.* **88B** (1979) 150.
14. D. Drijard et al., *Phys. Lett.* **81B** (1979) 250;
    D. Drijard et al., *Phys. Lett.* **85B** (1979) 452.
15. K.L. Giboni et al., *Phys. Lett.* **85B** (1979) 437.

16. W. Lockman et al., *Phys. Lett.* **85B** (1979) 443.

17. J. Irion et al., *Phys. Lett.* **99B** (1981) 495.

18. G. Sajot, Production of charm in the SFM at the ISR, in ICHEP-80, p.192; D. Drijard et al., *Phys. Lett.* **85B** (1979) 425.

19. D. Treille, Proc. Int. Symp. on Lepton and Photon Interactions at High Energies, Bonn, August 1981;
S. Reucroft, Proc. Multiparticle Dynamic Conf., Lake Tahoe, California, July 1982;
W. Willis, Selected Topics in ISR Physics, CERN 82-11, EP Division, November 1982.

20. R.J.N. Phillips, Phenomenology of New Particle Production, ICHEP-80, p. 1471; C.E. Carlson and R. Suaya, *Phys. Rev.* **D18** (1978) 760.

21. K.P. Das and R.C. Hwa, *Phys. Lett.* **68B** (1977) 459.

22. V. Barger et al., *Phys. Rev.* **D24** (1981) 1428;
V. Barger et al., *Phys. Rev.* **D25** (1982) 112;
R. Odorico, *Phys. Lett.* **107B** (1981) 232.

23. P. Mazzanti and S. Wada, *Phys. Rev.* **D26** (1982) 602.

24. S.J. Brodsky et al., *Phys. Lett.* **93B** (1980) 451;
S.J. Brodsky et al., *Phys. Rev.* **D23** (1981) 2745.

25. J.F. Owens and E. Reya, *Phys. Rev.* **D17** (1978) 3003;
D.W. Duke and J.F. Owens, *Phys. Rev.* **D30** (1984) 49.

26. P.R. Avery, Ph.D. thesis, University of Illinois, Urbana (1980);
J.J. Russell, Ph.D. thesis, University of Illinois, Urbana (1980);
M.J. Lamm, Ph.D. thesis, University of Illinois, Urbana (1983).

27. P. Coteus et al., *IEEE Trans. on Nucl. Sci.* **32**, 1, (1984) 585.

28. D. Harding et al., *IEEE Trans. on Nucl. Sci.* **30**, 5, (1983) 3768.

29. R.K. Ellis and J.C. Sexton, Explicit formula for heavy flavour production, FERMILAB-Pub-86/111-T, (August 1986).

30. R.D. Field and R.P. Feynman, *Nucl. Phys.* **B136** (1978) 1.

31. R. Ammar et al., *Phys. Lett.* **178B** (1986) 124.

32. M.E. Duffy et al., *Phys. Rev. Lett.* **55** (1985) 1816;
A.N. Aleev et al., preprint JINR E 86-422 (1986).

33. M. MacDermott and S. Reucroft, *Phys. Lett.* **184B** (1987) 108;
J. Qiu, *Phys. Lett.* **191B** (1987) 182.

34. P. Coteus et al., Production of Charm Strange Baryon Ξ_c^+ By Neutrons, Contributed talk at DPF meeting in Salt Lake City, (January 1987).

35. M. Aguilar-Benitez et al., *Phys. Lett.* **135B** (1984) 237.

36. M. Aguilar-Benitez et al., *Phys. Lett.* **123B** (1983) 103;
M. Aguilar-Benitez et al., *Phys. Lett.* **161B** (1985) 400;
M. Aguilar-Benitez et al., *Phys. Lett.* **164B** (1985) 404;
M. Aguilar-Benitez et al., *Phys. Lett.* **189B** (1987) 254.

37. R. Ammar et al., *Phys. Lett.* **183B** (1987) 110.

38. R. Bailey et al., *Z. Phys. C – Particles and Fields*, **30** (1986) 51;
S. Barlag et al., *Phys. Lett.* **184B** (1987) 283.

39. R. Klanner et al., Observation of Charmed Baryon Production in 150 GeV pBe Interaction, Presentation (and paper) given at the EPS International Conference on High Energy Physics, Lisbon, July 1981.

40. A.N. Aleev et al., *Sov. J. Nucl. Phys.* **35** (1982) 687;
A.N. Aleev et al., *Z. Phys. C – Particles and Fields*, **23** (1984) 333.

VITA

John Eugene Filaseta was born in Fort Knox, Kentucky on September 13, 1957. He entered the University of Arizona in 1975 and graduated with a Bachelor of Science degree in 1979. Since 1979 he has held teaching and research assistantships in the Physics Department at the University of Illinois at Urbana-Champaign. In 1980 he received a Masters of Science degree from the University of Illinois.